Optimal energy management strategy for hybrid electric vehicles with consideration of battery life

Dissertation

Presented in Partial Fulfillment of the Requirements for the Degree Doctor of Philosophy in the Graduate School of The Ohio State University

By

Li Tang, B.S., M.S.

Graduate Program in Mechanical Engineering

The Ohio State University

2017

Dissertation Committee:

Giorgio Rizzoni, Advisor

Levent Guvenc

Vadim Utkin

Wei Zhang

ProQuest LLC.
789 East Eisenhower Parkway
P.O. Box 1346
Ann Arbor, MI 48106 – 1346

Abstract

The dissertation offers a systematic analysis on the interdependency between fuel economy and battery capacity degradation in hybrid electric vehicles. Optimal control approaches including Dynamic Programming and Pontryagin's Minimum Principle are used to develop energy management strategies, which are able to optimally tradeoff fuel consumption and battery aging. Based on the optimal solutions, a real-time implementable battery-aging-conscious Adaptive Equivalent Consumption Management Strategy is proposed, which is able to achieve performance that is comparable to optimal results. In addition, an optimal control based charging strategy for plug-in hybrid electric vehicles and battery electric vehicles is developed, which minimizes battery capacity degradation incurred during charging by optimizing the charging current profile. Combining a generic control-oriented vehicle cabin thermal model with the battery aging model, the benefit of this strategy in terms of decreasing battery aging is significant, when compared with the existing strategies, such as the widely accepted constant current constant voltage (CC-CV) protocol. Thus this dissertation presents a complete set of optimal control solutions related to xEVs with consideration of battery aging.

To my parents and the rest of my family for their constant help and support during my graduate studies.

Acknowledgments

This journey would not be so wonderful without the help and support of many of the great people at the Center for Automotive Research of The Ohio State University. My advisor Dr. Giorgio Rizzoni has been patiently and constantly providing me with guidance and support to expand my research interests as well as to achieve each target. His dedication and enthusiasm always encourage me to pursue all the possibilities and to live the most of my life.

I would like to thank my colleagues and all the staff at the Center for Automotive Research for making both my life and work easy, convenient and enjoyable. They show and teach me the real buckeye spirit.

Vita

July, 2010	B.S. Mechanical Engineering, Shandong University, China
December, 2011	M.S. Mechanical Engineering, Carnegie Mellon University
June - August 2016	Simulation Engineer Intern, Delphi Automotive
August, 2012 - present	Graduate Research Associate, Center for Automotive Research, The Ohio State University

Publications

Research Publications

L. Tang, G. Rizzoni and S. Onori "Optimal energy management of HEVs with consideration of battery aging". *Proceedings of Transportation Electrification Asia-Pacific (ITEC Asia-Pacific), IEEE Conference and Expo*, 2014.

L. Tang, G. Rizzoni and S. Onori "Energy management strategy for HEVs including battery life optimization". *IEEE Transactions on Transportation Electrification*, 1(3):211-222, 2015.

L. Tang, and G. Rizzoni "Energy management strategy including battery life optimization for a HEV with a CVT". *Proceedings of Transportation Electrification Asia-Pacific (ITEC Asia-Pacific), IEEE Conference and Expo*, 2016.

L. Tang, G. Rizzoni and A. Cordoba-Arenas "Battery Life Extending Charging Strategy for Plug-in Hybrid Electric Vehicles and Battery Electric Vehicles". *Proceedings of 8th IFAC Symposium on Advances in Automotive Control-AAC*, 2016.

L. Tang, G. Rizzoni, M. Lukas "Comparison of Dynamic Programming-based Energy Management Strategies Including Battery Life Optimization". *Proceedings of Electrical Systems for Aircraft, Railway, Ship Propulsion and Road Vehicles & International Transportation Electrification Conference (ESARS-ITEC), IEEE Conference and Expo*, 2016.

L. Tang, G. Rizzoni and A. Cordoba-Arenas "Hybrid and Electric Vehicle Charging Optimization Accounting for Battery Aging". *Submitted to IFAC Journal of Control Engineering Practice.*

L. Tang, G. Rizzoni "Comparative Studies of Energy Management Strategies for HEVs with Consideration of Battery Aging". *In preparation for IEEE Transactions on Vehicular Technology.*

L. Tang, G. Rizzoni "Battery Aging Adaptive Energy Management Strategy for HEVs". *In preparation for IEEE Transactions on Control System Technology.*

Invention Disclosure

L. Tang, G. Rizzoni "Life Extending Charging Strategy for Plug-in Hybrid Electric Vehicles (PHEVs) and Battery Electric Vehicles (BEVs)". *submitted to Technology Commercialization Office The Ohio State University*, 2014.

L. Tang, G. Rizzoni "Battery Aging Adaptive Energy Management Strategy for xEV Powertrains". *submitted to Technology Commercialization Office The Ohio State University*, 2017.

Fields of Study

Major Field: Mechanical Engineering

Table of Contents

Page

Abstract ii

Dedication iii

Acknowledgments iv

Vita v

List of Tables x

List of Figures xii

List of Acronyms and Symbols xvii

1. Introduction 1

   1.1 Motivation 1
   1.2 Contribution of the Dissertation 3
   1.3 Organization of the Dissertation 4

2. Background and Literature Review 6

   2.1 Optimal Control of Hybrid Vehicles 6
      2.1.1 The energy management problem in HEVs 6
      2.1.2 Dynamic programming 10
      2.1.3 Analytical optimal control 13
      2.1.4 Instantaneous minimization method 16
      2.1.5 Model predictive control 20
   2.2 Battery aging 22
   2.3 Energy Management Strategy Integrated with Battery Health . . . 27

3. Model Development 33

3.1 HEV Powertrain 33
3.1.1 Powertrain architecture description 33
3.1.2 Vehicle road load model 34
3.1.3 Engine 35
3.1.4 Electric machine 38
3.1.5 Continuously variable transmission 38
3.2 Li-ion Battery Pack 40
3.2.1 Battery electrical model 41
3.2.2 Battery thermal model 44
3.2.3 Battery capacity degradation model 46
3.3 Vehicle cabin and battery thermal model 49
3.3.1 Solar radiation load 53
3.3.2 Generic Cabin Geometry 55
3.3.3 Vehicle cabin temperature simulation 57
3.4 Vehicle Model Integration 60
3.5 Summary 68

4. Optimal Control Problems for Hybrid and Electric Vehicles with Consideration of Battery Aging 69

4.1 Design of objective function 70
4.2 States and constraints 75
4.3 Control and constraints 76
4.4 Sequential optimization strategy 77
4.4.1 Problem formulation 77
4.4.2 DP solution 83
4.4.3 Simulation results 85
4.4.4 Summary 108
4.5 Systematic optimization strategy 110
4.5.1 Problem formulation 110
4.5.2 PMP solution 112
4.5.3 Simulation results 115
4.5.4 Summary 124
4.6 Comparison of sequential optimization and systematic optimization 127
4.7 Hybrid and electric vehicle charging optimization accounting for battery aging 135
4.7.1 Background and literature 136
4.7.2 Optimal control problem formulation with PMP 139
4.7.3 Simulation results 141

4.8 Summary 148

5. Real-time Energy Management Strategy for HEVs with Consideration of Battery Aging 150

5.1 Adaptive equivalent consumption minimization strategy 152
5.1.1 ECMS formulation 152
5.1.2 Adaptation based on feedback from SOC 153
5.1.3 Calibration of adaptive strategies 154
5.2 Aging-severity-based battery power correction 160
5.3 CVT ratio correction 163
5.4 Calibration and Simulation Results 169
5.5 Validation 177
5.6 Summary 182

6. Conclusion 183

Appendices 186

A. The Comparison between Sequential Optimization and Systematic Optimization over FUDS 186

B. Effects of Calibration Parameters on A-ECMS Performance over FUDS . 192

C. Calibration and Simulation Results of Aging-concious A-ECMS over FUDS 195

Bibliography 199

List of Tables

Table		Page
3.1	Components Specifications	34
3.2	Vehicle Parameters	36
3.3	Battery Cell Specifications	41
3.4	Battery Thermal Model Parameters	46
3.5	Battery Aging Experiment Data	47
3.6	Vehicle Cabin and Battery Thermal Model Parameters	52
3.7	Parameters in Solar Radiation Calculation	54
3.8	Surface Area and Angles	56
3.9	Braking Torque Split Parameters	65
4.1	Dynamic Programming Solution for US06	87
4.2	Dynamic Programming Solution for FUDS	97
4.3	Summary of DP Results	107
4.4	Simulation Results for US06	122
4.5	Simulation Results for FUDS	124
4.6	Performance Measure of US06 for Two Approaches	129

4.7 Summary of Level 2 Charging 143

4.8 Summary of Fast Charging 148

5.1 Effect of Calibration Parameters 155

5.2 w Value from Curve Fitting 163

5.3 Performance of Aging-conscious A-ECMS over US06 172

5.4 Validation of Aging-conscious A-ECMS 182

A.1 Performance Measure of FUDS for Two Approaches 187

B.1 Effect of Calibration Parameters 192

C.1 Performance of Aging-concious A-ECMS over FUDS 195

List of Figures

Figure **Page**

2.1 Schematic of Semi-empirical Model Development 27

3.1 Vehicle Architecture 34

3.2 Forces Acting on a Vehicle 36

3.3 1.6L Engine Fuel Flow Rate Map 37

3.4 Electric Machine Efficiency Map 39

3.5 Battery Cell 41

3.6 0^{th}-order Equivalent Circuit 42

3.7 Cell Open Circuit Voltage 44

3.8 Cell Internal Resistance 45

3.9 Curve fitting result of identified aging model with the experimental data [141] 47

3.10 Vehicle Cabin and Battery Thermal Load 51

3.11 Representation of the direct solar radiation component 53

3.12 Apparent Daily Path of the Sun 55

3.13 A Generic Vehicle Surface Geometry [70] 56

3.14 Environment Conditions in Phoenix Arizona 58

3.15 Vehicle Cabin Temperature 59
3.16 Vehicle Pedal Signal and Speed Profile 61
3.17 Vehicle Simulator Schematic 62
3.18 Vehicle Supervisory Controller 63
3.19 Braking Force & Braking Pedal Position 65
3.20 Variables Related to Powertrain Operation 66
3.21 Variables Related to Battery Operation 67
4.1 Severity Factor Map 73
4.2 Engine Fuel Map And Efficiency Map 79
4.3 Engine Optimal Operation Line 80
4.4 Map of CVT Ratio as A Function of Engine Power and Output Speed 81
4.5 Dynamic programming solutions for US06 with different α values . . 87
4.6 Dynamic programming solutions for US06 with different α values . . 88
4.7 Power split for US06 with different α values 91
4.8 Electric machine power for US06 with different α values 92
4.9 Battery energy throughput for US06 with different α values 92
4.10 Battery severity factor profile for US06 with different α values 93
4.11 Battery severity factor distribution for US06 with different α values . 94
4.12 CVT Ratio for US06 95
4.13 Engine operating points for US06 with different α values 95

4.14 Pareto Front for FUDS 97

4.15 Relative Optimality for US06 and FUDS 98

4.16 Dynamic programming solutions for FUDS with different α values . 100

4.17 Power split for FUDS with different α values 101

4.18 Power split for FUDS with $\alpha = 0.2$ 102

4.19 Battery energy throughput for FUDS with different α values 102

4.20 Battery severity factor distribution for FUDS with different α values 103

4.21 Transmission and Engine Operation for FUDS 105

4.22 Pareto Front 107

4.23 Battery energy throughput for Manhattan with different α values . . 109

4.24 Battery energy throughput for Artemis-urban cycle with different α values 109

4.25 λ_1 Dynamics 116

4.26 λ_2 Dynamics 117

4.27 Visualization of the Hamiltonian at one instant (t = 300 s in driving cycle US06) 118

4.28 States and co-states trajectories over US06 with ambient temperature at 30 °C 120

4.29 $\frac{\partial \sigma}{\partial \theta_{batt}}$ at 8C 121

4.30 States trajectories from different controllers with $\alpha = 0.7$ over US06 with ambient temperature at 30 °C 123

4.31 States and co-states trajectories over FUDS with ambient temperature at 30 °C 125

4.32 State trajectories from different controllers with $\alpha = 0.7$ over FUDS with ambient temperature at 30 °C 126

4.33 Pareto Front of US06 129

4.34 Battery Energy Throughput of US06 130

4.35 State trajectories and CVT ratio for US06 with $\alpha = 0.4$ at 30 °C . . . 132

4.36 Engine Operating Conditions for US06 with $\alpha = 0.4$ at 30 °C 133

4.37 Electric Machine Operating Conditions for US06 with $\alpha = 0.4$ at 30 °C 134

4.38 Level 2 Charging Battery Temperature and SOC 144

4.39 Level 2 Charging Battery Severity and C rate 145

4.40 Fast Charging in 30 minutes 146

4.41 Fast Charging in 10 minutes 147

5.1 Control Diagram of A-ECMS Accounting for Battery Aging 151

5.2 Results obtained from five US06 cycles with different k_p 156

5.3 Results obtained from five US06 cycles with different k_p 157

5.4 Results obtained from five US06 cycles with different T 158

5.5 Results obtained from five US06 cycles with different T 159

5.6 SOC Penalty Function 160

5.7 σ_{rms} and $P_{batt,rms}$ at different driving conditions obtained from Dynamic Programming 164

5.8 Curve fitting results for data obtained from Dynamic Programming . 165

5.9 Possible engine fuel consumption at wheel power request of 21 kW . 167

5.10 Comparison between Willans line mode and experimental data 170

5.11 Control Flow Chart of A-ECMS Accounting for Battery Aging 171

5.12 Aging-conscious A-ECMS Controller Output over US06 173

5.13 Battery Power Correction with Different $\bar{\sigma}$ over US06 175

5.14 Battery Severity Factor with Different $\bar{\sigma}$ over US06 176

5.15 Speed Profile of Test Cycle 178

5.16 Aging-conscious A-ECMS Controller Output over Test Cycle 179

5.17 Battery Power Correction with Different $\bar{\sigma}$ 180

5.18 Battery Severity Factor with Different $\bar{\sigma}$ 181

A.1 Pareto Front of FUDS 186

A.2 Battery Energy Throughput of FUDS 188

A.3 State trajectories and CVT ratio for FUDS with $\alpha = 0.5$ at 30 °C . . 189

A.4 Engine operating conditions for FUDS with $\alpha = 0.5$ at 30 °C 190

A.5 Electric machine operating conditions for FUDS with $\alpha = 0.5$ at 30 °C 191

B.1 Results obtained from five FUDS cycles with different k_p 193

B.2 Results obtained from five FUDS cycles with different T 194

C.1 Aging-concious A-ECMS Controller Output over FUDS 196

C.2 Battery Power Correction with Different $\bar{\sigma}$ over FUDS 197

C.3 Battery Severity Factor with Different $\bar{\sigma}$ over FUDS 198

List of Acronyms and Symbols

Acronyms

A-ECMS Adaptive Equivalence Consumption Minimization Strategy

BEV Battery Electric Vehicle

CC-CV Constant Current Constant Voltage

CVT Continuously Variable Transmission

DP Dynamic Programming

ECMS Equivalence Consumption Minimization Strategy

HEV Hybrid Electric Vehicle

MHC Moving Horizon Control

MPC Model Predictive Control

PHEV plug-in Hybrid Electric Vehicle

PMP Pontryagin's Minimum Principle

RHC Receding Horizon Control

SOC State of Charge

Symbols

α	Acceleration pedal position
α	Cost function weighing factor
β	Braking pedal position
$\dot{m}$	Mass flow rate
$\dot{q}$	Rate of heat generation
η	Efficiency
Γ	Battery nominal life in terms of Ah
γ	Battery life in terms of Ah
λ	Co-state
$\mathcal{U}$	Admissible control set

$\mathcal{X}$	Admissible state set
$\mathscr{H}$	Hamiltonian
ω	Rotational speed
ϕ	Final cost of optimal control problem
σ	Battery severity factor
θ	Temperature
a	Acceleration [m/s^2]
a_D	Discrete state update function
Ah	Ampere hour throughput
F	Force
g	Gravitational acceleration
$G(x,t)$	State constraints
I	Current
J	Cost function of optimal control problem
k	Time index
L	Instantaneous Cost
LHV	Lower heating value of gasoline
M	Mass
N_p	Battery cell number in parallel
N_s	Battery cell number in series
P	Power
Q	Capacity
R	Gas constant
r	Transmission ratio
R_0	Battery cell internal resistance
s	Equivalence factor
T	Time interval
T	Torque
t	Time
u	Control variable(s)
v	Speed
V_{oc}	Battery cell open circuit voltage

x Control system state(s)

Subscripts

$aero$ Aerodynamics

amb Ambient

$batt$ Battery

brk Braking

$cell$ Battery cell

ch Charging

$cool$ Coolant

cvt Continuously variable transmission

$diff$ Final differential

dis Discharging

ele Electricity

em Electric machine

eng Internal combustion engine

f Fuel

$grade$ Grade due to slope

ice Internal combustion engine

$ress$ Rechargeable energy storage system

$road$ Road load

$roll$ Rolling resistance

$trac$ Traction

veh Vehicle

wh Wheel

Chapter 1: Introduction

1.1 Motivation

Hybrid electric vehicles (HEVs) represent a steadily increasing segment of the automotive market. In the evolution of the design of hybrid vehicle systems, challenges keep coming up. These challenges are driven by the increasingly stringent government policies for fuel economy and emissions and by the progress in the technical development of major components such as batteries. It has been recognized that HEVs are the ideal transition from conventional all-petroleum vehicles to the all-electric vehicles due to the fact that they are combinations of an internal combustion engine (ICE) and an electric machine (EM). Thanks to an electrochemical energy storage system, e.g. a battery pack, HEVs offer features such as engine start/stop, engine downsizing, regenerative braking, and motor assist. With all the favourable features, an HEV's performance is influenced by many interrelated factors, which put advanced control strategies in critical position to improve performance and lower cost.

The overall performance of HEVs in terms of fuel consumption or energy consumption is dependent on the efficiency of individual powertrain components and good coordination of the drivetrain. In other words, the energy management strategy

in an HEV plays a very important role. The additional degrees of freedom in providing power to the vehicle make it possible to solve various optimization problems in allocating the vehicle power demand to the internal combustion engine and the electric drivetrain. Optimal control methods have been used extensively to design energy management strategies capable of delivering the best fuel economy while preserving other desirable performance and utility features [117, 111, 131, 125, 96, 138, 73]. Traditionally, the overall control objectives of an energy management strategy is to maximize fuel economy during a driving schedule without sacrificing vehicle performance [24, 116, 126].

The fuel economy of HEVs is highly dependent on the energy capacity of the on-board energy storage system. However, energy storage systems experience degradation in both energy capacity and internal resistance due to several irreversible degradation processes. The rate of battery capacity loss is dictated by many factors including operating and environmental conditions. Factors such as extreme temperature, high c-rate, high or low state of charge and excessive depth of discharge are recognized to contribute to capacity degradation [31, 145, 25, 17, 147]. On one hand, limiting stresses on the battery that could accelerate its aging may result in energy management policies that are conflict with the desire to minimize fuel consumption. On the other hand, Li-ion batteries represent a big part of vehicle cost. Therefore designing batteries to last for the life of a vehicle while still satisfying the energy and power requirements is not only a need but also a challenge. A hybrid electric vehicle equipped with a supervisory energy management controller that is able to reduce the battery aging effects during vehicle operation can potentially extend the battery life

and reduce overall cost.

1.2 Contribution of the Dissertation

The primary objective of this research is to investigate the relationship between fuel economy and battery capacity degradation in hybrid electric vehicles, and to develop a real-time implementable energy management strategy based on optimal performance, which is able to balance the two objectives: maximizing fuel economy and minimizing battery capacity degradation. This is the first time that a systematic analysis on interdependency of battery aging and energy management has been conducted. In order to achieve better estimation of battery capacity loss during vehicle operation, a control-oriented and experimental validated battery capacity degradation model is directly linked to the design of energy management strategy. Based on the insights gained from global optimal solutions, an online implementable control strategy is proposed, which is able to achieve close-to-optimal performance.

Additionally, the performance and longevity of Li-ion batteries depend, to a large extent, on the quality of their chargers. Therefore an optimal charging algorithm is developed for plug-in hybrid electric vehicle and battery electric vehicles, which is able to minimize battery capacity degradation for any given time window taking into account the environmental conditions. A generic vehicle cabin thermal model is developed and applied for designing the optimal charging strategy, which takes into account not only the ambient temperature but also the solar radiation. With the help of the weather forecast, it is realistic to predict the surrounding conditions of

the battery pack, which enables the real-time implementation of the optimal charging algorithm. Thus this dissertation presents a complete set of optimal control solutions related to xEVs with consideration of battery aging.

1.3 Organization of the Dissertation

This dissertation is organized as follows:

- **Chapter 2 Background and Literature Review** reviews energy management strategies for HEVs and related optimal control theories. An overview of lithium-ion battery aging phenomena and mathematical models is given. Finally, a review of relevant work, which incorporates battery life into energy management of HEVs, is also given.

- **Chapter 3 Model Development** describes the vehicle model used in designing the energy management strategy, which includes vehicle road load model, powertrain model, battery aging model and vehicle cabin and battery thermal model.

- **Chapter 4 Optimal Control Problems for Hybrid and Electric Vehicles with Consideration of Battery Aging** provides the detailed optimal control problem formulation as well as the analysis on the optimal solutions. Comparative studies on different strategies are also given.

- **Chapter 5 Real-time Energy Management Strategy for HEVs with Consideration of Battery Aging** presents an Adaptive Equivalence Consumption Minimization Strategy (A-ECMS) based battery-aging-conscious energy management strategy.

- **Chapter 6 Conclusions**

Chapter 2: Background and Literature Review

2.1 Optimal Control of Hybrid Vehicles

A hybrid electric vehicle is equipped with more than one energy sources. Usually, one of them is a high-capacity storage, for example: a liquid fuel tank, which is complemented by a low-capacity rechargeable energy storage system which is typically electrochemical batteries. Unlike in conventional vehicles, in which all the requested power from the driver is fulfilled by the chemical fuel, in hybrid electric vehicles, an additional decision has to be taken on how to distribute the power request among different energy sources especially when bi-directional power flows are allowed. A supervisory controller, which is also referred to as an energy management strategy in hybrid electric vehicles, plays the role of commanding the power split. In this section, the problem of designing such energy management strategies is introduced and formalized using optimal control theory.

2.1.1 The energy management problem in HEVs

In general, the intention of a hybrid architecture is the potential to achieve better fuel economy and lower emissions through the additional degree of freedom due to the presence of an additional energy source besides the primary one. This implies that at

any time and for any vehicle speed, the power needed by the vehicle can be provided by either one of these sources, or by a combination of the two. Regardless of the vehicle topology, the primary goal of any control strategies is to satisfy the drives' power requests by managing the power distributions among different on board energy storage systems while minimizing the total fuel consumption or some combined objectives.

The achievable improvement in fuel economy and as well as other merits are highly dependent on the energy management strategy. Making the correct decisions on power split is usually a complex problem. Early energy management controllers were mainly based on heuristic approaches inspired by the preferred behavior of the propulsion system [64, 12, 117]. The main advantage of the heuristic approaches is the easy implementation in real-time driving. The control input is decided by a set of rules, which are designed based on engineering intuitions or the knowledge gained from a series of global optimal strategies. As there is no explicit optimization involved, the computational load is small. In addition, the rule-based strategies are not dependent on the future driving conditions, so no prediction is required, which makes the real-time implementation convenient.

However, heuristic strategies cannot guarantee the desired vehicle performance under different conditions. One way to resolve this problem is to adopt systematic, model-based optimization methods with meaningful performance index or objective functions. Traditionally, the main objective of the energy management strategy is to minimize fuel consumption over a route, however, many other favourable performance indexes can be included as well such as reduction of pollutant emissions [82, 38, 66]

and improvement on driveabiliy [115, 105, 23] and battery life [137, 144, 143]. In general, it is possible to define the objective of hybridization as the minimization of a given cost function. Thus a general cost function has the form of

$$J = \phi(x(t_f)) + \int_0^{t_f} L(x(t), u(t), t)dt \tag{2.1}$$

where Ł$(\cdot)$ is the cost function, $x(t) \in \Re^n$ indicates the state vector, $u(t) \in \Re^p$ is the control vector, and $\phi(\cdot)$ is the penalty function on the final states. Multiple objectives can be combined into a single cost function by introducing weighting factors [97, 133, 93]. When multiple cost terms are considered, normalization is usually required so that all the cost terms are numerically comparable, which is critical especially for numerical solutions [85].

There are many state variables in a hybrid powertrain. The dimension of the state vector is dictated by the objective or the required level of accuracy [85, 57]. The system is often treated as quasi-stationary, if fuel consumption is the main concern. In this case, it is acceptable that battery state of charge (SOC) is considered as the only state variable. Other state variables, which represent the dynamic behavior of the electric motor and the ICE, have much faster dynamics than that of the main energy flows in an HEV and, therefore, are not considered in this situation. However, if drivability is included in the cost function, a more detailed dynamic vehicle model is needed resulting in additional state variables [77]. In general, state equation can be expressed as:

$$\dot{x}(t) = f(x(t), u(t), t) \tag{2.2}$$

The energy management problem is a constrained optimal control problem, which is subject to both state constraints and control constraints, which are usually time-variant [126]. In general, the state variable, battery SOC, is confined in an allowable range, which is specified by SOC_{min} and SOC_{max}, and which is a local or instantaneous constraint. In addition to that, charge sustenance is required by HEVs, which means SOC, at the end of driving cycles, needs to remain within some prescribed range, which is a global constraint. There are two ways to take into consideration of the sustenance constraint. One is to include it as a soft constraint, that is, by introducing penalty function $\phi(\cdot)$ on the deviations from the initial value of the charge level at the end of the driving cycles. Another choice is to treat charge sustenance as a hard constraint by requiring that the charge level at the end of mission equals to the initial value: $SOC(0) = SOC(T)$. Control constraints mostly concern physical operation limits such as maximum engine speed and the corresponding torque limit, motor power or battery power limits. Other control constraints can be imposed to enhance smoothness or performance. In general, the set of admissible states and controls are defined as:

$$\begin{cases} G(x,t) \leqslant 0 \\ u(t) \in \mathcal{U} \end{cases} \qquad \forall t \in [0, t_f] \tag{2.3}$$

It is clear that the energy management problem in a hybrid vehicle is a constrained-finite time horizon optimal control problem. The goal is to find the control vector u^* that minimizes the cost function (2.1) while meeting the dynamic constraints (2.2), and the local state and control constraints (2.3). In the following sections, techniques and methods to solve the optimal energy management problem are reviewed and discussed.

2.1.2 Dynamic programming

Once the objective function for a system has been chosen, the next task is to solve for a control function that minimizes this criterion. In the field of optimal control theory, two methods of accomplishing the minimization are the Minimum Principle of Pontryagin [118], and the method of Dynamic Programming developed by R. E. Bellman [16, 15, 14], and Dynamic Programming is the only optimal control technique capable of providing the optimal solution to problems of any complexity level. In this section Dynamic Programming is briefly introduced. The computational procedure and its application on energy management problems in HEVs are discussed.

Dynamic Programming is commonly used to solve for numerical solutions [128, 82, 24]. An optimal control policy is found by employing the principle of optimality: an optimal policy has the property that whatever the initial state and initial decision are, the remaining decision must constitute an optimal policy with regard to the state resulting from the first decision. In other words, from any point on an optimal trajectory the remaining trajectory is optimal for the corresponding problem that begins at that point.

First we approximate the continuously operating system of (2.2) by a discrete system described by the state difference equation

$$x_{k+1} = a_D(x_k, u_k) \quad k = 0, 1, \cdots, N-1 \tag{2.4}$$

where u_k is the control variable whose value is to be determined at time step k. Both the state x and control u are bounded and discretized.

It is desired to determine the control law that minimizes the criterion

$$J = L_N(x_N) + \sum_{k=0}^{k=N-1} L_k(x_k, u_k) \tag{2.5}$$

where L_k is defined as the arc cost, which is the same as the integrand in the continuous-time formulation (2.1).

The dynamic programming algorithm works by calculating the sequence of minimal cost-to-go backwards in time, which leads to the recurrence equation:

$$\begin{aligned} J^*_{N-k,N}(x(N-k)) = \min_{u(N-k)} \{ & L_{N-k}(x(N-k)) \\ & + J^*_{N-(k-1),N}(a_D(x(N-k), u(N-k)))\} \end{aligned} \tag{2.6}$$

with initial value

$$J^*_{N,N}(x(N)) = L_N(x(N)) \tag{2.7}$$

In (2.6), $J^*_{N-k,N}(x(N-k), u(N-k))$ represents the optimal cost at step $N-k$ in a problem with total N steps. The solution of this recurrence equation is an optimal control law or optimal policy, $u^*(x(N-k), N-k), \quad k = 1, 2, \cdots, N$, which is obtained by trying all the admissible control values at each admissible state value. In order to make the computational procedure feasible, it is required to quantize the state variables, control variables as well as the time variable. The solution obtained is the absolute (or global) minimum.

Dynamic Programming can be applied to solve the energy management problem in hybrid electric vehicles. The cost represents fuel consumption, emissions, or any other objectives to be minimized. The algorithm works by computing the sequence of minimal cost-to-go backwards in time, which means the final instant of driving cycle is processed first. In order to do so, all the arc costs between feasible states must be evaluated. The control input at each instance is the power split between the internal combustion engine and the rechargeable energy storage system. However, the actual decision variable of the algorithm is the system state, $x(k)$, rather than the control input. In the case of energy management problem for HEVs, Dynamic Programming algorithm determines the optimal sequence of state of charge in the rechargeable energy storage system, and then, as a consequence, the power that produces it. This way the state constraints can be implemented easily, as only the range of admissible state values is considered and therefore the states will never exceed boundaries. The number of solution candidates that can be considered and evaluated is a compromise between the computational capabilities and the accuracy of the result. In fact, the minimum cost may not exactly coincide with one of the gridded points, but the closer these are to each other, the better the approximation of the optimal solution. The computational burden of Dynamic Programming increases linearly with the final time t_f, and exponentially with the dimension of the state vector, which is known as the curse of dimensionality.

The global-optimal solution given by Dynamic Programming cannot be implemented directly due to two main reasons: the solution has to be calculated backwards, and therefore the entire driving cycle must be known a priori; it is a computational

demanding algorithm, and the first control action cannot be determined without the backward solution of the entire problem. While not directly realizable, this noncausal strategy often serves as a benchmark for evaluating the performance or optimality of real-time implementable strategies [24, 81, 80, 125, 113, 59, 19].

2.1.3 Analytical optimal control

One approach that enables analytical optimization is based on Pontryagin's Minimum Principle (PMP) [74], which leads to a nonlinear two-point boundary-value problem that must be solved to obtain an optimal control if it exists. Assuming that objective is to minimize the cost described in (2.1) subjected to system dynamics in (2.2) and constraints in (2.3), a Hamiltonian function is defined as

$$\mathscr{H} = L(x(t), u(t), t) + \lambda(t)^T \cdot f(x(t), u(t), t) \tag{2.8}$$

where $f(x(t), u(t), t)$ is the right-hand side of the system dynamic equation (2.2), $L(x(t), u(t), t)$ is the instantaneous cost in (2.1), and $\lambda(t)$ is a vector of optimization variables, which has the same dimension as the state vector, which is known as co-states of the system. Pontryagin's Minimum Principle states that a necessary condition for u^* to minimize the functional J is

$$\mathscr{H}(x^*(t), u^*(t), \lambda^*(t), t) \leqslant \mathscr{H}(x^*(t), u(t), \lambda^*(t), t) \tag{2.9}$$

for any $t \in [0, t_f]$ and for all admissible controls, i.e. the optimal solution $u^*(t)$ is such that

$$u(t)^* = \arg\min_u \mathscr{H}(x^*(t), u(t), \lambda^*(t), t) \tag{2.10}$$

At the same time, the state and co-state must satisfy the following conditions:

$$\dot{x}^*(t) = \frac{\partial \mathscr{H}}{\partial \lambda}|_{u^*(t)} = f(x(t), u(t), t) \tag{2.11}$$

$$\dot{\lambda}^*(t) = -\frac{\partial \mathscr{H}}{\partial x}|_{u^*(t)} = -\frac{\partial L}{\partial x}(x^*(t), u^*(t), t) - \lambda^*(t) \cdot [\frac{\partial f}{\partial x}(x^*(t), u^*(t), t)]^T \tag{2.12}$$

with boundary conditions

$$x^*(0) = x_0 \tag{2.13}$$

$$x^*(t_f) = x_{t_f} \tag{2.14}$$

As discussed before, the constraints on the state can be both local and global. Global constraints can be taken care of by ensuring (2.13) and (2.14). In order to enforce the local constraints on the state, i.e. $G(x, t) \leqslant 0$, additional cost or penalty is introduced in the Hamiltonian, which is activated whenever the state boundaries are reached or violated [103, 50].

An analytical solution is possible if explicit descriptions of $L(x(t), u(t), t)$ and state equations are available. In some special applications, the Hamiltonian function turns out to be an affine or quadratic function of the control variable, thus closed-form solution or an explicit optimal control can be derived. In general, however, the approach based on PMP leads to a nonlinear two-point boundary-value problem that cannot

be solved analytically to obtain the optimal control law. If the boundary conditions were all known at either $t = 0$ or $t = t_f$, we could numerically integrate the differential equation (2.11) and (2.12) to obtain $x^*(t)$, $\lambda^*(t)$, $t \in [0, t_f]$. Unfortunately, the boundary values are split as indicated in (2.13) and (2.14).

A standard way of solving an optimal control problem with PMP is some iterative numerical techniques, among which the most often used is the so called shooting method. The general procedure is stated as the following: an initial guess is used to obtain the solution to a problem in which one or more of the five necessary conditions (2.10-2.14) is not satisfied. This solution is then used to adjust the initial guess in an attempt to make the next solution come closer to satisfying all of the necessary conditions. If these steps are repeated and the iterative procedure converges, the necessary conditions (2.10-2.14) will eventually be satisfied.

Pontryagin's Minimum Principle is a rather powerful tool to solve finite horizon optimization problems. It converts the global optimal control problem to a local and instantaneous minimization problem. Clearly, the global nature of the problem remains evident in the boundary conditions, which requires the information regarding the future to search for the optimal initial condition. As a result, the solution generated by PMP is not causal. Although PMP only offers the necessary conditions for global optimality, it can be used to generate solution candidates. If only one solution is available and the necessary conditions are satisfied, the solution obtained from PMP is the optimal solution. The existence and uniqueness of the solution cannot be proved formally in the general case, but it is reasonable to assume that at least

one optimal solution exists for the energy management problem for hybrid electric vehicles, in the sense that there must be at least one sequence of controls yielding the lowest possible fuel consumption.

PMP requires less computational effort compared with direct numerical optimization methods such as DP, when applied for numerical solutions. It has been widely used for solving optimal control problems in application of HEVs [1, 134, 133, 73, 72, 151].

2.1.4 Instantaneous minimization method

PMP may offer an optimal solution with less computational load compared with DP, but the solution is still not real-time implementable due to the iterative nature requiring knowledge of future driving conditions a priori. One of the possible solutions is to convert the global optimization problem into a sequence of local or instantaneous minimization problems. A well-defined local minimization problem enables quasi-optimal results. The equivalent consumption minimization strategy (ECMS) [110, 127, 96], which is the most well-known one among these strategies, has been recently shown to be equivalent to PMP under certain conditions [130].

As a method to reduce the global minimization problem defined in section 2.1.1 to a sequence of local or instantaneous minimization problems to be solved at each instant without using the information regarding the future, the equivalent consumption minimization strategy was introduced by Paganelli et al. [108, 110, 111, 109]. The essence of ECMS is that in a charge-sustaining HEV, the energy change in the battery

pack at the end of one trip is negligible, which means almost all of the propelling energy is ultimately from the fuel and the battery pack only plays the role of an energy buffer. The electricity used during a battery discharge phase must be replenished at a later phase using the fuel from the engine or regenerative braking. The instantaneous cost that is minimized at each instant is called equivalent consumption, in which the battery energy usage is converted to an equivalent consumption of fuel and added to the real fuel consumption. The instantaneous equivalent fuel consumption to be minimized:

$$\dot{m}_{f,eqv}(t) = \dot{m}_f(t) + \dot{m}_{ress}(t) \tag{2.15}$$

where $\dot{m}_{ress}(t)$ represents the virtual fuel consumption associated to the use of electric energy. As the fuel mass flow rate is calculated based on

$$\dot{m}_f(t) = \frac{P_{eng}(t)}{\eta_{eng}(t) LHV} \tag{2.16}$$

where $\eta_{eng}(t)$ is the engine efficiency and LHV is the fuel lower heating value in [MJ/kg], the virtual fuel mass flow consumed by the electric machine can be represented by analogy as

$$\dot{m}_{ress}(t) = \frac{s(t)}{LVH} P_{batt}(t) \tag{2.17}$$

where $s(t)$ is the equivalence factor, which is used to assign a cost to electric energy, converting electric power into equivalent fuel consumption. The equivalence factor can be interpreted as the efficiency of which fuel is transformed into electrical power and vice-versa. Thus, $s(t)$ is a vector, one for charge and one for discharge,

$s(t) = [s_{chg}(t), s_{dis}(t)]$. In fact, the equivalence factor can be formulated as a constant, which represents the average overall efficiency of the electric path for a specific driving cycle [117].

The key to the effectiveness of this strategy is attributing a meaningful value to the equivalence factor. Clearly, its value affects the charge sustainability: according to (2.17), if the value of $s(t)$ is too high, the cost of using electric energy would be high, which makes the hybridization not fully realized; if, on the other hand, it is too low, the electric energy would be depleted fast. So both the vehicle fuel consumption and the evolution of the battery state of charge are dependent on the value of $s(t)$. It has been shown [125, 97, 96] that results obtained from ECMS can achieve comparable performance to those obtained from Dynamic Programming. The values of optimal equivalence factors are different for different driving cycles and they can be obtained only if the driving cycle is known a priori. This means that, despite its instantaneous property, ECMS still relies on information on future driving conditions. So it is reasonable to say that if the actual driving condition is too different from the one for which the strategy is tuned, the control still works but the performance is not as good as it could potentially be. The selection of the most suitable value of equivalence factor under different driving conditions to guarantee optimality is the challenge for ECMS.

If the perfect knowledge of future driving conditions is not available, equivalent consumption based strategy lends itself to suboptimal online implementable solutions providing that the equivalence factor is appropriately updated as driving conditions

change, which leads to adaptive equivalent consumption minimization strategy (A-ECMS). Based on the adaptation techniques, A-ECMS can be identified:

- Adaptation based on driving cycle prediction [125, 2, 47]: the best value of $s(t)$ is identified based on receding-horizon optimization with the help of the speed predictor. The optimization procedure for $s(t)$ is repeated every few minutes, using vehicle speed measurement and a simplified vehicle model embedded in the vehicle controller. This method introduces some approximation, but the equivalence factor is representative of present driving conditions and the overall process works well.

- Adaptation based on driving pattern recognition [55, 65, 54]: the suitable value of $s(t)$ is selected from the equivalent factor database by analysing the past driving conditions periodically and comparing with representative driving scenarios. This method takes advantage of the fact that the equivalence factors are similar for cycles with similar statistical properties. A pattern recognition algorithm is used to identify which kind of driving conditions the vehicle is undergoing, and select the most appropriate equivalence factors from a predefined set.

- Adaptation based on feedback from SOC [69, 27, 102]: the value of $s(t)$ is updated based on the SOC feedback and its variation from the desired SOC value. The idea is to maintain the SOC profile around the target value, which is usually a constant in a charge-sustaining HEV. In [69] and [27], the value of the equivalence factor is updated at each instant to account for the deviation of the state of charge from its reference value SOC_{set}. Instead of adapting continuously at each time step, [102] only updates equivalence factor regularly

with intervals of duration T, which allows SOC deviating from the reference value during the vehicle operation. Thus the charge-sustainability condition is enforced on shorter time frames.

Regardless of how the adaptation is performed, the A-ECMS methods enable the online implementation of optimization based supervisory control strategy. Though the results are suboptimal, performance that is comparable to those achieved by dynamic programming can be obtained with calibrations.

2.1.5 Model predictive control

Model predictive control (MPC) has been widely studied in the context of energy management strategy [101, 11, 37, 22, 68, 39] as an alternative optimal control method that may be implementable in real time. Where MPC differs from other controllers is that it solves the optimal control problem online for the current state of the plant, rather than providing the optimal control for all states, that is determining a feedback policy online. MPC computes the optimal control policy online using a finite-horizon prediction (of future conditions, i.e. road load, in the HEV energy management case). MPC classical schemes consider either a constant setpoint or a reference trajectory and are designed for rejecting disturbances. The controls are computed over a receding horizon by minimizing a criterion:

$$\begin{aligned} J(x(k)) = \min_{u(\cdot)} \{ & \sum_{i=0}^{p-1} ||x(k+i|k) - r(k+i)||^2_{w_i^x} \\ & + \sum_{i=0}^{m-1} ||u(k+i|k)||^2_{w_i^u} \} \end{aligned} \tag{2.18}$$

where $(m \leqslant p)$ p denotes the length of the prediction horizon or output horizon, and m denotes the length of the control horizon or input horizon; w_i^x and w_i^u are the

weighting factors at the i^{th} sample time; $r(k)$ is the vector of the state references; $u(\cdot) := [u(k)^T, \ldots, u(k+m-1|k)^T]^T$, $u(k) \in \Re^q$ is the sequence of manipulated variables to be optimized; $x(k) \in \Re^n$ denote the state prediction generated by the nominal model:

$$x(k+1) = Ax(k) + Bu(k), \quad x(0) = x_0 \tag{2.19}$$

$$\begin{cases} x(k) \in \mathcal{X} \\ u(k) \in \mathcal{U} \end{cases} \tag{2.20}$$

A receding horizon policy proceeds by implementing only the first control $u^*_{p,m}(k|k)$ to obtain $x(k+1) = Ax(k)+Bu^*_{p,m}(k|k)$. The rest of the control sequence $u^*_{p,m}(i|k), i = k+1, ..., k+m-1$ is discarded and $x(k+1)$ is used to update the optimization problem (2.18-2.20) as a new initial condition. This process is repeated, each time using only the first control action to obtain a new initial condition, then shifting the cost ahead one time step and repeating. This is the reason why MPC is also sometimes referred to as receding horizon control (RHC) or moving horizon control (MHC). The purpose of taking new measurements at each time step is to compensate for unmeasured disturbances and model inaccuracy, both of which cause the system output to be different from the one predicted by the model.

Three main difficulties arise when applying MPC to hybrid vehicle management. First of all, the system dynamics is mostly driven by the exogenous variable (i.e. driving conditions) that cannot be simply predicted over long horizon with a sufficient accuracy. Secondly, for classical MPC scheme, the minimal value of the criterion, usually in a quadratic form, is expressed as a function of the state. Therefore the

closed loop stability can be proved using a Lyapunov function [45]. For hybrid vehicle application, the criterion is the fuel consumption which is a nonlinear function of the control and the exogenous variables. Even without initial state error,the minimal cost differs from zero since it is not directly related to the battery state of charge but to the fuel consumption. The stability of a MPC scheme is therefore more difficult to prove. Last but not the least, it is difficult to design the reference trajectory of the state (or output). Most of the existing control strategies consider a constant setpoint for the battery state of charge. Although this goal is acceptable for a long horizon, it is useless for a short horizon.

However, as a potentially real-time implementable optimal control based approach, MPC has been studied and applied in the field of HEV energy management. With the advent of in-vehicle navigation systems that make use of GPS and digital mapping technologies, it is reasonable to presume that predicting future road loads over a short horizon can in fact be achieved with acceptable accuracy.

2.2 Battery aging

Lithium-ion (Li-ion) batteries are the preferred energy storage technology in xEVs due to their high energy and power density. For the applications in automobile, which require durability and stability, the long-term cycling and storage behaviour becomes of increasing interest. However, battery health is one of the main uncertainties in the total life-cycle cost of advanced energy storage systems. Therefore aging of lithium-ion batteries as well as health management have been and are the subject of a great

amount of research (e.g.:[145, 3, 18, 56, 32, 58, 114, 46]). A brief overview of these aging mechanism is provided in the next few paragraphs.

In general, aging of battery is demonstrated by a reduction in the ability to store energy and deliver power, which is correlated with loss in capacity and increase in internal resistance. Aging mechanisms occurring at anodes and cathodes differ significantly. One major source of aging at the anode is due to the reactions between the electrolyte and the anode resulting in the formulation of a "protective layer", which is known as solid electrolyte interface (SEI) [6, 8, 9, 76]. During charging, the electrochemical status of the electrolyte components is out of the stable range, hence, reductive electrolyte decomposition together with irreversible consumption of lithium ions takes place at the electrode/electrolyte interface. The decomposition process as well as the product of the process, e.g. SEI formation and growth, contributes to the aging of the battery anode. The presence of SEI leads to an increase of impedance, which is the major cause of power fading. With the growth of SEI, more and more active or mobile lithium is lost, leading to self-discharge and irreversible capacity degradation. SEI growth proceeds through the whole life of the battery, e.g. cycling and storage, and the rate of the process is subjected to many factors such as temperature, rate of current and depth of discharge. According to the study from [84, 139, 33], capacity fade is primarily the result of loss of active lithium that is most likely associated with anode degradation.

Another cause of degradation in a battery is related to cathode materials and structures. Lithium manganese oxides ($LiMn_2O_4$) with spinel structure, lithium

nickel cobalt mixed oxides $[Li(Ni, Co)O_2]$ with layered structures as well as lithium iron phosphate ($LiFePO_4$) based lithium ion batteries have been considered as promising candidates for large scale applications in the automotive and space industries due to cost, availability and performance. Basic aging mechanisms under cycling and different storage conditions for the above types of cathode materials are: (i) loss of positive active materials, (ii) changing of electrode composition due to electrochemical reactions or corrosion, (iii) oxidation of the electrolyte and (iv) aging products interaction with the anode. These aging effects have a strong correlation with each other and cannot be analysed independently [7, 10, 36, 99, 100].

Being aware of the health of the battery helps in making timely life cycle management decisions, reducing warranty and maintenance costs while improving serviceability, availability and safety, and it is possible only when an aging model describing the evolution of aging over time/cycle is available. Aging models for lithium-ion batteries can be classified into two categories, namely, physical-chemical models and empirical models. Physical-chemical models are usually developed to study or describe a single aging mechanism inside the cell [121, 150, 90, 91, 89]. The literature on physical-chemical based modeling of lithium ion batteries is quite extensive. Analytic expressions for the specific capacity against discharge rate were presented by [40]. The first model with two composite electrodes and a separator was presented by [48] and was further extended to account for the decay in capacity of the cell with cycle number by [121] based on a continuous occurrence of a very slow solvent diffusion/reduction near the surface of the negative electrode when the cell is in charge mode. Further extensions to this model were made in [136] by including the effect

of porosity change of the intercalation material on capacity fade. The single particle model was presents by [99], in which each electrode is represented by a single spherical particle. While the physical-chemical models have the advantage of providing a sophisticated account of the various physical processes occurring in a battery, solving the model is very time-consuming. Ideally, one would expect for such model that is not computationally heavy and it provides a realistic portrait of the physical processes occurred during cycling.

Due to its simplicity but still good accuracy, semi-empirical models have been used for on-line battery prognosis, estimation of state-of-health as well as design of battery management system. Recently, semi-empirical models have been also used for optimal HEV energy management strategy with consideration of battery aging [133, 144] and for the study of aging propagation among cells in advanced battery systems [35]. Various empirical and semi-empirical models have been proposed [20, 122, 147, 34]. These models are developed with consideration of simplified physical relations in the model by fitting the parameters of the model with experimental data obtained from aging tests (process shown in Fig.2.1 [51]), resulting in a set of equations that describe the main degradation mechanisms. In [20], accelerated calendar and cycle life of Li-ion battery is studied, which shows that useful life was strongly affected by temperature, time, state-of-charge and change in state-of-charge (ΔSOC). To estimate the percentage of power loss the data were fit with the general equation:

$$Q = A \cdot exp(\frac{-E_a}{R \cdot T})t^z \tag{2.21}$$

where Q represents the percentage power loss, t the time, T the temperature in Kevin, A the pre-exponential factor, E_a the activation energy in Jmol^{-1}, R the gas constant and z the adjustable parameter. In [122], semi-empirical correlations for two capacity fade parameters are developed to predict the performance of the battery as a function of number of cycles:

$$\theta_n^N = \theta_n^0 - k_1(cycle)^{\frac{1}{2}} \tag{2.22}$$

$$R_f^N = R_f^0 - k_2(cycle)^{\frac{1}{2}} \tag{2.23}$$

where θ_n the available active charge at negative electrode, R_f the film resistance, the constant k_1 and k_2 depend on cycling conditions and the type of negative electrode material used. A semi-empirical capacity degradation model is proposed in [147] based on the results from an accelerated cycle life study, which is an extension of the work from [20]. Instead of using time, the authors chose Ah-throughput as a parameter for the life modeling. Ah-throughput represents the amount of charge delivered by the battery during cycling. The function form of the life model can be expressed as:

$$Q_{loss} = B \cdot exp(\frac{-31700 + 370.3 \cdot C_{rate}}{R \cdot T})(Ah)^{0.55} \tag{2.24}$$

where Q_{loss} the percentage of capacity loss, B the pre-exponential factor, R the gas constant, T the absolute temperature.

Despite the efforts reported in the literature, there is still the need to understand battery aging under more realistic HEV operations. In particular, the development of accurate aging models that are able to assess and predict the life of the Li-ion batteries under realistic automotive scenarios is critical. Due to the favorable compromise

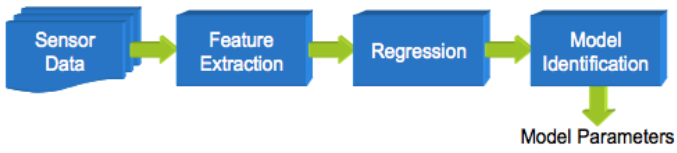

Figure 2.1: Schematic of Semi-empirical Model Development

between simplicity and accuracy, a semi-empirical model is employed in the control-oriented models used in this dissertation and the details of this model are described in the following chapter.

2.3 Energy Management Strategy Integrated with Battery Health

The performance, reliability, and cost effectiveness of all electrified vehicles are highly dependent on the selection, integration, control and health of the on-board energy storage systems. For example, the fuel economy, recuperation capability, and drivability of hybrid and electric vehicles are significantly influenced by the specific power and energy capacity of their ESSs [124, 148, 152]. Additional focus and concerns from both the automotive manufactures and customers are the lifetime and safety issues of ESSs [44, 94, 67]. Thus, aimed at satisfying the energy and power requirements of the vehicle simultaneously, most of the designs lead to the oversizing of either of them. The oversized designs cause expensive, heavy, and voluminous ESSs. Indeed, many studies have been performed on how to optimally size the drivetrain components, particularly the battery [5, 49, 149, 71, 42, 95, 119]. However, batteries experience irreversible power fade and capacity decay as they age, and therefore the performance of the electrified vehicles will be negatively influenced even with an

optimally sized battery pack. The rate of battery aging is dictated by many factors including operating and environmental conditions. Factors such as extreme temperature, high C-rate, high or low state of charge and excessive depth of discharge, which are closely related to the vehicle operation strategy, are recognized to contribute to capacity degradation.

It stands to reason that one would want to consider strategies for limiting battery aging in the design of HEV control algorithms. However, limiting stresses on the battery that could accelerate its aging may result in energy management policies that are in conflict with the desire to minimize fuel consumption. Mathematically, this situation can be described as a multi-objective optimization problem. In [93], a multi-objective optimal control problem is formulated, which seeks to manage power flow in a power-split PHEV to minimize both health degradation and energy consumption cost. The authors quantify the aging effect of the battery by anode side resistive film formation. Thus, the rate of capacity loss is characterized by the growth rate of the film thickness:

$$\frac{\partial \delta_{film}}{\partial t} \tag{2.25}$$

which depends on the chemistry of the electrode and electrolyte. The control objective function is then formulated as

$$\min \sum_{k=0}^{N} \alpha \cdot c_E + (1-\alpha) \cdot c_H \tag{2.26}$$

$$c_E = \beta \cdot W_{fuel} + \frac{-V_{oc} Q_{batt} \dot{SOC}}{\eta_{EVSE}} \tag{2.27}$$

$$c_H = \frac{\partial \delta_{film}}{\partial t} \tag{2.28}$$

where α the weighting factor, c_E the instantaneous energy consumption cost, which includes both fuel and grid charging costs, β the relative price of gasoline per MJ to the price of grid electricity per MJ, c_H the battery capacity loss rate. The optimal control problem is solved by Stochastic Dynamic Programming (SDP), and the simulation results show that a PHEV power management strategy that considers SEI film growth in addition to energy consumption will deplete battery charge quickly to reduce film growth rates and blend engine and battery power to avoid charge sustenance. An approach to take into account battery aging in energy management strategies for HEVs is presented in [133], in which the aging effect is quantified by battery effective Ah-throughput:

$$Ah_{eff} = \int_0^{t_f} \sigma \cdot |I_{batt}| dt \tag{2.29}$$

in which σ is severity factor that characterizes the cycling conditions.The proposed cost function takes the form of

$$J = \int_0^{t_f} (1-\alpha) \cdot \dot{m}_f + \alpha \cdot c_a \cdot \frac{1}{\Gamma} \cdot \sigma \cdot |I_{batt}| dt \tag{2.30}$$

where α the weighting factor, $\dot{m}_f$ the fuel flow rate, c_a the transformation coefficient of the battery wear, to make it dimensionally compatible with the fuel consumption by expressing the two costs in terms of monetary expense. This strategy is solved by Pontryagin's Minimum Principle, which shows that battery life can be extended with a compromise on fuel economy. Instead of explicitly including battery aging in the cost function, the authors of [43] chose to treat battery state-of-health

as one of the states in the optimal control problem. Assuming that a battery can withstand a certain amount of energy throughput before it reaches its end-of-life, a throughput-based capacity fade model is adopted:

$$\dot{SOH} = -\frac{P_{batt}}{2 \cdot N \cdot Q_0} \tag{2.31}$$

where N the total number of cycles before end-of-life, which is a function of battery power P_{batt}, and Q_0 the battery nominal energy capacity. The strategy is solved by ECMS-based method by tracking prescribed profiles for both battery SOC and SOH. In [146], an energy management strategies of a hybrid vehicle with hybrid storage system is discussed, where a battery is coupled with a capacitor. Battery aging effect is considered by taking into account the battery RMS current, which is equivalent to a minimization of the integrated square of the battery current along the cycle. Thus the objective function takes the form of

$$J = \int_0^T C(t) + K_{ibatt} \cdot I_{batt}^2(t) dt \tag{2.32}$$

where C the fuel consumption and K_{ibatt} the weighting factor. Pontryagins Minimum Principle is applied to solve the optimal control problem and the results indicate that a good compromise may be found when increasing fuel consumption by a small amount while significantly decreasing the battery RMS current and thus battery aging. Given the fact that temperature is one of the most influential factors contributing to battery aging, an energy management strategy for electrified vehicles taking into account battery health through an additional cost on battery internal temperature is presented in [107], in which the control objective is to minimize:

$$J = \int_{t_1}^{t_2} \dot{m}_f(t) + \kappa(t) \cdot \dot{T}_{cell}(t) dt \tag{2.33}$$

where $\dot{m}_f$ is the instantaneous fuel consumption, $\dot{T}_{cell}$ is the battery cell temperature κ is a weighting parameter depending on the cell temperature. PMP-based simulation results highlight the fact that the strategy is not promising in saving battery life.

Battery health management is particularly challenging for two reasons. First, the most critical damage mechanisms are still not fully understood. Therefore, broad ranges of degradation models are studied and incorporated in power management formulation techniques. Second, the dynamics are simulated using computationally intensive electrochemical models that are incompatible to control design. Moreover, energy management strategy for xEVs is, by itself, a nontrivial problem that requires the solution of an optimal control problem with multiple inputs, disturbances, states and control constraints.

Given the fact that Dynamic Programming is the only optimal control approach that can guarantee global optimality with any level of problem complexity, the solutions generated by Dynamic Programming are always studied as the benchmark in this dissertation. Pontryagin's Minimum Principle, as an analytical approach and instantaneous minimization method, is of great interest to gain insights on design of the real-time implementable control strategy. Combining the results from Dynamic Programming and PMP, an Adaptive ECMS based real-time energy management

strategy is developed. Thus, this dissertation offers the evolution of an energy management problem from global optimal but noncausal to suboptimal but real-time implementable.

Chapter 3: Model Development

This chapter provides a detailed overview of the modeling work linked to the development and simulation of energy management strategies. The main objective is to reproduce the energy flows within the powertrain and the vehicle, in order to obtain an accurate estimation of fuel consumption and battery state of charge, based on the road load and control inputs. Since energy analysis is the primary goal, efficiency considerations are at the basis of the models described.

3.1 HEV Powertrain

3.1.1 Powertrain architecture description

The vehicle under investigation is a pre-transmission parallel HEV passenger car. Fig. 3.1 illustrate the configuration of the powertrain architecture, which consists of a battery pack, an electric machine, an internal combustion engine and a continuously variable transmission (CVT). The engine and electric machine are mounted on the same shaft which connects to the CVT through a torque damper. The main characteristics of the components are listed in Table 3.1. The hybrid function attached to this configuration includes engine start-stop, torque assist and regenerative braking.

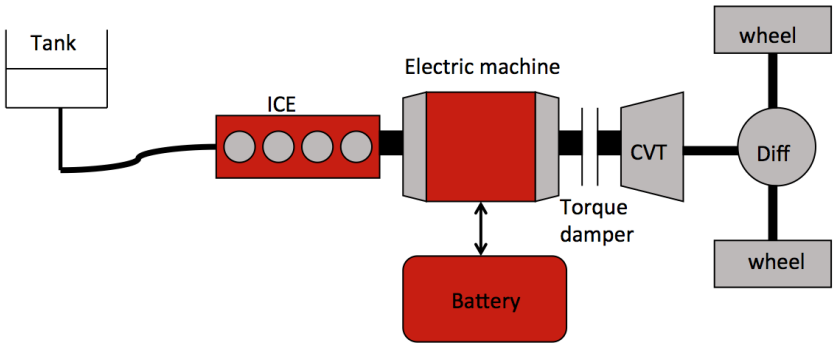

Figure 3.1: Vehicle Architecture

Table 3.1: Components Specifications

Components	**Specification**
Vehicle Mass	1294 kg
IC Engine	1.6 liter 85 kW gasoline engine
Electric Machine	15 kW
CVT	Ratio: 3.172∼0.529
Final drive	Ratio: 2.7
Battery Pack	Li-ion 820 Wh, 4.6 Ah, 20 kW

3.1.2 Vehicle road load model

Since the primary objective is to develop an understanding of the vehicle longitudinal dynamics and of the energy characteristics of hybrid vehicles, the vehicle is considered as a point mass. Thus the motion equation can be written from the equilibrium forces shown in Figure 3.2:

$$M_{veh}\frac{dv_{veh}}{dt} = F_{intertia} = F_{trac} - F_{roll} - F_{aero} - F_{grade} \tag{3.1}$$

where M_{veh} is the effective vehicle mass, v_{veh} is the longitudinal vehicle velocity, $F_{inertia}$ is the inertial force, $F_{trac} = F_{pwt} - F_{brake}$ is the tractive force generated by the powertrain and the brakes at the wheels, F_{roll} is the rolling resistance, F_{areo} is the aerodynamic resistance, F_{grade} the force due to road slope.

The aerodynamic resistance is expressed as

$$F_{aero} = \frac{1}{2}\rho_{air}A_f C_d v_{veh}^2 \tag{3.2}$$

where ρ_{air} is the air density, A_f the vehicle frontal area, C_d the aerodynamic drag coefficient.

The rolling resistance force is modeled as

$$F_{roll} = C_{roll}M_{veh}g\cos\delta \tag{3.3}$$

where g is the gravity acceleration, δ the road slope angle, and C_{roll} the rolling resistance coefficient.

The grade force is the horizontal component of the vehicle weight, which is calculated as the following:

$$F_{grade} = M_{veh}g\sin\delta \tag{3.4}$$

The values of the vehicle dynamics parameters are listed in Table 3.2.

3.1.3 Engine

The engine used in this work is an 1.6L in-line four cylinder spark ignition gasoline engine.There are many modeling approaches used for an internal combustion engine,

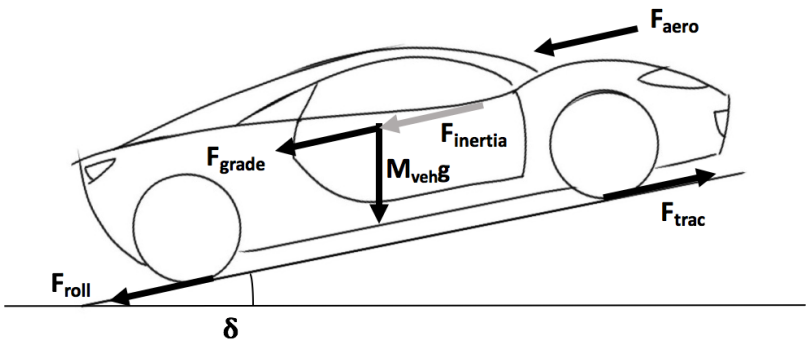

Figure 3.2: Forces Acting on a Vehicle

Table 3.2: Vehicle Parameters

Parameter	Value	Unit
ρ_{air}	1.29	kg/m^3
A_f	2	m^2
C_d	0.27	-
C_{roll}	0.015	-
g	9.81	m/s^2
δ	0	degree

for instance, static map, mean-value model and one-dimensional fluid-dynamic model. In this study, the static map approach is adopted, which assumes the engine to be a perfect actuator, which responds immediately to the commands. The fuel flow rate is computed using a map or table as a function of both engine speed ω_{ice} and torque T_{ice}, which are supposed to be known:

$$\dot{m}_f = f(\omega_{ice}, T_{ice}) \tag{3.5}$$

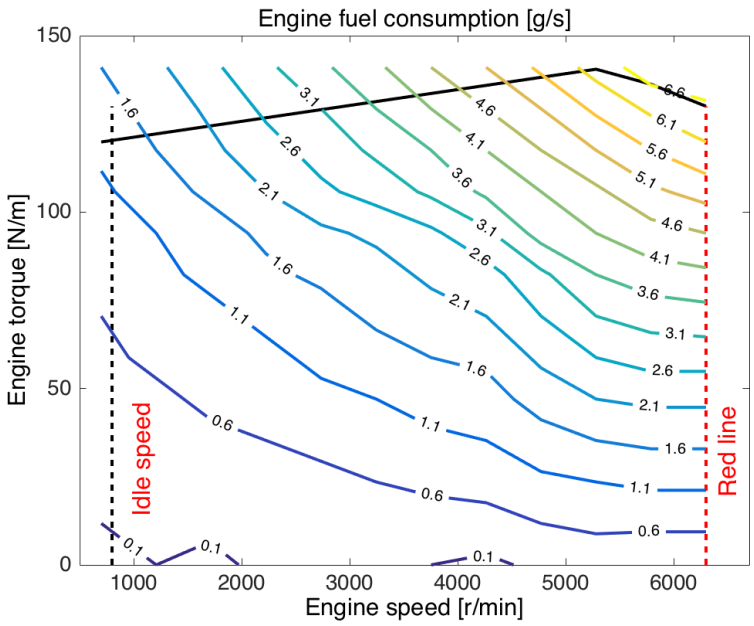

Figure 3.3: 1.6L Engine Fuel Flow Rate Map

In particular, the torque is usually a control input for the engine, while the speed is a measured input and derives from the vehicle wheel speed. A curve that gives the maximum engine torque as a function of the current speed is also included in this kind of model to ensure that the torque does not exceed the limits of the engine:

$$0 \leqslant T_{ice} \leqslant T_{ice_{max}}(\omega_{ice}) \tag{3.6}$$

In addition to the torque limit, engine speed limits should be respected as well:

$$\omega_{ice_{idle}} \leqslant \omega_{ice} \leqslant \omega_{ice_{redline}} \tag{3.7}$$

Figure 3.3 shows the fuel flow rate map of the engine used in this study. The engine data is from Powertrain System Analysis Toolkit©(PSAT).

3.1.4 Electric machine

A permanent magnet synchronized electric machine is studied, which has continuous power of 15 kW and peak power of 30 kW. Electric machines can be modeled using an approach similar to the one used for the engine, i.e., based on maps of torque and efficiency. Desired values of electrical power or torque can be used as a control input. The relation between torque at the shaft and electric power is provided by an efficiency map (Figure 3.4), which is a function of speed and torque:

$$\eta_{em} = f(\omega_{em}, T_{em}) \tag{3.8}$$

Therefore the power request of the electric is given by

$$P_{em_{req}} = T_{em} \cdot \omega_{em} \cdot \eta_{em}^{z}(\omega_{em}, T_{em}) \tag{3.9}$$

in which $z = -1$ when electric machine is a motor or the power request is positive, otherwise $z = 1$.The operation of the electric machine is limited by its minimum and maximum torque curve, as well as by its extreme speed:

$$T_{em_{min}}(\omega_{em}) \leqslant T_{em} \leqslant T_{em_{max}}(\omega_{em}) \tag{3.10}$$

$$\omega_{em_{min}} \leqslant \omega_{em} \leqslant \omega_{em_{max}} \tag{3.11}$$

3.1.5 Continuously variable transmission

A Continuously Variable Transmission (CVT) provides an infinite number of transmission gear ratios within the limits of the device. This is in contrast to an

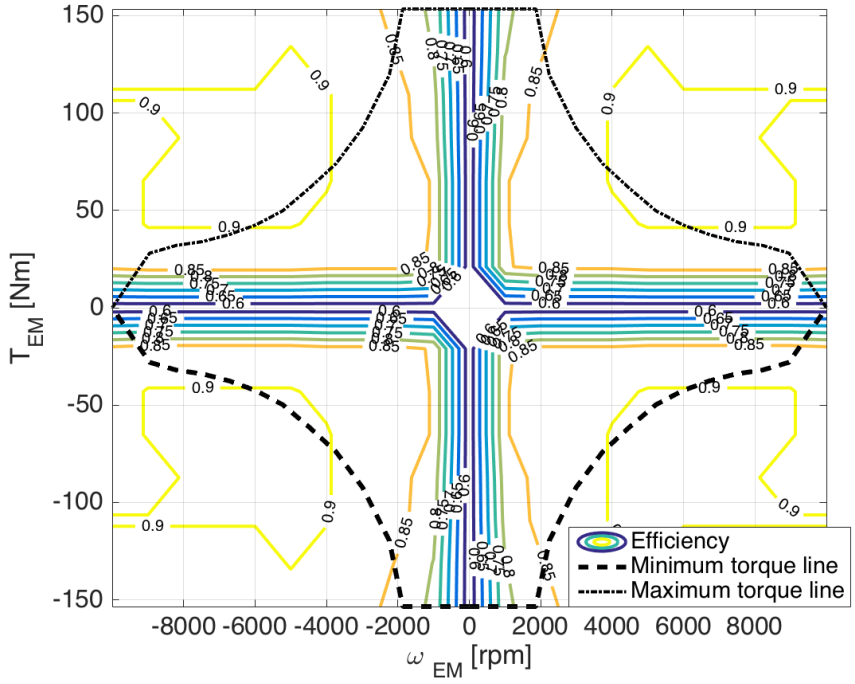

Figure 3.4: Electric Machine Efficiency Map

automatic or manual transmission that typically offers five or six gear choices. For energy analysis, a simple model that accounts for speed and torque ratios with a constant efficiency is adopted. The following speed relationship is always held:

$$\omega_{out} = \frac{\omega_{in}}{r_{cvt}} \tag{3.12}$$

in which ω_{in} is the CVT input speed, ω_{out} is the output speed and r_{cvt} is the CVT ratio. The torque model is described as:

$$T_{out} = \begin{cases} T_{in} \cdot r_{cvt} \cdot \eta_{cvt} & \text{if } T_{in}\omega_{in} \geq 0; \\ \frac{T_{in} \cdot r_{cvt}}{\eta_{cvt}} & \text{if } T_{in}\omega_{in} < 0. \end{cases} \tag{3.13}$$

with the convention that power flow is positive when going from input to output. T_{in} and T_{out} are defined as CVT input torque and output torque respectively, and η_{cvt} is the CVT efficiency. The CVT ratio should be bounded by it minimum and maximum values:

$$r_{cvt_{min}} \leqslant r_{cvt} \leqslant r_{cvt_{max}} \tag{3.14}$$

3.2 Li-ion Battery Pack

Battery models have become an indispensable tool for the design of battery-powered systems. Their uses include battery characterization, state-of-charge and state-of-health (SOH) estimation, algorithm development, system-level optimization, and real-time simulation for battery management system design.

Electrochemical energy storage systems, a battery pack in this study, are key components of hybrid electric vehicles. The battery model contains an electric model, a lumped thermal model, and a semi-empirical capacity degradation model, which is

Figure 3.5: Battery Cell

linked to the optimal control studies. All the parameters are based on $LiFePO_4$ cell from A123 system. The specifications of the battery cell are listed in Table 3.3.

Table 3.3: Battery Cell Specifications

Name	ANR26650
Type	Nanophosphate Li-ion
Cell Geometry	Cylindrical (Figure 3.5)
Manufacture	A123 Systems
Nominal Voltage of Cell	3.3 V
Nominal Capacity of Cell	2.3 Ah

3.2.1 Battery electrical model

Battery models based on equivalent circuits [120] are preferred for system-level development and controls applications due to their relative simplicity. Engineers use equivalent circuits to model the thermo-electric behavior of batteries, parameterizing

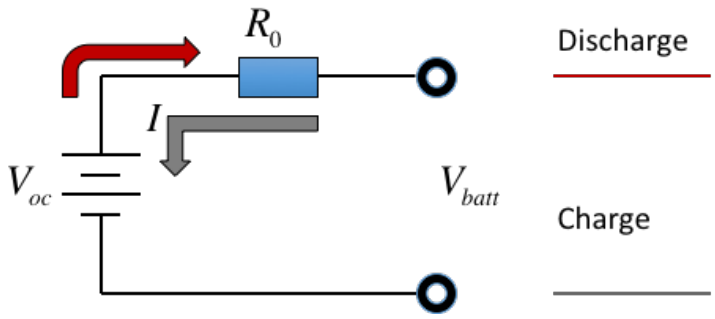

Figure 3.6: 0^{th}-order Equivalent Circuit

their nonlinear elements with correlation techniques that combine models and experimental measurements via optimization.

A battery system consists of battery cells (Figure 3.5). Depending on the requirements of output voltage and power and energy capacities for the designed hybrid vehicle system, a battery is configured by many cells connected in series or parallel or both. In this study, a 0^{th}-order equivalent circuit model is used, which comprises a voltage source V_{oc} and an internal resistance R_0 in series (Figure 3.6). The open circuit voltage is a function of battery state of charge (SOC) (Figure 3.7), while the internal resistance is a function of both battery SOC and temperature, θ_{batt}, as shown in Figure 3.8.

$$V_{OC} = f(SOC) \tag{3.15}$$

$$R_0 = f(SOC, \theta_{batt}) \tag{3.16}$$

Based on the equivalent circuit and Ohms law, the cell current can be expressed by [133]

$$I_{cell}(t) = \frac{V_{oc} - \sqrt{V_{oc}^2 - 4 \cdot R_0 \cdot P_{cell}(t)}}{2 \cdot R_0} \tag{3.17}$$

in which P_{cell} is cell power in Watt. Thus, battery SOC, which is the main dynamics of the optimal control problem, is calculated as

$$SOC(t) = SOC_0 - \frac{1}{Q_{cell} \cdot 3600} \cdot \int_0^t I_{cell}(\tau) \cdot \eta_{batt}(sign[I_{cell}(\tau)]) d\tau \tag{3.18}$$

with the convention that I_{cell} is positive when discharging. SOC_0 is the initial value of SOC and Q_{cell} is the nominal cell capacity in ampere-hours. η_{batt} is the Coulombic efficiency, which is dependent on the sign of current.

Assuming that each cell is identical in the battery pack, the battery current and power can be described as

$$I_{batt} = I_{cell} \cdot N_p \tag{3.19}$$

$$P_{batt} = P_{cell} \cdot N_p \cdot N_s \tag{3.20}$$

in which N_p and N_s are number of cell in parallel and number of cell in series respectively. In this study, $N_p = 2$ and $N_s = 54$ resulting in total nominal battery energy capacity of 0.82 kWh.

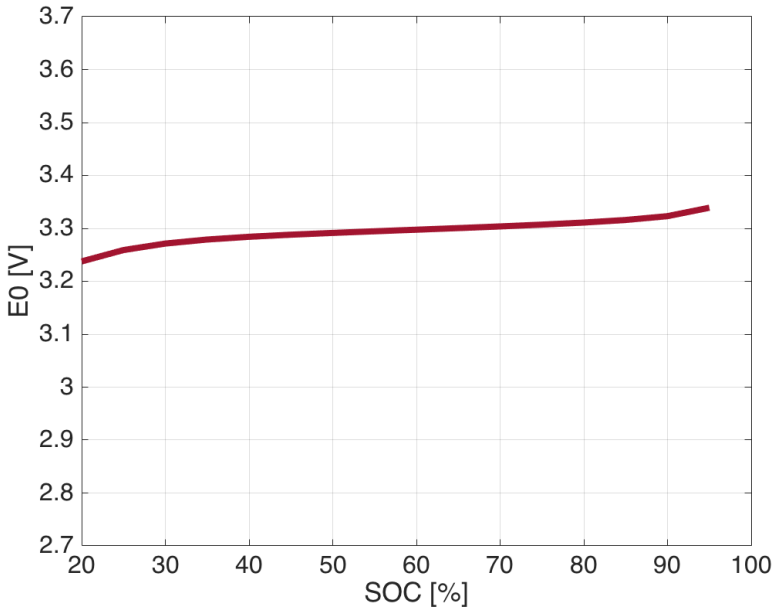

Figure 3.7: Cell Open Circuit Voltage

3.2.2 Battery thermal model

Based on the electric circuit model and thermal dynamics of the battery , the power generating heat and battery temperature can be calculated from the equations,

$$\dot{q}_{batt} = R_0 \cdot I_{cell}^2 \cdot N_s \cdot N_p \tag{3.21}$$

$$\dot{\theta}_{batt} = \frac{\dot{q}_{batt} + h_{batt} \cdot A_{surface} \cdot (\theta_{cool} - \theta_{batt})}{M_{batt} \cdot C_{p_{batt}}} \tag{3.22}$$

where all the parameters and values are listed in Table

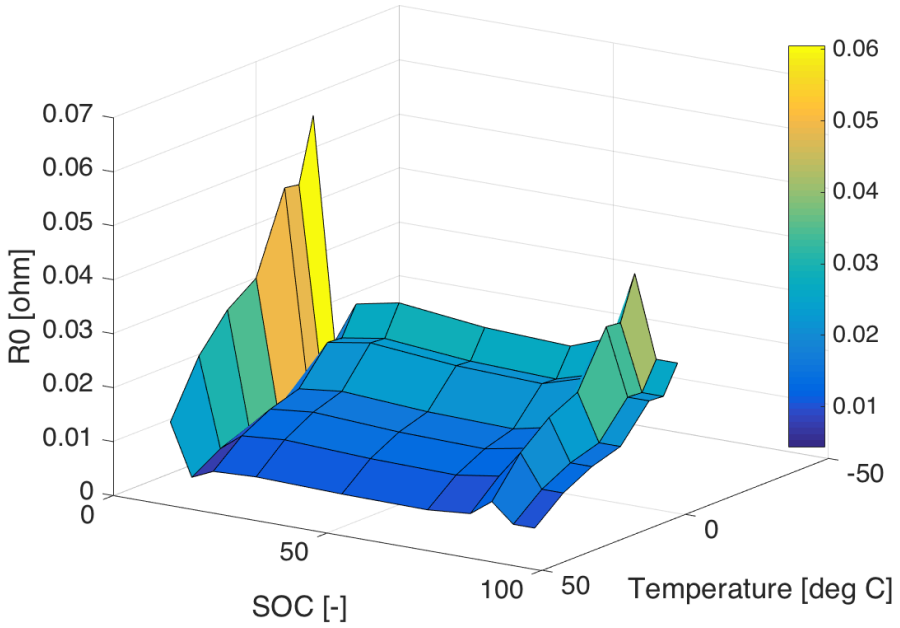

(a) R0, charging

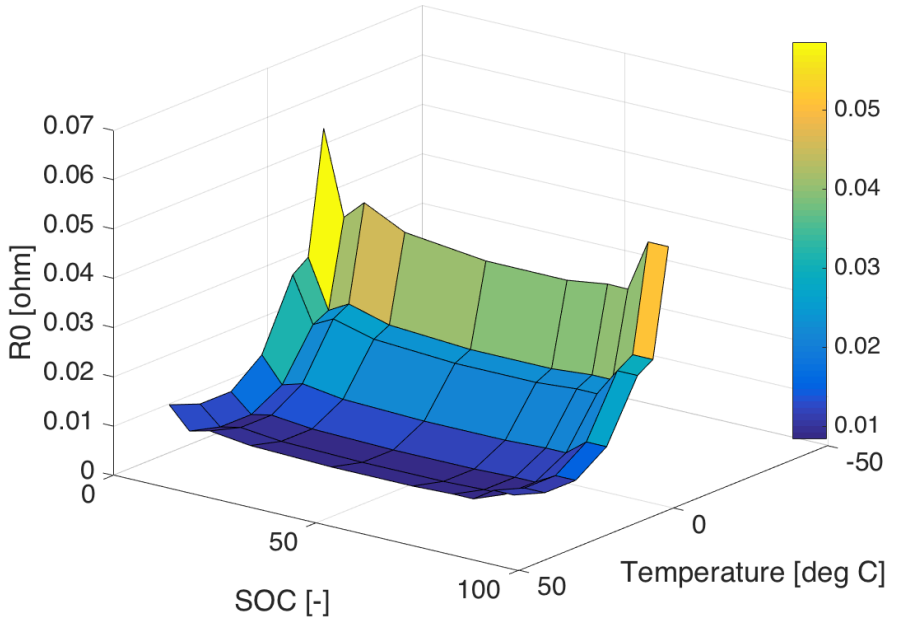

(b) R0, discharging

Figure 3.8: Cell Internal Resistance

Table 3.4: Battery Thermal Model Parameters

Parameter	Description	Value	Unit
h_{batt}	Heat transfer coefficient	30	$W/m^2 \cdot K$
$A_{surface}$	Battery surface area	0.32	m^2
M_{batt}	Pack mass	7.88	kg
$C_{p_{batt}}$	Specific heat	825	$J/kg \cdot K$
θ_{cool}	Coolant temperature	Depending on environment	°C

3.2.3 Battery capacity degradation model

Battery aging, resulting in capacity decay and internal resistance increase, originates from multiple and complex mechanisms. In HEV/EV applications, there are two aging situations: storage and cycling. The focus of this study is on reducing battery capacity degradation during vehicle operation, so a control-oriented cycling capacity loss model is introduced in this section.

Table 3.5: Battery Aging Experiment Data

DATA	$S\bar{O}C[\%]$	$\bar{I}_c[1/h]$	$\bar{\theta}[^\circ\mathrm{C}]$
Profile A	38.5	2.8	36
Profile B	42.0	3.0	38
Profile C	68.0	6.0	45

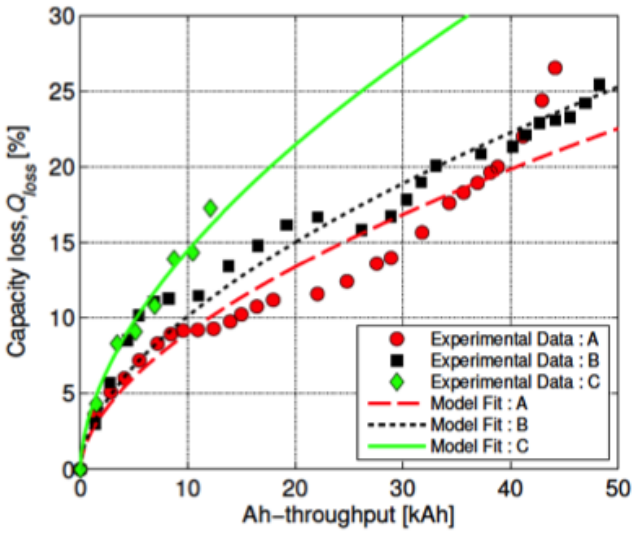

Figure 3.9: Curve fitting result of identified aging model with the experimental data [141]

Aging models for lithium-ion batteries can be classified into two categories, namely, physical-chemical models and empirical models. Physical-chemical models are usually developed to study or describe a single aging mechanism inside the cell [91, 90]. For instance, a first-principles capacity fade model is developed based on the mechanism for SEI growth [121]. This type of models are helpful in understanding of aging under different modes as well as the effect of an aging source on different aspects of the cell performance. Such first-principles models have limitations such as the requirement of a detailed model of the aging processes and often require long computation time. To remedy these shortcomings, various empirical and semi-empirical models have been proposed [20, 34], These models are developed by considering simplified physical relations in the model by fitting the parameters of the model with experimental data obtained from aging tests, resulting in a set of equations that describe the main degradation mechanisms. Due to the favorable compromise between simplicity and accuracy, semi-empirical models are employed in the control-oriented models used in this study. We start from a generic model initially proposed in [147], which has the form

$$Q_{loss} = B \cdot exp(\frac{-E_a}{R \cdot \theta}) \cdot (Ah)^z \tag{3.23}$$

where Q_{loss} is the battery capacity loss in percentage with respect to the nominal capacity, B is a pre-exponential factor, E_a is the activation energy in $J \cdot mol^{-1}$, R is the gas constant, θ is the battery temperature expressed in Kelvin, Ah is the Ah-throughput, and z is the power law factor.

The cycle life of the battery is usually characterized in a laboratory setting where the battery is subjected to standard or synthetic test profiles that do not necessarily

mimic real cycling conditions. In order to capture the battery aging effects under HEV operating conditions as well as to incorporate dependence on SOC, the generic aging model is calibrated on battery aging data obtained from a charge sustaining HEV, and the data is reported in Table 3.5 where profile A and B are from [53] and profile C is from [137]. The data of profile A represents the battery operation in an actual city driving conditions in Gothenburg, Sweden, whereas profile B illustrates battery usage in a load cycle designed over a stochastic process model for HEVs. The data of profile C is an outcome of experimental test of batteries with load conditions from a real HEV driving cycle. The three profiles use the same type of battery, which is $LiFePO_4$ cell (ANR26650) from A123 system, and are specified in terms of average state of charge, $S\bar{O}C$, average C-rate, $\bar{I}_c$ and average battery temperature, $\bar{\theta}$. Following a two-step curve fitting procedure, the result is shown in Fig.3.9 and the identified aging model [141] has the form of

$$Q_{loss.\%} = (\alpha \cdot SOC + \beta) \cdot exp(\frac{-31700 + 163.3 \cdot I_c}{R \cdot \theta}) \cdot Ah^{0.57} \tag{3.24}$$

$$\alpha = \begin{cases} 1287.6, & SOC \leqslant 0.45 \\ 1385.5, & SOC > 0.45 \end{cases}$$
$$\beta = \begin{cases} 6356.3, & SOC \leqslant 0.45 \\ 4193.2, & SOC > 0.45 \end{cases}$$

3.3 Vehicle cabin and battery thermal model

When a vehicle is parked under a clear sky, the thermal load due to solar radiation may be greater than the load due to conduction between the surroundings and the vehicle cabin especially in summer, which makes the battery experience higher temperature than the ambient temperature. Cabin thermal models have been developed

using numerical methods and lumped-parameter approaches to design, analyze and control of air conditioning (AC) systems for passenger thermal comfort, reduction of fuel consumption and tailpipe emissions and so on. In the context of studying the impact of temperature on battery life in a parked vehicle , lumped-parameter approaches have been adopted. A lumped capacitance thermal network approach is used to model the vehicle cabin and battery thermal model [98], which is illustrated in Fig. 3.10. The solar radiation load $\dot{Q}_{rad}$ has three components, which are direct radiation $\dot{Q}_{dir}$, diffuse radiation $\dot{Q}_{diff}$ and reflected radiation $\dot{Q}_{ref}$. The mathematical models for each are described in the following section. The vehicle cabin and battery thermal models are described in equation (3.25) and (3.26). All the parameters are calculated based on a regular sedan [98] and listed in Table 3.6.

$$M_{cab} \cdot \dot{\theta}_{cab} = \dot{Q}_{rad} + \frac{1}{K_{ac}}(\theta_{amb} - \theta_{cab}) + \frac{1}{K_{bc}}(\theta_{batt} - \theta_{cab}) \tag{3.25}$$

$$\begin{aligned} M_{batt} \cdot \dot{\theta}_{batt} = & \dot{q}_{batt} + \frac{1}{K_{bc}}(\theta_{cab} - \theta_{batt}) + \frac{1}{K_{ab}}(\theta_{amb} - \theta_{batt}) \\ & + U \cdot (\theta_{cool} - \theta_{batt}) \end{aligned} \tag{3.26}$$

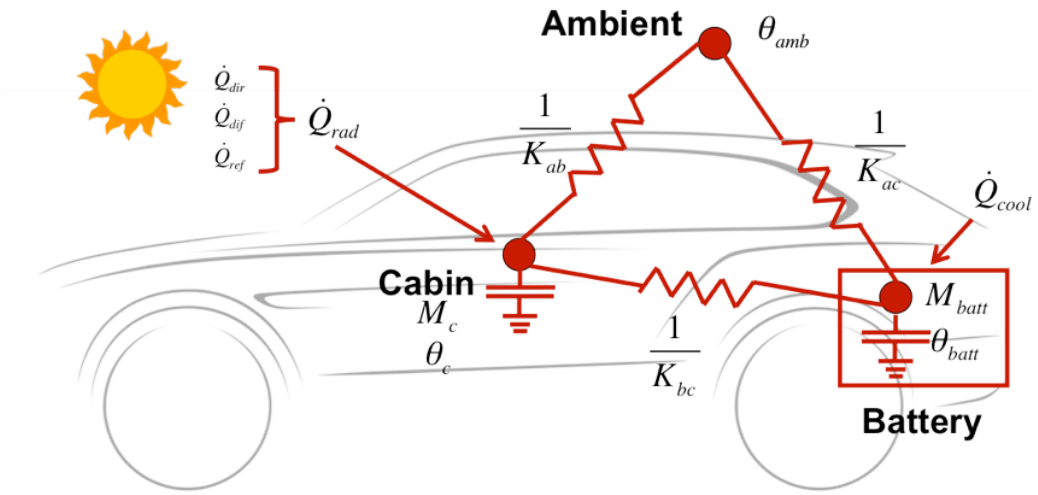

Figure 3.10: Vehicle Cabin and Battery Thermal Load

Table 3.6: Vehicle Cabin and Battery Thermal Model Parameters

Parameters	**Description**	**Value**
$\dot{Q}_{rad}$	Solar radiation load	Time and location dependent
$\dot{q}_{batt}$	Heat generated by battery	Control input
θ_{amb}	Ambient temperature	Time and location dependent
θ_{cab}	Cabin temperature	Output of model
θ_{batt}	Battery temperature	Output of model
θ_{cool}	Coolant temperature	25 °C
M_{cab}	Thermal mass of Vehicle cabin	10177 J/K
M_{batt}	Thermal mass of battery pack	52827 J/K
K_{ac}	Effective heat transfer coefficient between ambient and cabin	1.316 W/K
K_{bc}	Effective heat transfer coefficient between battery and cabin	0.753 W/K
K_{ab}	Effective heat transfer coefficient between ambient and battery	0.511 W/K
U	Effective heat transfer coefficient between battery and cooling system	Fan setting dependent

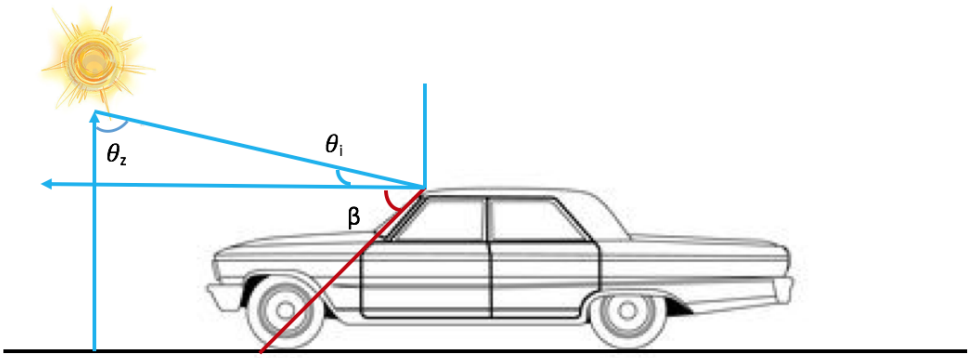

Figure 3.11: Representation of the direct solar radiation component

3.3.1 Solar radiation load

The solar radiation load $\dot{Q}_{rad}$ consists of direct solar radiation $\dot{Q}_{dir}$, diffuse solar radiation $\dot{Q}_{diff}$ and radiation reflected by road $\dot{Q}_{ref}$. Each of them is calculated as [70]:

$$\dot{Q}_{dir} = \sum_{surface} S \cdot \tau \cdot \dot{I}_{dir} \tag{3.27}$$

$$\dot{Q}_{diff} = \sum_{surface} S \cdot \tau \cdot \dot{I}_{diff} \tag{3.28}$$

$$\dot{Q}_{ref} = \sum_{surface} S \cdot \tau \cdot \dot{I}_{ref} \tag{3.29}$$

in which S is the incidence surface, τ is the surface area transmissibility and $\dot{I}(\cdot)$ is based on the mathematical equations as the following:

$$\dot{I}_{dir} = A \cdot exp(-B \sec \theta_z) \tag{3.30}$$

$$\dot{I}_{diff} = \frac{1}{2} \cdot C \cdot \dot{I}_{dir} \cdot (1 + \cos\beta) \tag{3.31}$$

$$\dot{I}_{ref} = \frac{1}{2} \cdot \rho_g \cdot (\dot{I}_{dir} + \dot{I}_{diff}) \cdot (1 - \cos\beta) \tag{3.32}$$

The parameters and description are listed in Table 3.7. A, B and C are constants tabulated in ASHRAE Handbook of Fundamentals [4]. Both Zenith angle and angle of incidence beam are dependent on location and time. The related information can be found in National Solar Radiation Database (NSRDB) from National Renewable Energy Laboratory. NSRDB is a serially complete collection of meteorological and solar irradiance data sets for the United States and a growing list of international locations.The data base contains hourly data of the solar position (Fig. 3.12). The value of ground reflectivity ρ_g is approximately 0.2 based on [4].

Table 3.7: Parameters in Solar Radiation Calculation

Parameter	**Description**
A	Apparent solar irradiation
B	Extinction coefficient
C	Diffuse radiation factor
θ_z	Zenith angle as shown in Fig. 3.11
θ_i	The angle of incidence beam
β	The surface angle with horizontal
ρ_g	Ground reflectivity

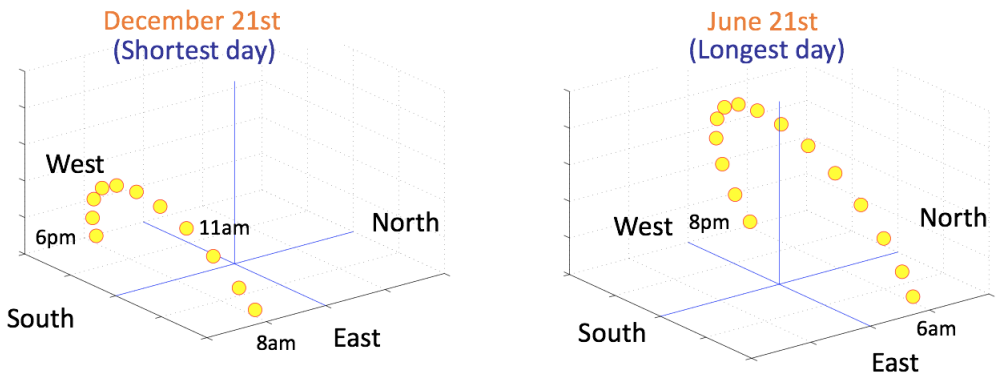

Figure 3.12: Apparent Daily Path of the Sun

3.3.2 Generic Cabin Geometry

The ambient conditions influence the cabin temperature through convection and conduction through the vehicle roof, glass surfaces, bottom surface, and doors. The information about the vehicle geometry and characteristics are necessary to calculate the solar radiation load. The geometry associated with a simple vehicle is used, which is shown in Fig. 3.13. Table 3.8 gives the actual values of the associated surface areas, and surface angles in relation to vertical axis. In addition, the following modeling assumptions are made:

- The vehicle is parked with the windshield facing south.
- The glass transmissibility is approximately 0.8 [4].
- The vehicle body transmissibility is approximately zero.

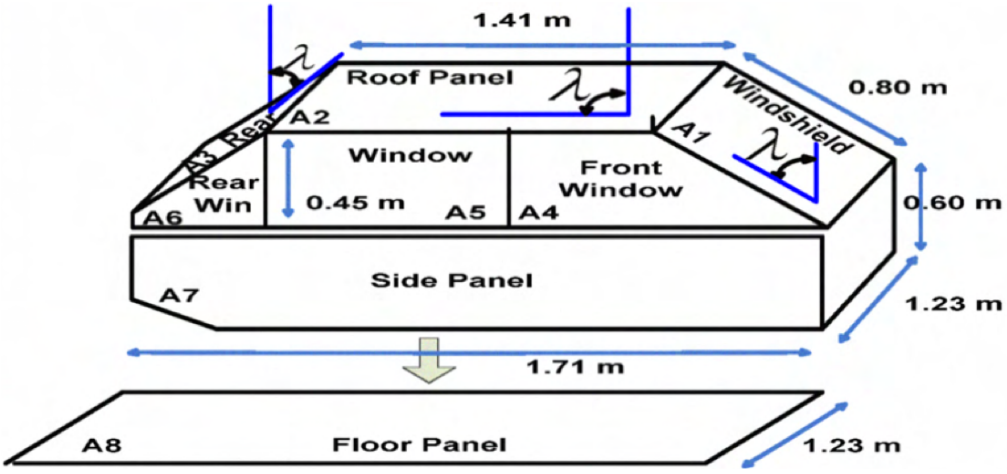

Figure 3.13: A Generic Vehicle Surface Geometry [70]

Table 3.8: Surface Area and Angles

Surface No	**Surface**	**Area** m^2	**Angle** λ°
A1	Windshield	0.98	40
A2	Roof panel	1.40	90
A3	Rear window	0.71	60
A4	Front window	$0.23 \cdot 2$	15
A5	Side window	$0.21 \cdot 2$	15
A6	Rear side window	$0.05 \cdot 2$	15
A7	Side panel	$0.99 \cdot 2$	0
A8	Floor	2.10	90

3.3.3 Vehicle cabin temperature simulation

With the generic cabin thermal model described above and the available environment information from NSRDB, a simulation platform is developed in Simulink®. The inputs to the model include:

- Hourly ambient temperature
- Hourly direct and diffuse solar radiation
- Hourly solar position
- Battery charging current

The output from the model is the vehicle cabin temperature as well as battery temperature. As an example, a hot day in Phoenix Arizona is simulated. The environment conditions are shown in Fig. 3.14. In this case, we assume no battery charging event, thus the vehicle cabin temperature has the profile in Fig. 3.15. It is clear that the vehicle cabin temperature can be much higher than the ambient temperature, which is critical when considering battery aging condition during charging.

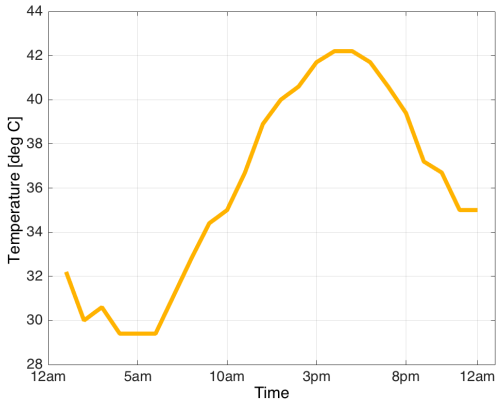

(a) Ambient temperature

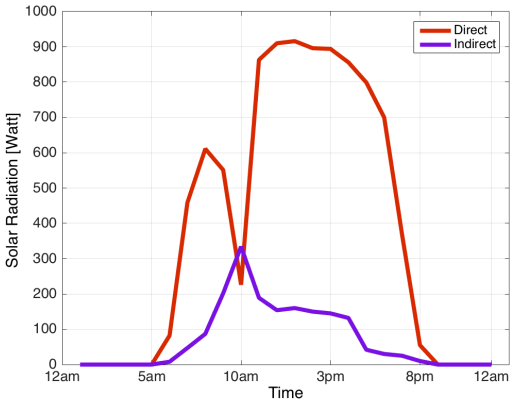

(b) Solar radiance

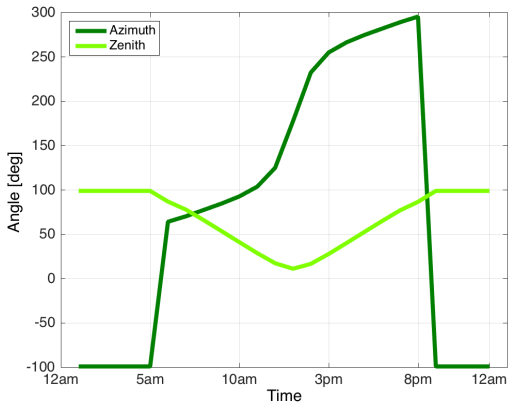

(c) Solar angle

Figure 3.14: Environment Conditions in Phoenix Arizona

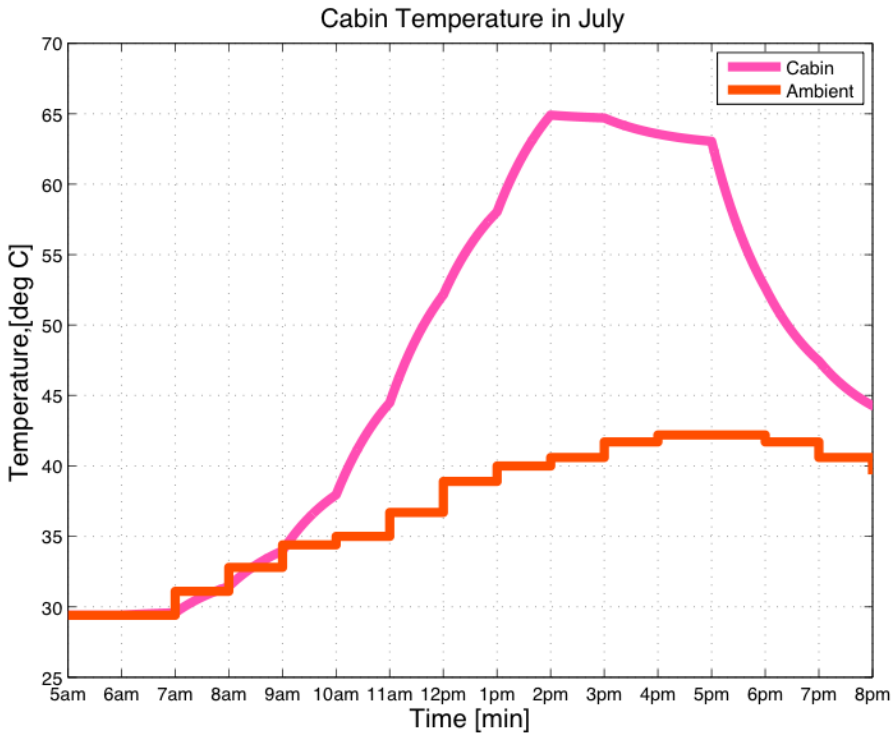

Figure 3.15: Vehicle Cabin Temperature

3.4 Vehicle Model Integration

In order to simulate the vehicle performance and estimate fuel consumption, it is necessary to have an integrated and system-level vehicle model, which includes all the powertrain components described previously. A forward, quasi-static approach [123] is used in developing the vehicle simulation platform in Simulink®. The simulator has four main functional blocks: driver, vehicle controller, powertrain and vehicle dynamics.The overall simulator structure is shown in 3.17.

When simulating vehicle performance, the driver will operate the vehicle to follow a given cycle, and the driver is modeled and implemented as a PI controller. The desired speed (input from driving cycle) is compared to the actual vehicle speed, and acceleration or barking commands are generated accordingly to follow the cycle speed profile. The pedal signal is a number between 0 and 1, which spans the powertrain torque output as well as the braking torque. A sample driving demonstrating the pedal signal along with vehicle speed profile is shown in Fig. 3.16. The driver's command is an input to the supervisory controller block, which is responsible of issuing the actuator setpoints (engine, electric machine, CVT and friction braking) to the rest of the powertrain components, which provide the total traction force. Finally, the force is applied to the vehicle speed dynamics (3.1), which yields the acceleration at the wheel with the road load information.

The supervisory controller is the focus of this study, in which optimal torque split between IC engine and electric machine and optimal CVT ratio are determined. The structure of the controller is illustrated in Figure 3.18. There are four control modules

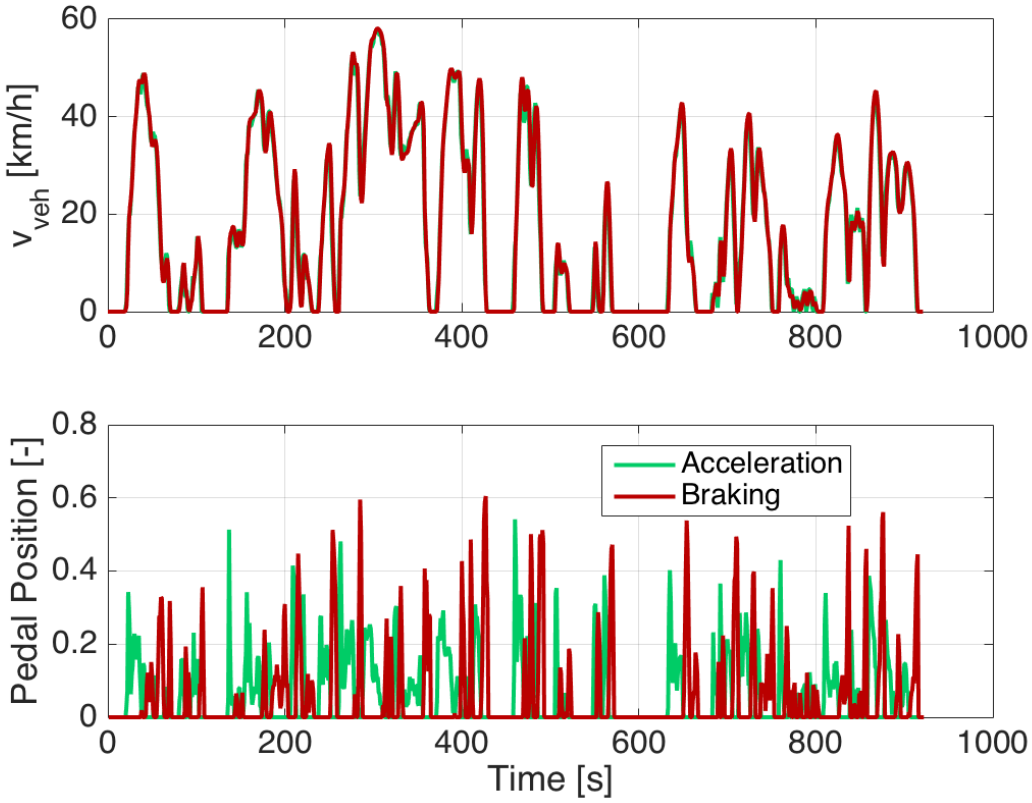

Figure 3.16: Vehicle Pedal Signal and Speed Profile

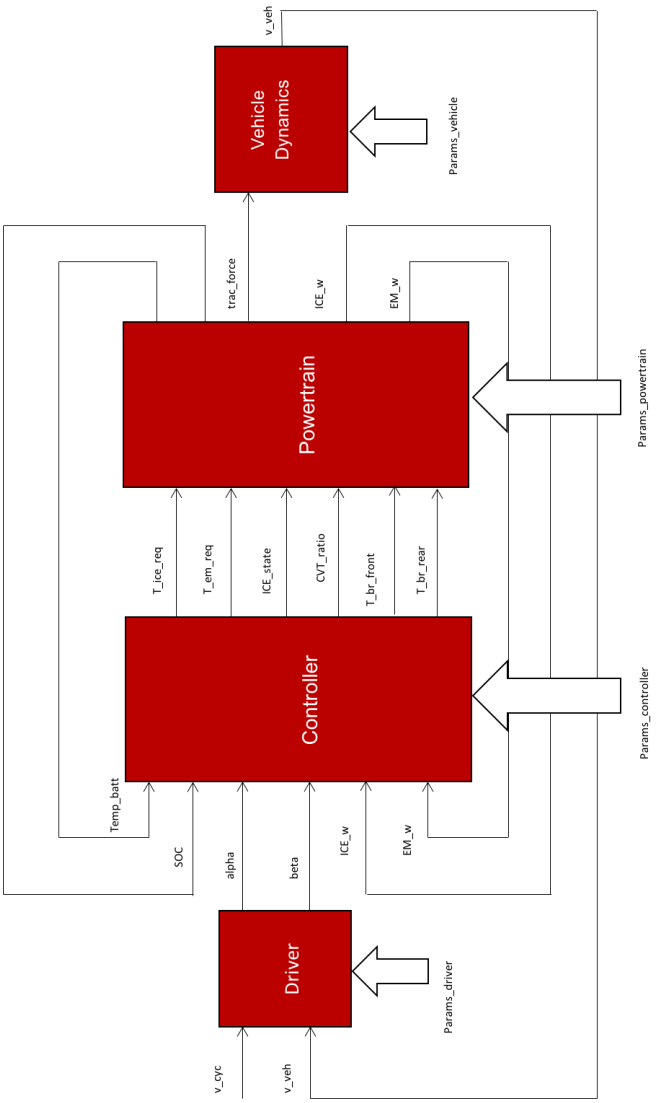

Figure 3.17: Vehicle Simulator Schematic

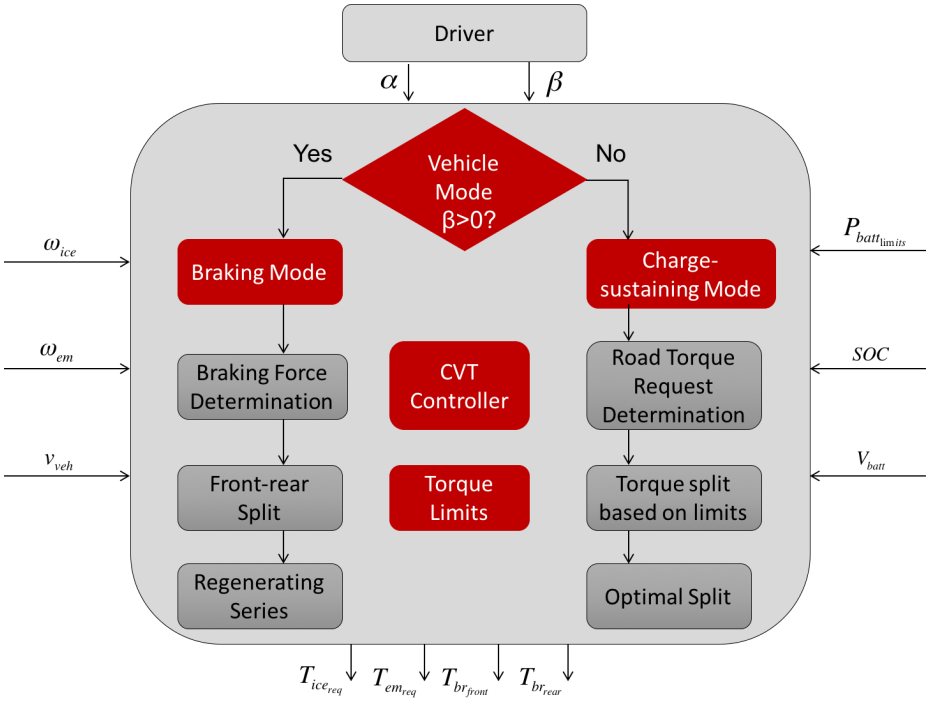

Figure 3.18: Vehicle Supervisory Controller

inside supervisory controler: charge-sustaining mode control, braking mode control, CVT control and torque limits control. The operation of the vehicle is divided into charge-sustaining mode and braking mode based on the pedal position. In charge-sustaining mode, the acceleration pedal position is translated into driver's torque request based on the current powertrain torque limits. Then optimal torque split is determined by solving the optimal control problem, which is presented in later chapters. In braking mode, the braking pedal position is interpreted based on the map shown in Figure 3.19. The total braking torque is splited between the front and rear axles based on the geometry of the vehicle using equations:

$$T_{front} = T_{brk} \cdot (\frac{b}{l} + \frac{h}{l} \cdot \frac{T_{brk}}{M_{veh} \cdot g}) \tag{3.33}$$

$$T_{rear} = T_{brk} \cdot (\frac{a}{l} - \frac{h}{l} \cdot \frac{T_{brk}}{M_{veh} \cdot g}) \tag{3.34}$$

where all the parameters and values are listed in Table 3.9. Since the vehicle being modeled is front-wheel-driving, only the braking torque on the front axle T_{front} is subjected to regenerative braking control.

To demonstrate the output from the simulator, some variables of interest are shown in Figure 3.20 and Figure 3.21.

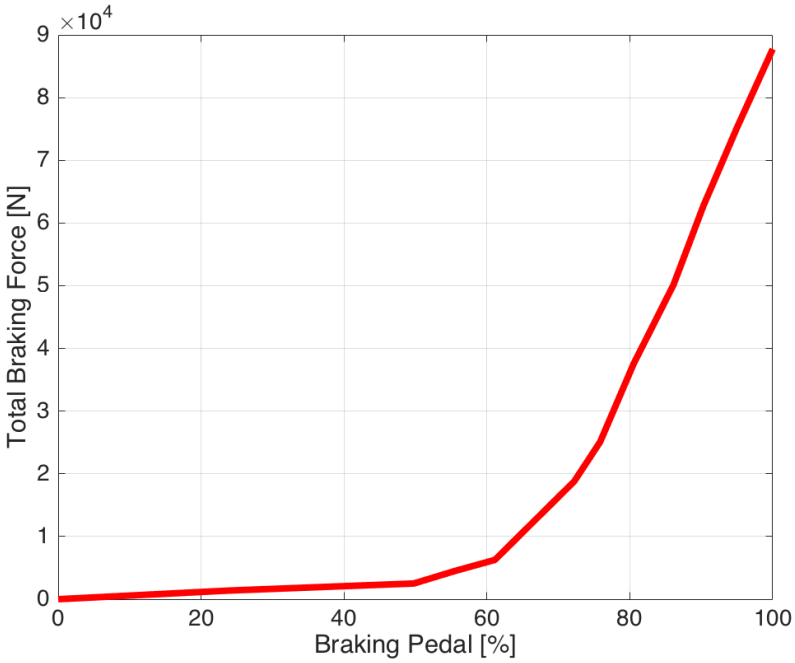

Figure 3.19: Braking Force & Braking Pedal Position

Table 3.9: Braking Torque Split Parameters

Parameter	Description	Value	Unit
M_{veh}	Mass of vehicle	1294	kg
g	Gravitational acceleration	9.81	m/s^2
l	Length of vehicle	4.5	m
a	Distance of front axle from center of mass	1.04	m
b	Distance of rear axle from center of mass	1.62	m
h	Height of center of mass above ground	0.58	m

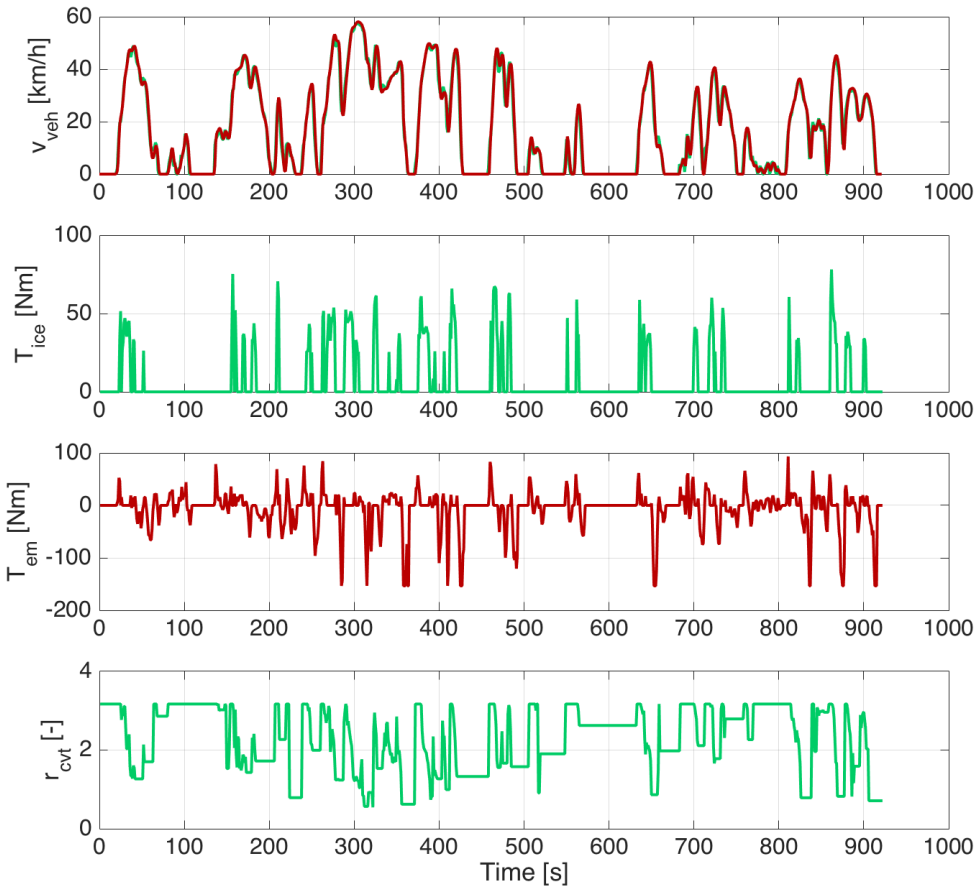

Figure 3.20: Variables Related to Powertrain Operation

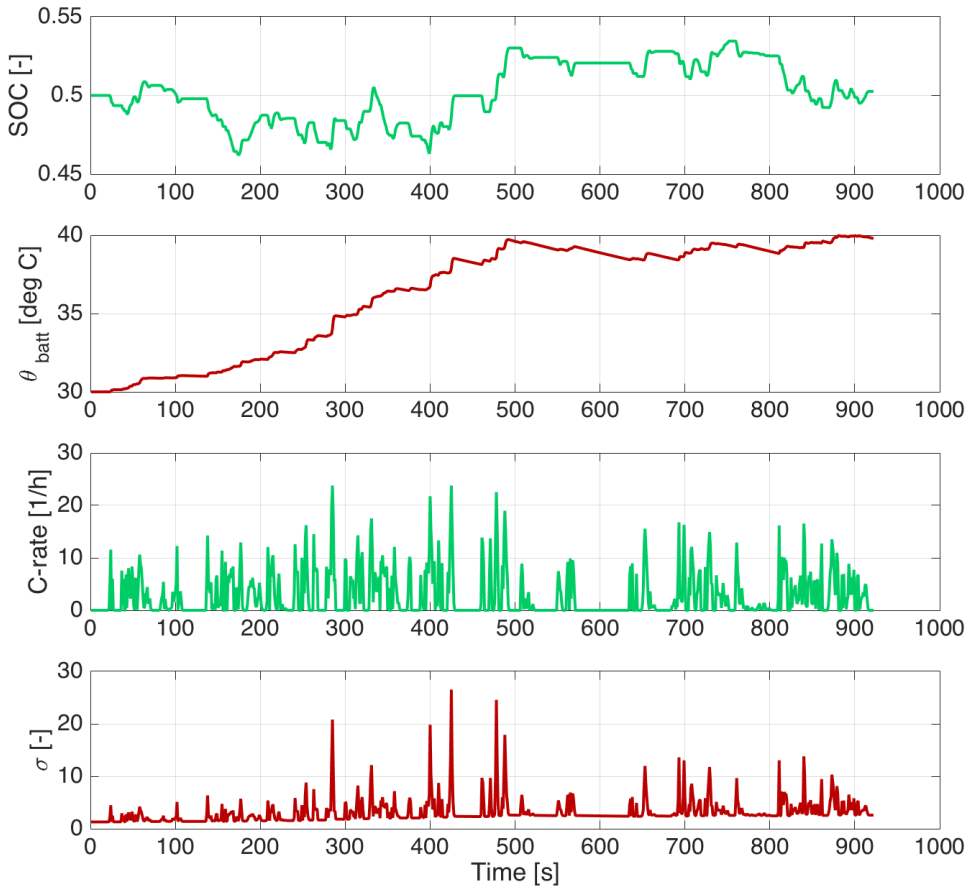

Figure 3.21: Variables Related to Battery Operation

3.5 Summary

A hybrid vehicle simulation system can be realized at varying level of fidelity depending on the requirements and objectives, but the basic system consists of models of the engine, motor/generator, transmission, final drive, wheel/tire, vehicle, and driver. The driver model outputs the vehicle demand power to the energy management based on the difference between the desired vehicle speed and actual vehicle speed. The energy management determines the required power from the engine and electric machine, respectively. The powertrain models respond to the power commands and the energy storage system provides the battery's SOC and terminal voltage. The vehicle performance, such as fuel economy, drivability, battery aging and emissions, is highly dependent on the energy management strategies, which are studied in the following chapters.

Chapter 4: Optimal Control Problems for Hybrid and Electric Vehicles with Consideration of Battery Aging

In this chapter, the energy management problem in hybrid electric vehicles is formulated as an optimal control problem in which the control algorithm is required to tradeoff between two objectives: minimizing fuel consumption, and minimizing battery degradation. To find a solution to this problem, a control-oriented and experimentally validated battery capacity degradation model is linked to the design of energy management strategy; the model is parametrized using experimental data that corresponds to the real HEV driving conditions. The energy management strategy focuses on charge-sustaining operating mode, which could apply equally well for HEV and plug-in HEV in charge-sustaining phase.

Two solutions of the optimal control problem are obtained and comparisons between the two solutions are conducted. In one case, the transmission shift ratio is pre-computed in advance of the optimal solution, while the transmission shift ratio is optimized as part of the optimal energy management strategy. Simulation-based results are presented and analysed to evaluate the benefits of different strategies. Important insights into the interdependency of battery aging and vehicle operation are

discussed to explore tradeoffs between fuel economy and battery capacity loss.

The optimal control problem formulation is presented first and followed by the analysis of the solutions obtained from four driving schedules, which helps draw conclusions about the nature of the optimal solutions; there results will be useful in a later chapter when a real-time implementable strategy is designed. In the second half of the chapter, we turn to another optimal control problem that minimizes battery capacity degradation in PHEVs while charging and compare the optimal charging strategy with the existing charging scenarios. Thus this chapter presents a complete set of optimal control problems related to xEVs with consideration of battery aging.

4.1 Design of objective function

The objectives of the optimal control problem formulated and solved are twofold: minimizing fuel consumption, while minimizing battery capacity degradation. A crucial step in formulating such optimal control problem consists in the development of a model to properly quantify the battery wear to be included in the cost function. In this work, an Ampere-hour throughput-based capacity degradation model is adopted, which is described in section 3.2.3. The assumption behind the throughput model is that a battery is able to withstand a certain amount of energy throughput subjected to a constant operating condition before it reaches the end of life. This is equivalent to have the battery last a number of charging and discharging cycles. It is clear that operating conditions dictate battery aging phenomena, thus different battery life durations are expected when the battery is operated under different inputs and environmental conditions. The concept of severity factor is utilized to quantify the

relative aging effect with respect to a nominal operating condition. If the-end-of-life of a battery is defined as a certain percentage capacity drop from its initial value, then battery life with respect to a nominal cycle can be characterized by the total Ah-throughput when the battery reach the-end-of-life [132] [104]. The nominal battery life Γ in terms of Ah-throughput can be expressed as

$$\Gamma = \int_0^{EOL} |I_{nom}(t)|dt \tag{4.1}$$

where I_{nom} is the current profile under nominal conditions.

When conditions are different than the nominal scenario, the amount of Ah can be delivered before the end-of-life will be different, which can be represented by

$$\gamma = \int_0^{EOL} |I(t)|dt \tag{4.2}$$

where $\gamma(I, \theta_{batt}, SOC)$ is the battery life given in terms of Ah-throughput corresponding to specific operating conditions given in terms of current I, temperature θ and SOC [132] [104]. The relative aging effects of any load cycles the battery is subject to can be reflected by severity factor defined as:

$$\sigma(I, \theta_{batt}, SOC) = \frac{\Gamma}{\gamma(I, \theta_{batt}, SOC)} = \frac{\int_0^{EOL} |I_{nom}(t)|dt}{\int_0^{EOL} |I(t)|dt} \tag{4.3}$$

When the battery is undergoing a more severe load cycle, the severity factor is greater than one and a shorter life is expected. The concept of severity factor to express the relative aging effect of a specific load cycle was initially proposed in [132][88].

The severity factor σ can be obtained empirically using the aging model in (3.24). If, for example, the end-of-life is defined as 20% loss of capacity and the nominal conditions defined in this study are $I_{c,nom}$ equals to 1C, $SOC_{nom} = 0.5$ and $\theta_{nom} = 25\,^{\circ}\text{C}$, then the nominal battery life Γ can be calculated as

$$\Gamma = \left[\frac{20}{(\alpha \cdot SOC_{nom} + \beta) \cdot exp(\frac{-31700+163.3 \cdot I_{c,nom}}{R \cdot \theta_{nom}})} \right]^{\frac{1}{0.57}} \tag{4.4}$$

Battery life under different load conditions could be computed as follow if we knew the actual values of SOC, I_c and θ_{batt}

$$\gamma = \left[\frac{20}{(\alpha \cdot SOC + \beta) \cdot exp(\frac{-31700+163.3 \cdot I_c}{R \cdot \theta_{batt}})} \right]^{\frac{1}{0.57}} \tag{4.5}$$

If we then compute $\gamma(SOC, I_c, \theta_{batt})$ for various values of each variable, we could derive the value of the severity factor defined in (4.3). The shape of the severity factor is shown in Figure 4.1 with two different battery temperature values.

In order to give the effective life depletion due to charge exchange within the battery, we define effective Ah-throughput as in [104]:

$$Ah_{eff}(t) = \int_0^t \sigma(I_c, \theta_{batt}, SOC) \cdot |I(\tau)| d\tau \tag{4.6}$$

Efective Ah-throughput gives the effective life depletion with respect to the nominal life defined by Γ. Thus the battery will reach the end of life when $Ah_{eff}(t) = \Gamma$, and the objective of minimizing battery aging is equivalent to minimizing $Ah_{eff}(t)$ [133].

Considering fuel economy and battery aging simultaneously requires defining a suitable cost function. We propose a cost function which has the form of

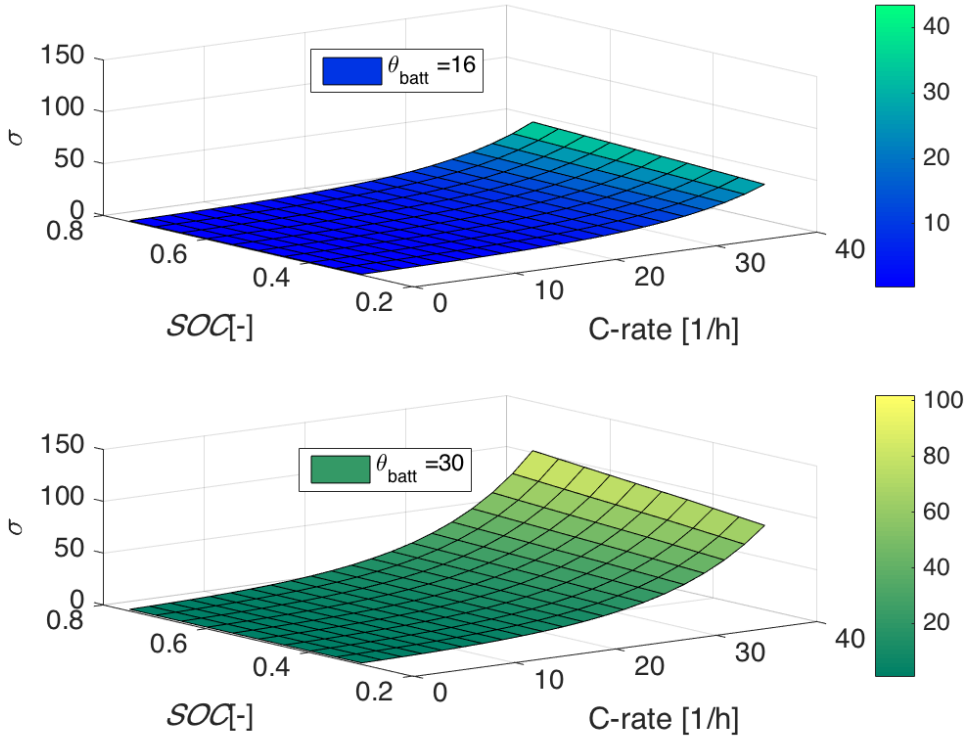

Figure 4.1: Severity Factor Map

$$J = \int_0^{t_f} \alpha \cdot \frac{\dot{m}_f(t) - \bar{\dot{m}}_f}{m_{f,diff}} + (1-\alpha) \cdot \frac{\sigma(t) \cdot |I_{cell}(t)|}{Ah_{eff,diff}} dt \tag{4.7}$$

The first term represents fuel cost while the second term can be interpreted as battery aging cost. The parameter α is a weighting factor which can take on any value between 0 and 1. One can continuously trade off between these two costs by varying the value of α, which should yield a Pareto front [92]. In order to make these two terms numerically comparable, normalization is performed for both. The idea is that the two terms are normalize by the differences of optimal function values in the Nadir and Utopia points that give the length of the intervals where the optimal objective functions vary within the Pareto optimal set [52]. As a result, $\bar{\dot{m}}_f$ is the average fuel flow rate in g/s corresponding to the best fuel economy case, which is when $\alpha = 1$, and which is the worst case in terms of battery aging. Theoretically, in the minimum aging case, i.e. $\alpha = 0$, the vehicle operates as a conventional vehicle without using the battery, which should yield zero aging effects and worst fuel economy. Then $m_{f,diff}$ represents the difference in fuel consumption between the best and worst case while $Ah_{eff,diff}$ is the difference in aging cost. This normalization scheme provides the best normalization results as one normalizes the objective functions by the true intervals of their variation over the Pareto optimal set. Intuitively, it is not difficult to see that the two terms after normalization will be bounded by 0 and 1, will have the comparable magnitude in the weighted objective function.

4.2 States and constraints

There are many state variables in a hybrid powertrain. The dimension of the state vector is dictated by the objective or the required level of accuracy [85, 57]. The system is often treated as quasi-stationary, if fuel consumption is the main concern. State variables, which represent the dynamic behavior of the electric motor and the ICE, have much faster dynamics than that of the main energy flows in an HEV and, therefore, are not considered in this situation. In the traditional fuel-minimization-focused problems, it is acceptable that battery SOC is considered as the only state variable. However, in this work, reducing battery aging effect is another target in addition to fuel minimization. Therefore, battery temperature, which is an essential factor related to battery aging, is included as the second state variable in this optimal control problem. The state dynamics is described in 3.18 and 3.22 respectively.

The state constraints emphasise the fact that the state of charge should remain within an acceptable range during the trip:

$$SOC_{min} \leqslant SOC(t) \leqslant SOC_{max} \quad \forall t \in [0, t_f] \tag{4.8}$$

The maximum and minimum value of the state of charge are constant during the driving and are set to $SOC_{min} = 0.3$ and $SOC_{max} = 0.7$. The terminal constraints states that the initial and final state of charge should be close (ideally equal) in a charge-sustaining vehicle.

$$SOC(0) = SOC(t_f) = SOC_0 \tag{4.9}$$

The value of SOC_0 is set to 0.5.

Regarding the battery temperature θ_{batt}, there is no constraint applied in terms of minimum and maximum allowable temperature. The battery pack is air-cooled with a fixed coolant temperature that is dependent on the ambient conditions. Thus the battery temperature evolves based on 3.22 with initial condition $\theta_{batt}(0) = \theta_{batt,0}$.

4.3 Control and constraints

The system analysed in this work is a parallel pre-transmission hybrid, and the vehicle architecture is shown in Fig.3.1. The engine and electric machine are mounted on the same shaft which connects to the continuously variable transmission (CVT) through a torque damper. A CVT provides an infinite number of transmission gear ratios within the limits of the device. This is in contrast to a stepped automatic or manual transmission. Thus, in addition to torque split, the CVT ratio adds one more degree of freedom to the system, which makes engine speed or the main shaft speed independent of wheel speed. Thus the available free inputs are electric machine torque T_{em}, and CVT ratios r_{cvt}.

The constraints on the control inputs first come from the physical limits that should be always respected:

$$T_{em_{min}}(\omega_{em}(t)) \leqslant T_{em}(t) \leqslant T_{em_{max}}(\omega_{em}(t)) \tag{4.10}$$

$$r_{cvt_{min}} \leqslant r_{cvt}(t) \leqslant r_{cvt_{max}} \tag{4.11}$$

In addition, the driver's demand should always be satisfied, which includes road torque request and vehicle speed profile:

$$T_{road}(t) = (T_{ice}(t) + T_{em}(t)) \cdot \eta_{cvt}^{k} \cdot r_{cvt}(t) \cdot r_{diff} + T_{brake}(t) \tag{4.12}$$

$$\omega_{ice}(t) = \omega_{em}(t) = \omega_{wh}(t) \cdot r_{cvt}(t) \cdot r_{diff} \tag{4.13}$$

As CVT ratio connects the engine speed and electric machine speed to wheel speed, it should guarantee that both engine speed and electric machine speed stay in their limits while meeting the wheel speed profile.

4.4 Sequential optimization strategy

For the strategy studied in this section, the CVT ratio is not considered as part of the optimal control problem and instead it is optimally determined before torque split by way of a static optimization. Therefore, this strategy is called sequential optimization strategy.

4.4.1 Problem formulation

In a hybrid architecture with a fixed number of step transmission, the engine crankshaft speed is known once the wheel speed profile is known, thus only the torque split between engine and electric machine needs to be optimized. In this type of problems, optimization for minimizing fuel consumption and optimization for maximizing engine efficiency are not equivalent, because for a given engine speed the torque that yields minimum fuel consumption is not necessarily the torque that gives the best

efficiency, which can be understood by comparing the engine fuel consumption map with the engine efficiency map in Figure 4.2. However, when both engine torque and engine speed are controllable, as in this hybrid architecture with a CVT, minimization of fuel consumption and maximization of engine efficiency are equivalent due to the fact that for a given power, the engine operating point (T_{ice}, ω_{ice}) that yields the minimum fuel consumption has to be the point that gives the best efficiency.

In the sequential optimization strategy, the continuously variable transmission is controlled to keep the internal combustion engine operating at low fuel consumption points by tracking the optimal operation line (OOL) [21], which is shown in Figure 4.3. The OOL can be calculated from the engine map by minimizing the fuel consumption or maximizing the efficiency for a set of power outputs. As indicated by the Figure. 4.3 (a), the best efficiency of the engine is around 35%, which is located at a relatively high speed region. The selected engine has an uncommon efficiency map, which manifests in the following way: the isoefficiency line of 30% dips down around $\omega_{ice} = 4300$, which makes the OOL goes down at that region and in addition, this engine has high efficiency at very high speed (4.3 (a)). The engine maps (fuel consumption and efficiency) are acquired from the Powertrain System Analysis Toolkit (PSAT) developed by Argonne National Laboratory. The engine is particularly selected to demonstrate the engine behavior with the optimal control strategies, however, the methodology introduced in this work is not restricted to a particular vehicle model.

Based on the OOL, the optimal engine speed for a given power requirement and vehicle speed can be decided. The OOL tracking strategy is implemented as a 2-D look-up table, which is illustrated in Figure. 4.4. Thus instead of being considered

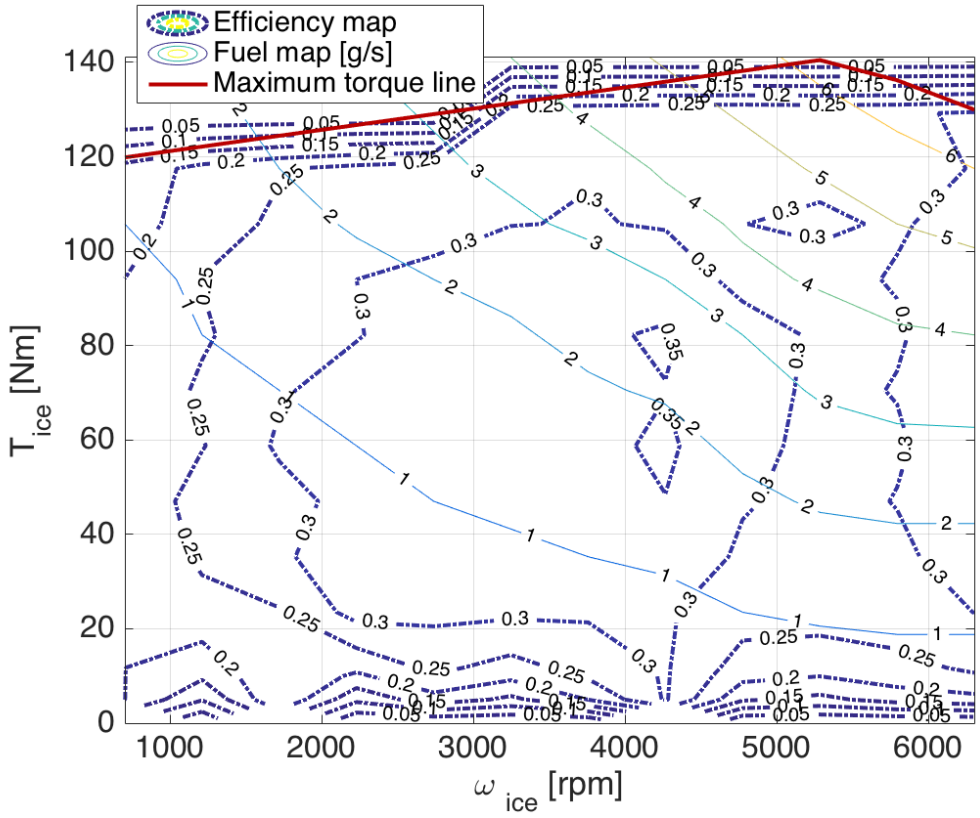

Figure 4.2: Engine Fuel Map And Efficiency Map

as a decision variable in the optimal control problem, CVT ratio is formulated as a disturbance. Since the CVT ratio is determined before the torque split, the engine will operate around the OOL instead of being exactly on the OOL.

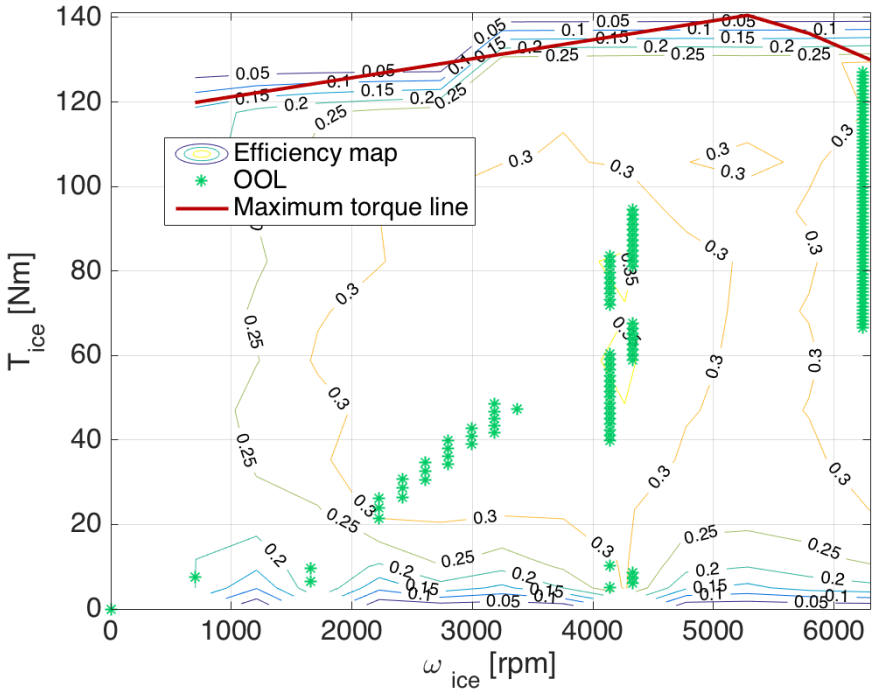

(a)

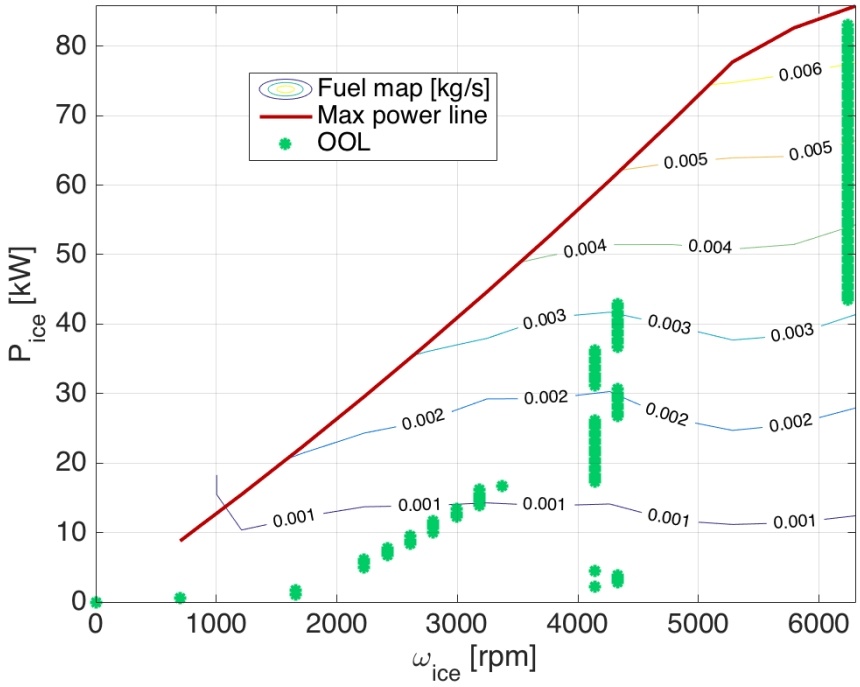

(b)

Figure 4.3: Engine Optimal Operation Line

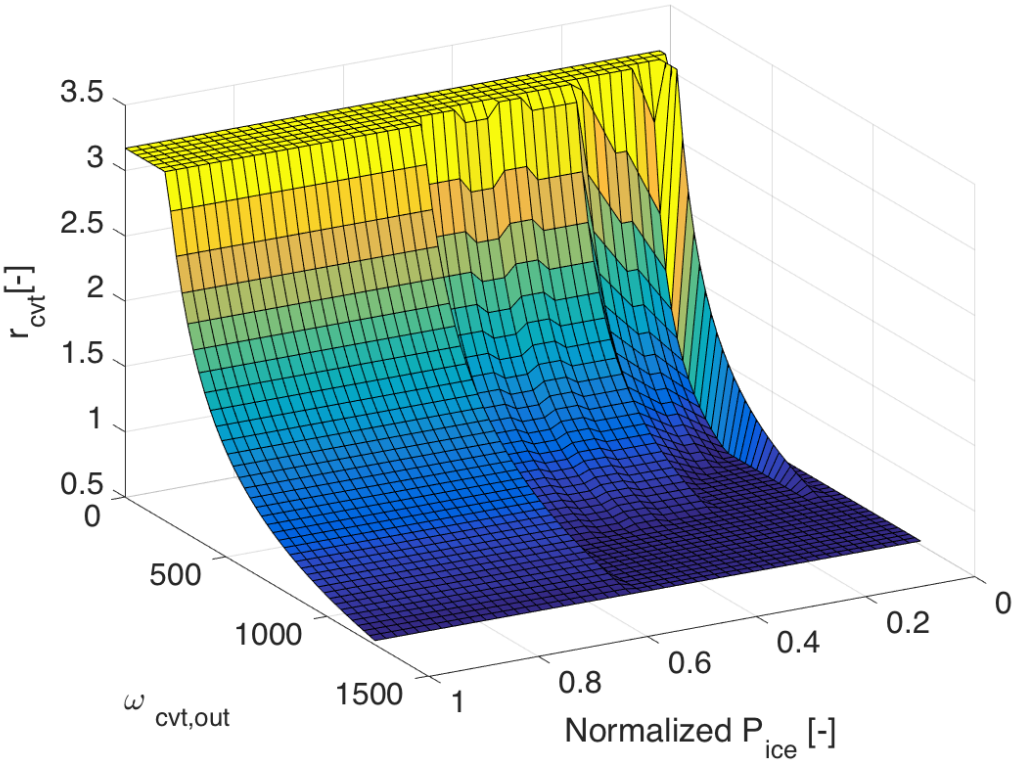

Figure 4.4: Map of CVT Ratio as A Function of Engine Power and Output Speed

Based on the previous assumptions and models, the complete optimal control problem statement is the following:

$$\min : \int_0^{t_f} \alpha \cdot \frac{\dot{m}_f(t) - \bar{\dot{m}}_f}{m_{f,diff}} + (1-\alpha) \cdot \frac{\sigma(t) \cdot |I_{cell}(t)|}{Ah_{eff,diff}} dt$$

subject to

$$\begin{aligned}
&S\dot{O}C(t) = -\frac{I_{cell}(t)}{Q_{cell} \cdot 3600} \\
&\dot{\theta}_{batt}(t) = \frac{\dot{q}_{batt}(t) + h_{batt} \cdot A_{surface} \cdot (\theta_{cool} - \theta_{batt}(t))}{M_{batt} \cdot C_{p_{batt}}} \\
&T_{road}(t) = (T_{ice}(t) + T_{em}(t)) \cdot \eta_{cvt}^{k} \cdot \gamma_{cvt}(t) \cdot \gamma_{diff} + T_{brake}(t) \\
&0 \leqslant T_{ice}(t) \leqslant T_{ice_{max}}(\omega_{ice}(t)) \\
&T_{em_{min}}(\omega_{em}(t)) \leqslant T_{em}(t) \leqslant T_{em_{max}}(\omega_{em}(t)) \\
&T_{brake}(t) \leqslant 0 \\
&I_{cell_{min}} \leqslant I_{cell}(t) \leqslant I_{cell_{max}} \\
&SOC_{min} \leqslant SOC(t) \leqslant SOC_{max} \\
&SOC(0) = SOC_0 \\
&SOC(t_f) = SOC_0 \\
&\theta_{batt}(0) = \theta_{batt,0}
\end{aligned} \tag{4.14}$$

Thus the optimal control problem can be reduced to the mathematical form:

$$u^* = \underset{u}{\text{argmin}} : J = \int_0^{t_f} \alpha \cdot \frac{\dot{m}_f(u,t) - \bar{\dot{m}}_f}{m_{f,diff}} + (1-\alpha) \cdot \frac{\sigma(x,u,t) \cdot |I_{cell}(x,u,t)|}{Ah_{eff,diff}} dt$$

subject to

$$\begin{aligned} \dot{x} &= f(x,u,v) \\ x(0) &= x_0 \\ x(t_f) &= x_T \\ x(t) &\in \chi \\ u(t) &\in \mathcal{U} \end{aligned} \tag{4.15}$$

where

$$x = \begin{bmatrix} SOC \\ \theta_{batt} \end{bmatrix} \quad u = T_{em} \quad v = \begin{bmatrix} T_{road} \\ \omega_{wh} \\ r_{cvt} \end{bmatrix}$$

where x is the state vector, u is the control input, v is the measured disturbance. χ and $\mathcal{U}$ are defined as the admissible state and control sets respectively. As this control strategy is designed for charge sustaining operation mode, SOC at the end of one trip is required to equal to that at the beginning, which is formulated as a hard constraint.

4.4.2 DP solution

As an approach that guarantees global optimality, Dynamic Programming is applied to solve the optimal control problem. Applying dynamic programming to the system (4.15) corresponds to finding the optimal sequence of the appropriate decision variable backward in time with the knowledge of future driving conditions. The problem setup for dynamic programming requires a discrete-time description of the

system, and a discrete set of values for the decision variables. The procedure is illustrated next.

Consider the discrete-time system described by a discretized version of (3.18) and (3.22):

$$SOC(k+1) = SOC(k) - \Delta t \cdot \frac{I_{cell}(k)}{Q_{cell}}, \quad k = 0, \ldots, N_T - 1 \tag{4.16}$$

$$\begin{aligned}\theta_{batt}(k+1) =& \theta_{batt}(k) + \\ & \Delta t \cdot \frac{I_{cell}^2(k) \cdot R_0 \cdot N_s \cdot N_r + U \cdot A_{surface} \cdot (\theta_{cool} - \theta_{batt}(k))}{M_{batt} \cdot C_{p_{batt}}}, \quad k = 0, \ldots, N_T - 1\end{aligned} \tag{4.17}$$

where Δt the sampling time, N_T the length of the optimization horizon in number of samples, which is calculated as

$$N_T = \frac{t_f - 1}{\Delta t} + 1 \tag{4.18}$$

Thus, k indicates the value of the variable at the k$^{\text{th}}$ time step. The states of the system are discretized and can only take one of the finite number of values between the minimum and the maximum. The set of values can be defined as

$$SOC^j = SOC_{min} + (j-1)\frac{SOC_{max} - SOC_{min}}{N_{SOC} - 1}, \quad j = 1, \ldots, N_{SOC} \tag{4.19}$$

$$\theta_{batt}^j = \theta_{batt,min} + (j-1)\frac{\theta_{batt,max} - \theta_{batt,min}}{N_\theta - 1}, \quad j = 1, \ldots, N_\theta \tag{4.20}$$

where N_{SOC} and N_θ are the number of available grid point at each time step for SOC and θ_{batt} respectively. The control input, T_{em}, needs to be discretized between the admissible range as well.

$$T_{em}^i = T_{em,min} + (i-1)\frac{T_{em,max} - T_{em,min}}{N_u - 1}, \quad i = 1, \ldots, N_u \tag{4.21}$$

where N_u is the number of available control options at each time step. The control problem is to minimize the total cost:

$$\min_{u(k),k\in\{1,\ldots,N_T\}} \sum_{k=0}^{N_T} \alpha \cdot \frac{(\dot{m}_f(x(k),u(k)) - \bar{\dot{m}}_f)\cdot\Delta t}{m_{f,diff}} + (1-\alpha)\cdot\frac{\sigma(x(k),u(k))\cdot|I(x(k),u(k))|\cdot\Delta t}{Ah_{eff,diff}} \tag{4.22}$$

with respect to the predefined state grid and control grid. The Dynamic Programming algorithm determines the optimal sequence of state of charge, and then, as a consequence, the electric machine torque that produces it. In this work, a generic dynamic programming function for Matlab, which is called *dpm* function [140], is used to solve the Dynamic Programming problem.

4.4.3 Simulation results

In this work, four driving cycles are studied, which are US06, Federal Urban Driving Schedule (FUDS), Manhattan and Artemis urban driving schedule. They represent aggressive driving, urban and city driving conditions, which should be able to address the performance of the optimal controller in a general way. The ambient temperature is set to 30C, with the benefit of the optimal controller being more obvious under more aggressive driving conditions and at higher ambient temperatures, since these are the conditions that cause the battery to see larger C-rate and higher

cell temperatures.

US06 Driving Schedule

US06 driving schedule was developed to address aggressive, high speed and/or high acceleration driving behavior, rapid speed fluctuations, and driving behavior that is often typical of real world high driving. The cycle represents an 8.01 mile (12.8 km) route with an average speed of 48.4 miles/h (77.9 km/h), maximum speed 80.3 miles/h (129.2 km/h), and a duration of 596 seconds.

Performance results for the Pareto front of the controller that optimally tradeoffs battery capacity degradation with engine fuel consumption are presented in Figure 4.5 and the numerical results are summarized in Table 4.1 by sweeping the weighting factor α in (4.22) from 0.1 to 1. This plot indicates that, indeed, there exists a fundamental tradeoff between battery capacity degradation and fuel economy. Namely, effective Ah-throughput can be potentially reduced to zero, which makes the vehicle function as a conventional one, but at the sacrifice of a measurable decrease in fuel economy. However, it is possible to reduce the aging effect, or Ah_{eff}, by a big percentage with only small increase on fuel consumption. If one compares the results of $\alpha = 0.9$ with what from $\alpha = 1$, the effective Ah-throughput is reduced by 46.0% while the fuel consumption is increased by only around 1%, which is negligible.

To acquire physical insights into the behavior and properties of the optimal controllers, we analyze three solutions from the Pareto set, $\alpha = 1$, 0.7 and 0.3. The

Table 4.1: Dynamic Programming Solution for US06

α	Fuel Consumption [g]	Ah_{eff}
1	563	36.8
0.9	569	19.7
0.8	578	10.9
0.7	586	6.7
0.6	594	4.3
0.5	600	3.0
0.4	608	1.9
0.3	618	1.1
0.2	630	0.4
0.1	636	0.2

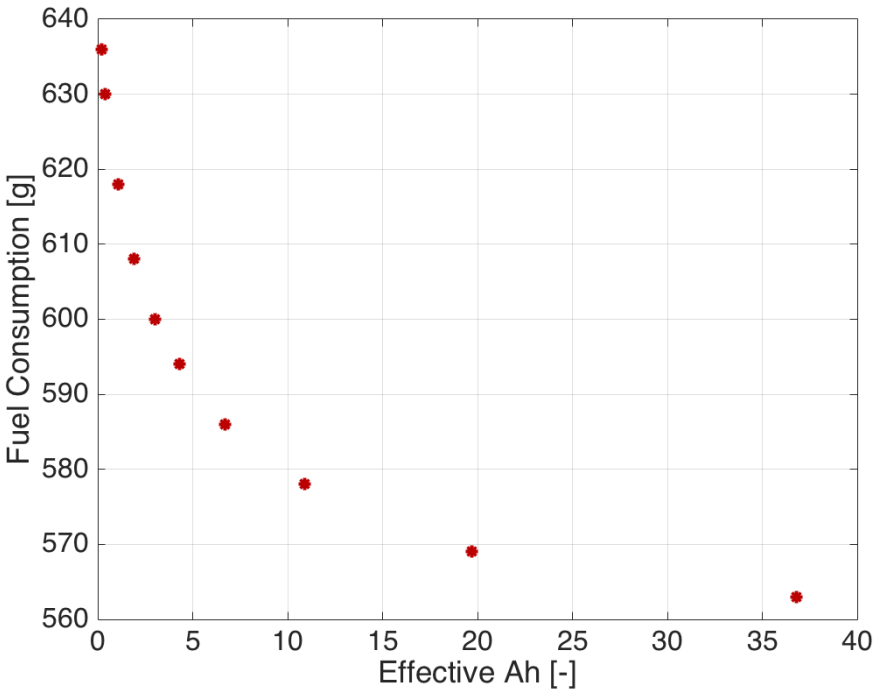

Figure 4.5: Dynamic programming solutions for US06 with different α values

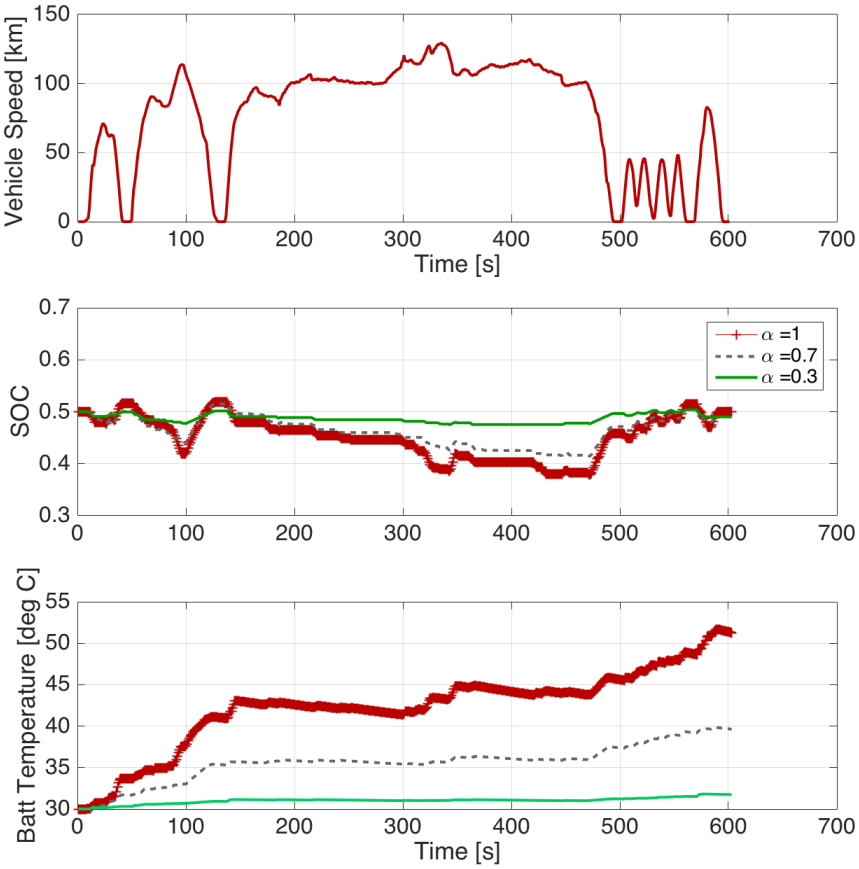

Figure 4.6: Dynamic programming solutions for US06 with different α values

selected solutions are supposed to represent fuel optimal case, balancing fuel consumption and aging cost case and aging-dominant scenario. Figure 4.6 demonstrates the profiles of battery SOC and battery temperature along with the vehicle speed. If we define ΔSOC as the difference between the maximum and minimum points during one trip, then

$$\Delta SOC = max(SOC(t)) - min(SOC(t)) \tag{4.23}$$

With $\alpha = 1$, the SOC profile is more dynamic and ΔSOC, is around 13.3%. As α decreases, the SOC trajectory becomes flatter and in addition, the value of ΔSOC becomes smaller: 10% and 2.9% for $\alpha = 0.7$ and $\alpha = 0.3$ respectively. Battery temperature, as one of the most influential factors on battery health degradation, gives a good demonstration on the effectiveness of the controller in optimally reducing aging effects by varying the weighting factor, which results in about 20 °C difference at the end of the trip. Generally speaking, the controller achieves lower aging effects by using less electric energy regardless of the energy flow direction and by choosing the best timing to use it.

This can be further illustrated by the power split profiles in Figure 4.7. There are many instances when electric machine provides power assist with $\alpha = 1$, which basically keeps the engine operating below 40kW. In the case with $\alpha = 0.7$, the electric power assist becomes smaller, while with $\alpha = 0.3$ there is almost no electric assistance. On the other hand, if we look at the negative power split, which is between regenerative power and friction braking power, the recovered energy becomes less and less as α becomes smaller and smaller. This is due to the fact that battery

ages whether it is being charged or discharged, and therefore energy from regenerative braking is not free in the context of reducing battery capacity degradation. It is more obvious in Figure 4.8, which shows electric machine power from the three cases on the same axes. If we zoom into the time range between 85s and 110s, it is clear that electric machine power decreases from both direction as α decreases. Moreover, this is a charge-sustaining HEV, the net charge flow at the end of the trip should be close to zero, which makes the discharged energy equal to the sum of the recovered energy and the energy from engine to battery. As a result, when discharged energy, which is only for electric assist, becomes less, the recovered energy will drop proportionally.

In fact, with US06 driving cycle, the engine seldom charges the battery regardless of the value of α. One of the reasons is that the driving cycle is too aggressive that it is not efficient for the engine to produce excessive power to charge the battery even with $\alpha = 1$. More importantly, using engine to charge battery is an event that will have both fuel cost and battery aging cost, which is not favored by either of the objectives. The result can be demonstrated by Figure 4.9, which shows the total battery energy throughput consist of three categories: discharged energy, recovered energy and energy from engine to battery. For the full range of α values considered, the amount of energy flowing from engine to battery is negligible. Another observation is that the total energy throughput decreases with α.

In addition to reducing the total energy usage from the battery, the controller also tries to bring down the severity factor to save battery life, which can be seen from Figure 4.10. There are some extremely hight values of severity factor with $\alpha = 1$,

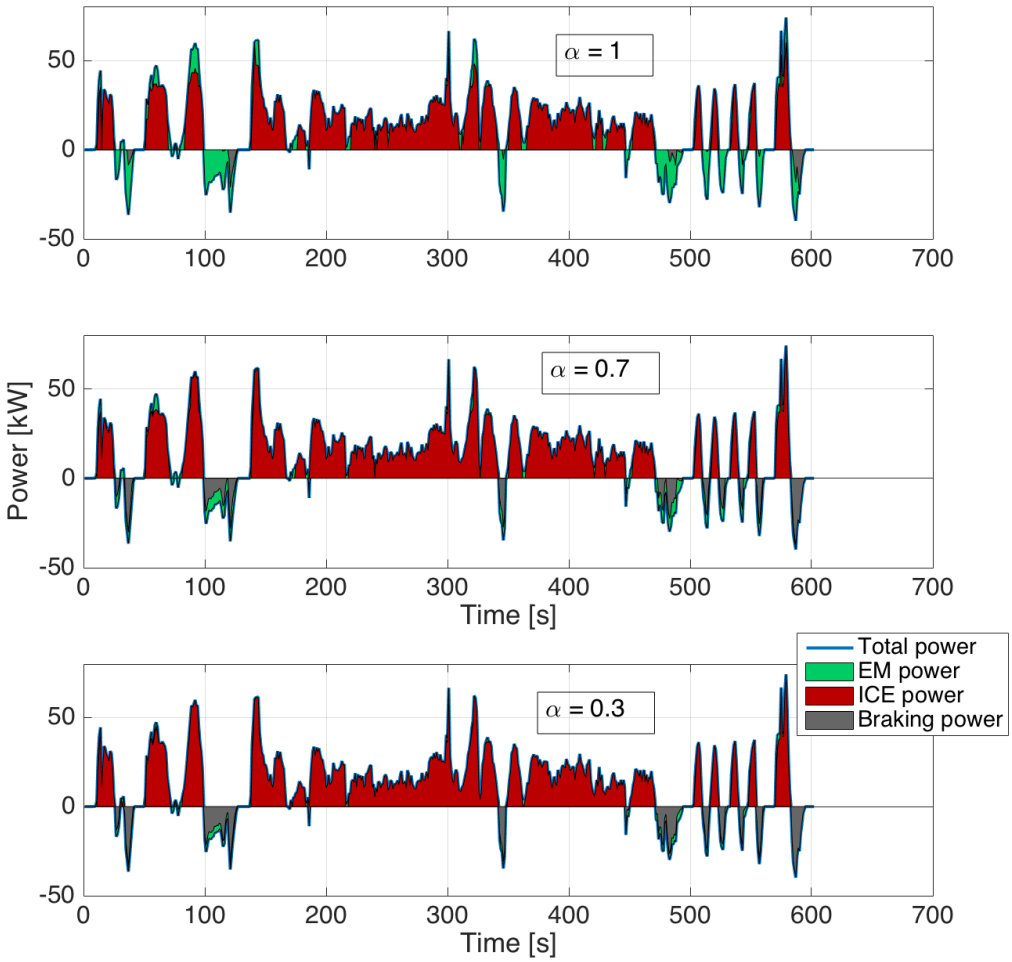

Figure 4.7: Power split for US06 with different α values

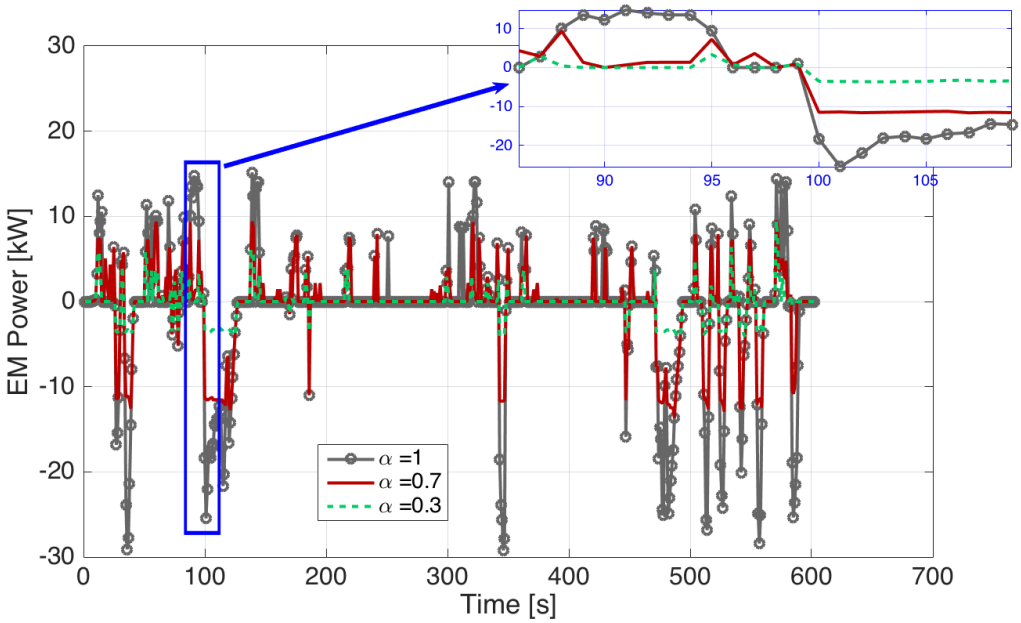

Figure 4.8: Electric machine power for US06 with different α values

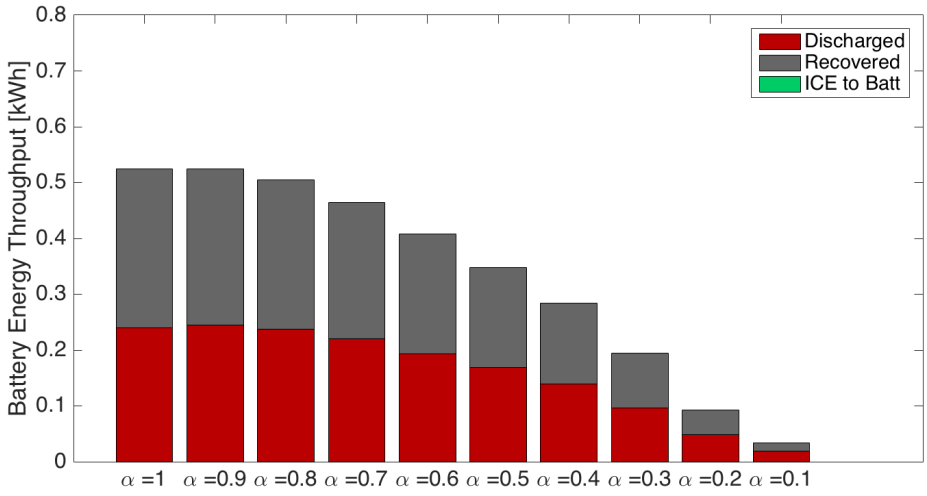

Figure 4.9: Battery energy throughput for US06 with different α values

however, with $\alpha = 0.7$, the optimal controller is able to avoid all the big spikes and keep the severity factor lower than 10 most of the time. Further reduction can be observed with $\alpha = 0.3$. Figure 4.11 gives the distribution of severity factor from different operating modes on the severity factor map.

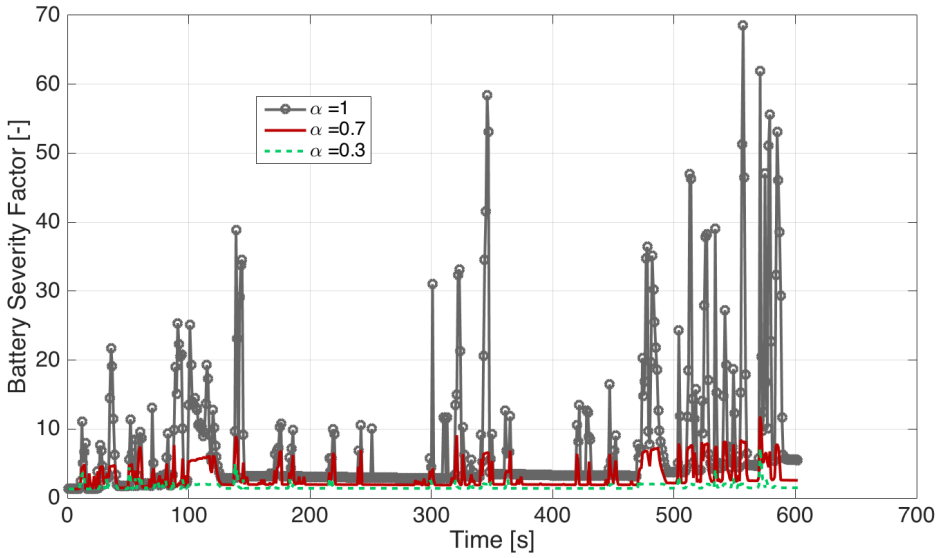

Figure 4.10: Battery severity factor profile for US06 with different α values

The CVT ratio is pre-optimized based on vehicle speed and wheel power request as described in section 4.4.1, and it is depicted in Figure 4.12. The CVT ratio leads to engine operating points shown in Figure 4.13. It is clear that the engine is tracking the OOL in all three cases, however, with different values of α, the engine operation is different. With less electric assist, there are more points at high power in the case of $\alpha = 0.3$, and the root mean square value of engine power is 21kW, while in the case of $\alpha = 1$, the root mean square value of engine power is 19kW.

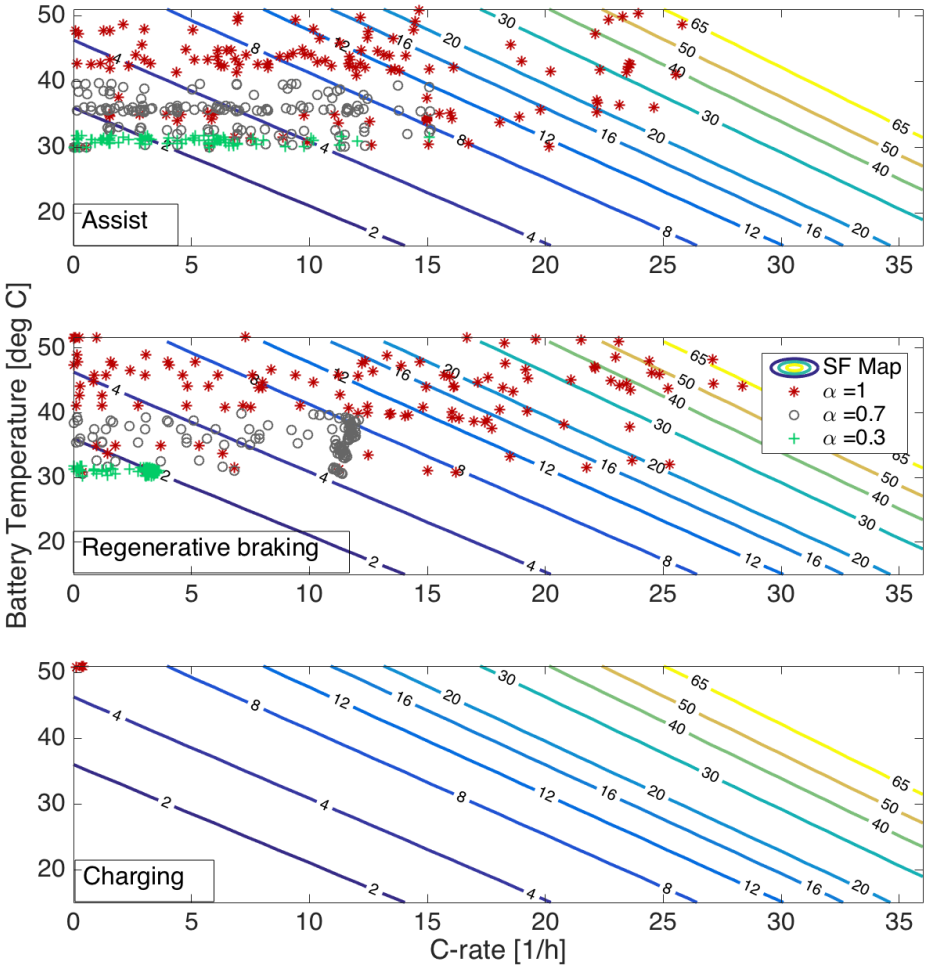

Figure 4.11: Battery severity factor distribution for US06 with different α values

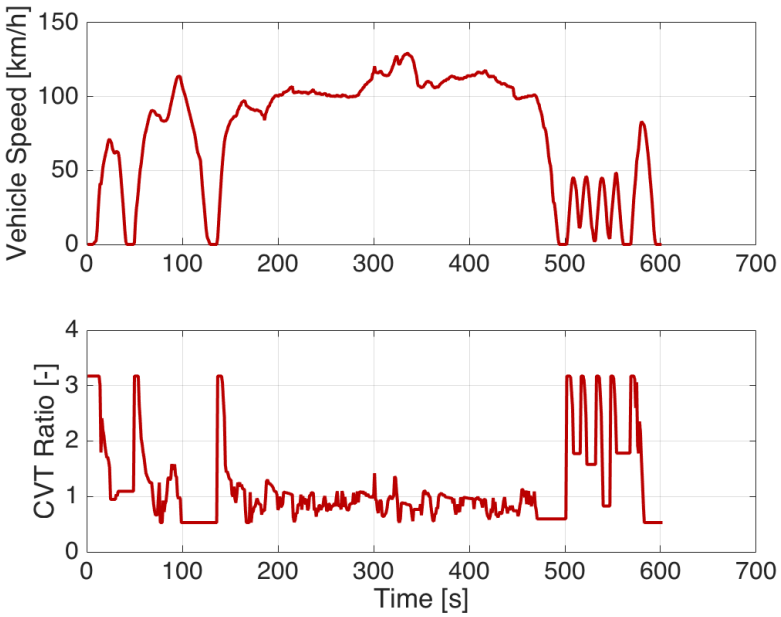

Figure 4.12: CVT Ratio for US06

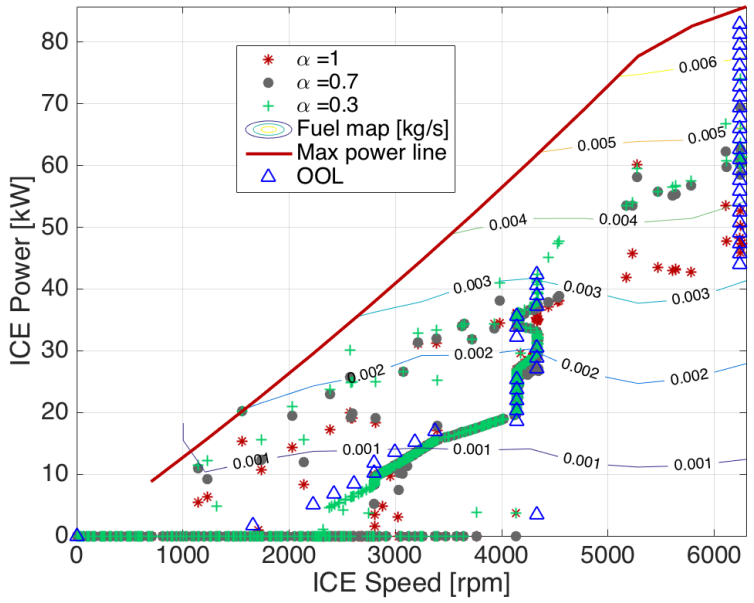

Figure 4.13: Engine operating points for US06 with different α values

Federal Urban Driving Schedule

FUDS simulates an urban route of 7.5 miles (12.07 km) with frequent stops. The maximum speed is 56.7 miles/h (91.2 km/h) and the average speed is 19.6 miles/h (31.5 km/h) with a duration of 1372 seconds.

Performance results for the Pareto front of the controller that optimally tradeoffs battery capacity degradation with engine fuel consumption are presented in Figure 4.14 and the values are listed in Table 4.2. As before, this is achieved by sweeping the weighting factor α from 0.1 to 1. The Pareto front indicate that a fundamental tradeoff exists between fuel economy and battery life span for city driving conditions as well. According to the data in Table 4.2, the controller can reduce the effective Ah processed by 98% at a cost of 25% more fuel consumption. If one compare the Pareto front of FUDS (Figure 4.14) with that of US06 (Figure 4.5), the shape is almost the same, however, for US06, the data points concentrate on the left side while for FUDS there are more points on the right, which means that aging effect can be substantially reduced with small weight on aging cost for US06, which is not true for FUDS. If we choose the performance measure from $\alpha = 1$ as the nominal conditions, the relative optimality is defined as the ratio of normalized reduction on effective Ah-throughput and the normalized increase on fuel consumption

$$\frac{\Delta Ah_{eff}}{\Delta m_f} = \frac{Ah_{eff_{max}} - Ah_{eff}}{Ah_{eff_{max}} - Ah_{eff_{min}}} / \frac{m_f - m_{f_{min}}}{m_{f_{max}} - m_{f_{min}}} \tag{4.24}$$

where $Ah_{eff_{max}}$ and $m_{f_{min}}$ correspond to effective Ah-throughput and fuel consumption with $\alpha = 1$, $Ah_{eff_{min}}$ and $m_{f_{max}}$ correspond to effective Ah-throughput and fuel consumption with $\alpha = 0.1$. The results are shown in Figure 4.15. The higher the

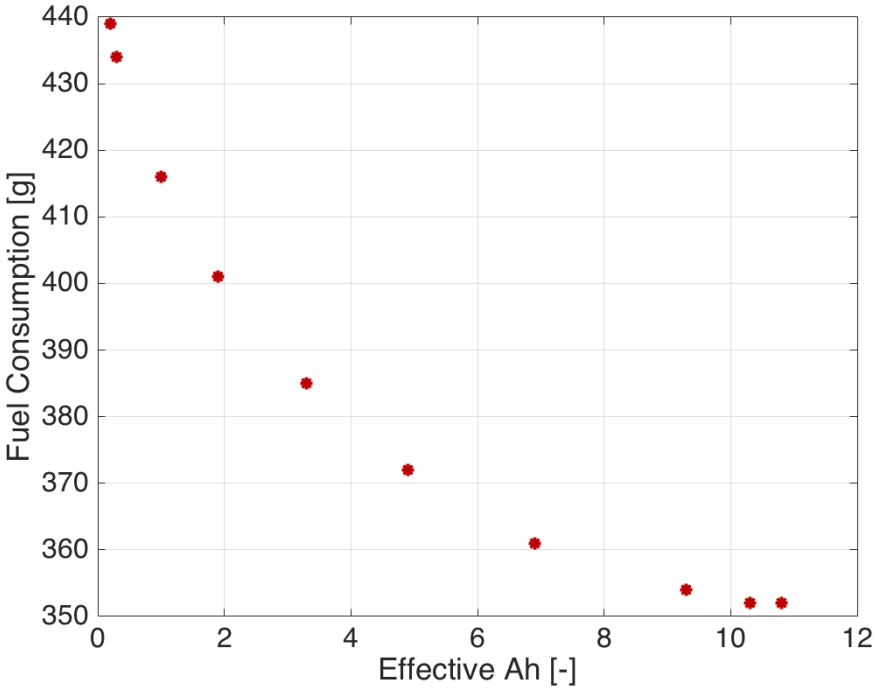

Figure 4.14: Pareto Front for FUDS

Table 4.2: Dynamic Programming Solution for FUDS

α	Fuel Consumption [g]	Ah_{eff}
1	352	10.8
0.9	352	10.3
0.8	354	9.3
0.7	361	6.9
0.6	372	4.9
0.5	385	3.3
0.4	401	1.9
0.3	416	1.0
0.2	434	0.3
0.1	439	0.2

relative optimality is, the more battery life can be saved with 1 gram of fuel sacrifice. The high relative optimality is achieved at high α values for US06, which pushes the points on the Pareto front to the left quickly and makes the Pareto front flat at high α values. On the other hand, the relative optimality is low at high α values for FUDS, which keeps more data points at lower right corner on the Pareto front. The reason for missing data point at $\alpha = 0.9$ for FUDS is that the performance measure for $\alpha = 0.9$ is too close to that for $\alpha = 1$, which is removed to avoid dividing by zero.

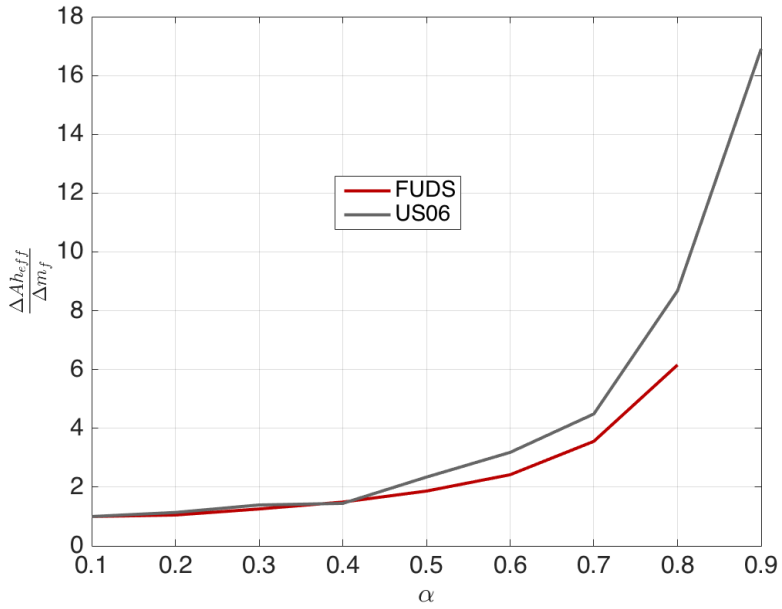

Figure 4.15: Relative Optimality for US06 and FUDS

In order to gain insights on the property of the optimal controller, three solutions are analyzed from the Pareto set, $\alpha = 1, 0.5, 0.2$. Figure 4.16 portrays the SOC trajectories and battery temperature evolutions along with the speed profile. As before,

the fuel optimal case, $\alpha = 1$, has the most dynamic profile of SOC with ΔSOC around 10%. As α decreases, ΔSOC becomes smaller, which is 4.8% and 1.2% for $\alpha = 0.5$ and $\alpha = 0.2$ respectively. It is clearly shown that the optimal controller is able to keep battery temperature within a much lower range when the weighting on aging cost goes up.

The behavior of the system states can be further understood by analyzing the power split profile, which is depicted in Figure 4.17. The same trend can be observed as for the US06 cycle, which is that the usage of electric energy is reduce both directions (positive and negative) as α becomes smaller. When electric power is restricted by the controller at low α value, the electric power is mainly used to launch the vehicle other than assist the engine (Figure 4.18). The reason lies in the nature of the FUDS cycle, which is characterized by frequent start-stop other than high power requirement. The total battery energy throughput is shown in Figure 4.19. As before, the total battery energy throughput decreases with α value and the discharged energy is mainly compensated by the energy from regenerative braking.

Battery severity factor distribution is shown in Figure 4.20. Basically severity factor from three different cases is divided into three levels by battery temperature. Different from US06, the highest severity factor comes from regenerative braking mode. Again, this is mainly because that the driving cycle does not require high propulsion power.

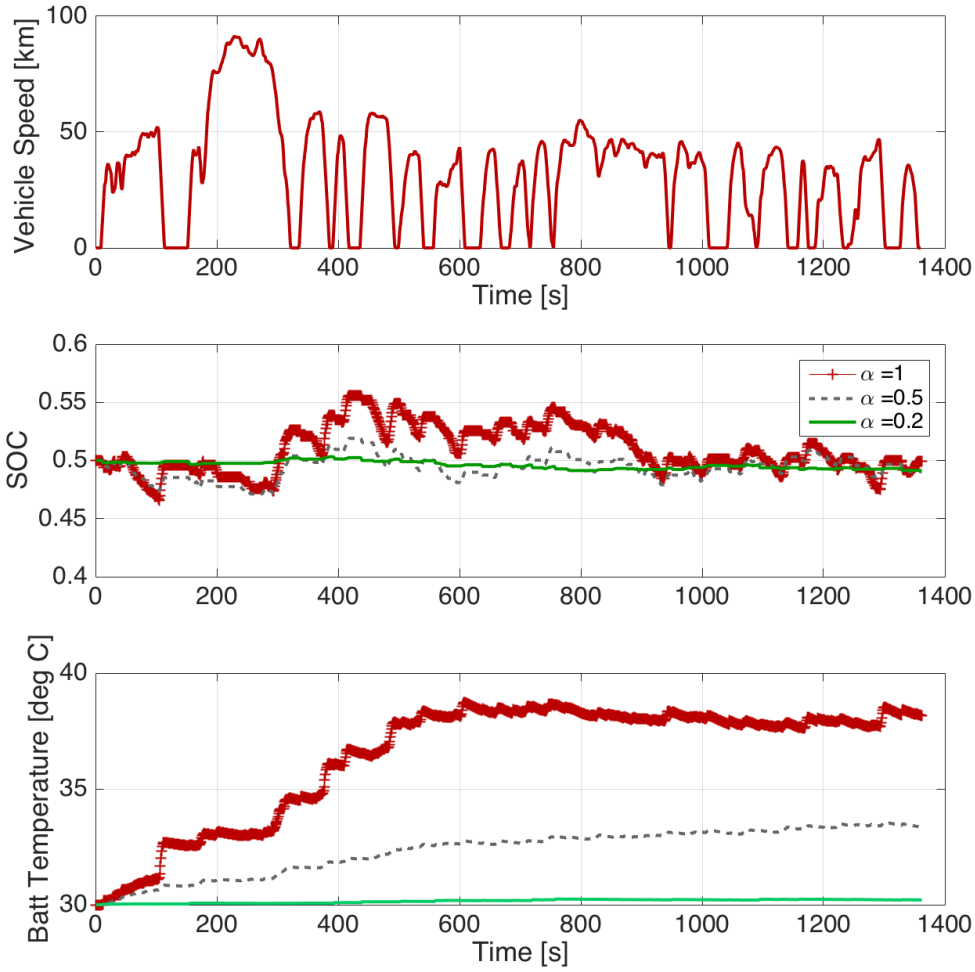

Figure 4.16: Dynamic programming solutions for FUDS with different α values

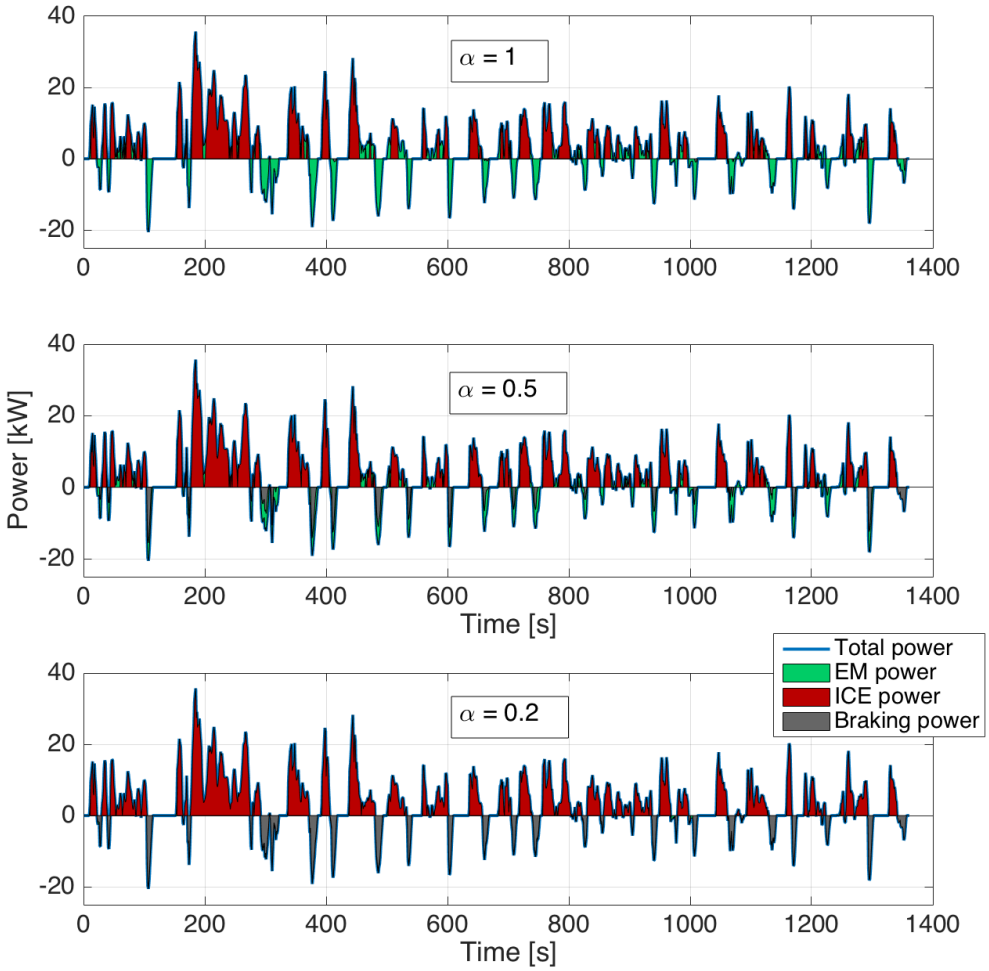

Figure 4.17: Power split for FUDS with different α values

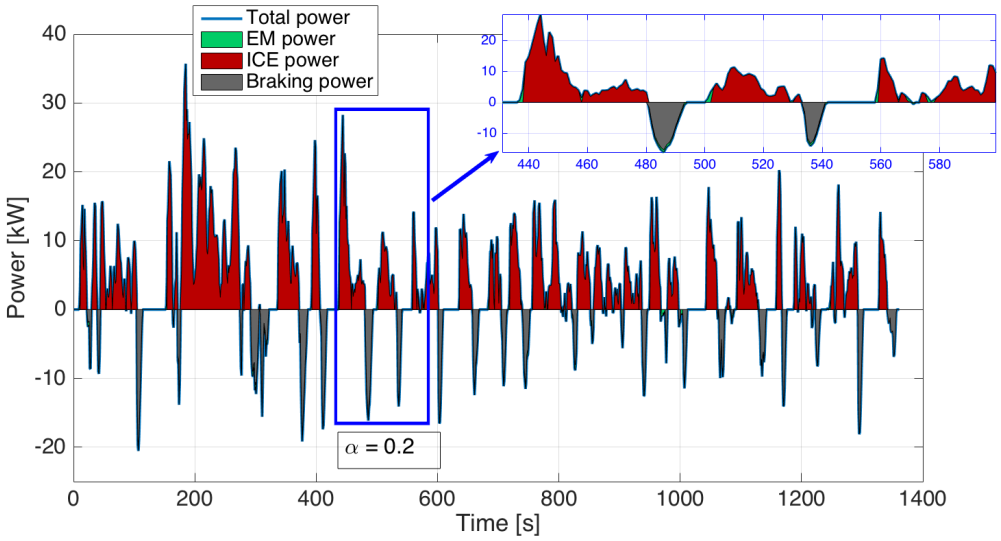

Figure 4.18: Power split for FUDS with $\alpha = 0.2$

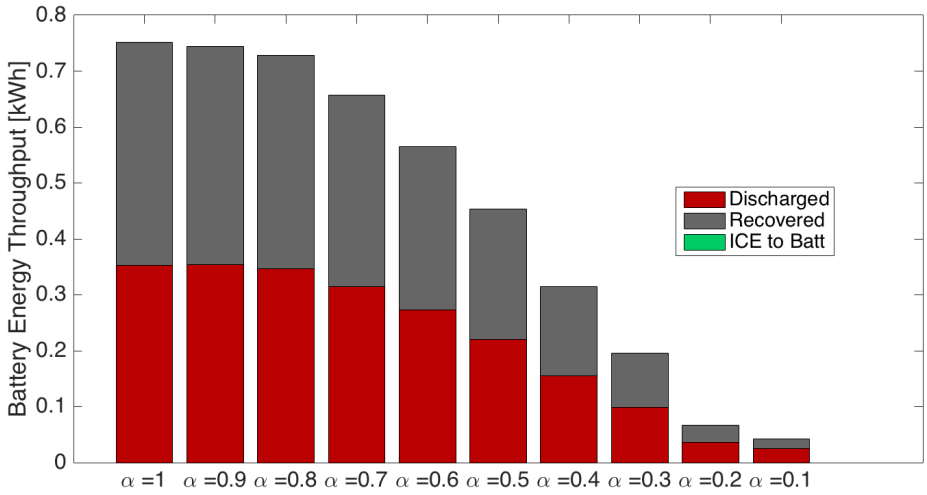

Figure 4.19: Battery energy throughput for FUDS with different α values

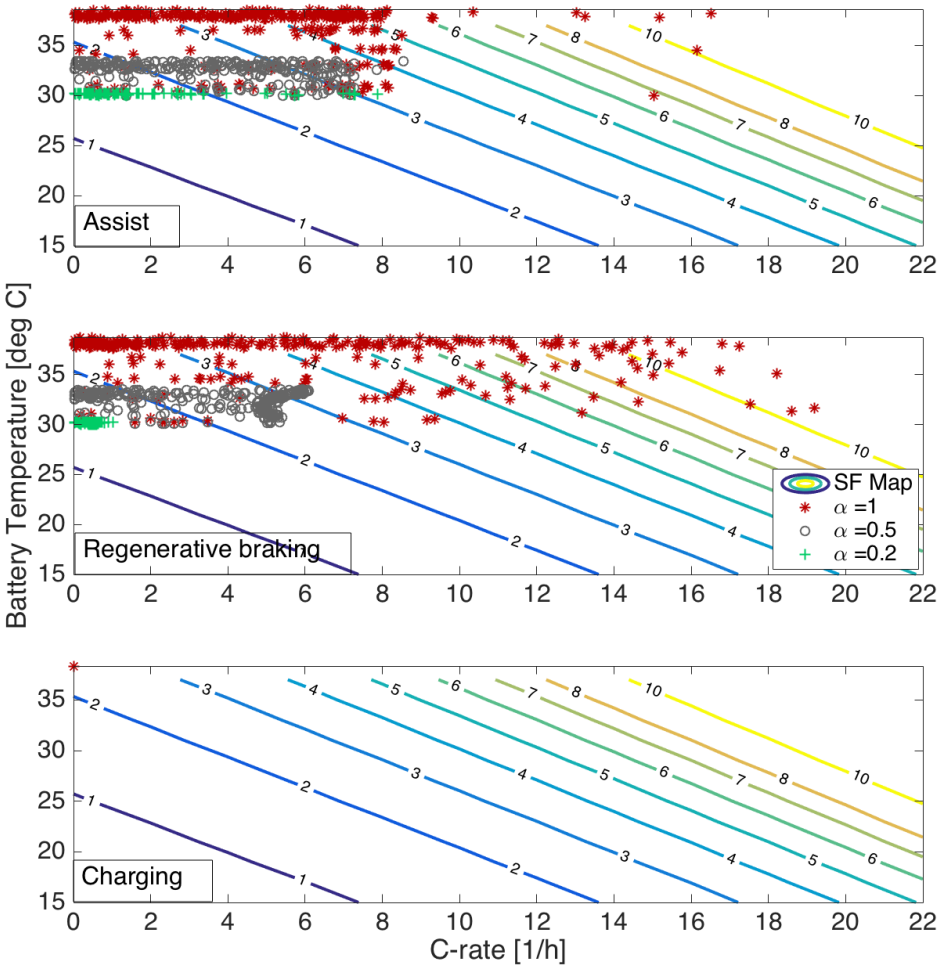

Figure 4.20: Battery severity factor distribution for FUDS with different α values

The optimized CVT ratio for FUDS is illustrated in Figure 4.21 (a), which leads to the engine operating points shown in Figure 4.21 (b). The transmission tries to make the engine operate on the optimal operating line, though it is not always possible due to the mismatch of the road request and powertrain limits. The average engine power corresponding to $\alpha = 1, 0.5 and 0.2$ are 3.6kW, 3.9kW and 4.2kW. Since the driving cycle is an urban driving characterized by low power, the engine output power is low.

Different Driving Cycles

In addition to US06 and FUDS, the results of two more driving cycles are presented, which are Manhattan city driving and Artemis urban driving schedule. Manhattan simulates city bus line of 2.1 miles (3.33 km) with frequent stops. The maximum speed is 18.7 miles/h (30.1 km/h) and the average speed is 6.8 miles/h (11 km/h) with a duration of 1089 seconds. Artemis driving cycle is designed based on European real world driving patterns, which is consist of three driving schedules: (1) Urban, (2) Rural road and (3) Motorway. In this work the urban schedule is selected, which has a duration of 920 seconds and distance of 2.8 miles (4.47 km). The maximum speed and average speed of Artemis urban are 36 miles/h (58 km/h) and 10.9 miles/h (17.5 km/h) respectively.

The performance of four driving schedules are summarized and listed in Table 4.3. The Pareto front for each driving cycle is graphically represented in Figure 4.22. The Pareto front is pretty flat at the right hand side for both Manhattan and Artemis urban driving cycles, which means that battery aging effects can be dramatically

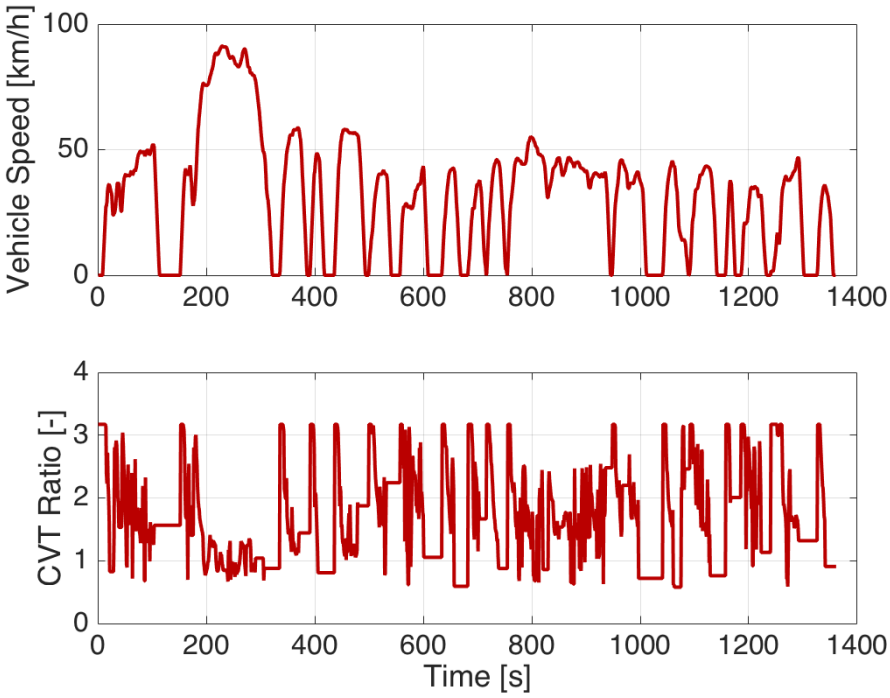

(a) CVT Ratio for FUDS

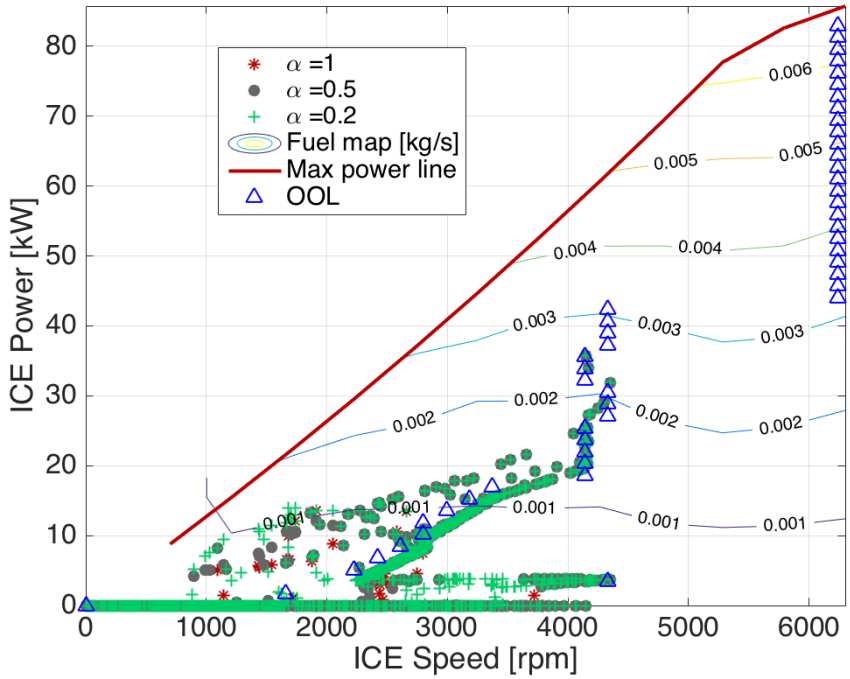

(b) Engine operating points for FUDS with different α values

Figure 4.21: Transmission and Engine Operation for FUDS

reduced without sacrificing much on fuel consumption. In fact, if we look through $\alpha = 0.6 - 1$ of Artemis-urban cycle, there is almost no extra fuel cost to achieve about 34% saving on aging. This observation implies that electric assist and regenerative braking can be done in a more intelligent way with a battery aging-conscious controller, which has no negative impact on the fuel economy.

As shown in Figure 4.23, some amount of energy from engine to battery can be observed when fuel cost is emphasized in the Manhattan driving cycle. This is due to the fact that the Manhattan driving is characterized by low speed, low power and frequent stop-start, thus the benefit of electric assist in terms of saving fuel is significant. Therefore controller intends to bring engine to higher power and more efficient operating regions to produce excessive power and save it in the battery for appropriate electric assist. It is safe to assume that more energy from engine to battery can be observed, if the driving condition is more city-driving-like.

The optimal controller improves battery life not only by reducing the usage of electric energy but also by optimally choosing when and how to use electric energy. This can be proved by comparing the effective Ah-throughput and battery energy throughput from different α values. For instance, in Manhattan driving cycle, the Ah_{eff} with $\alpha = 0.7$ is reduced by 15% compared with that with $\alpha = 1$. However, the amount of battery energy throughput with $\alpha = 0.7$ is only reduced by 6.4% compared with the case with $\alpha = 1$. Moreover, in the Artemis urban driving schedule, with $\alpha = 0.7$, the Ah_{eff} is 37.6% less than that from $\alpha = 1$, but the battery energy throughput is only 9.6% less (Figure 4.24). This observation indicate that, with the

Table 4.3: Summary of DP Results

	US06		FUDS		Manhattan		Artemis-urban	
α	Fuel [g]	Ah_{eff}	Fuel [g]	Ah_{eff}	Fuel [g]	Ah_{eff}	Fuel [g]	Ah_{eff}
1	563	36.8	352	10.8	111	4.1	156	10.1
0.9	569	19.7	352	10.3	111	3.7	156	9.6
0.8	578	10.9	354	9.3	111	3.6	158	8.0
0.7	586	6.7	361	6.9	112	3.5	161	6.3
0.6	594	4.3	372	4.9	116	2.7	166	4.9
0.5	600	3.0	385	3.3	123	2.0	173	3.6
0.4	608	1.9	401	1.9	136	1.2	182	2.4
0.3	618	1.1	416	1.0	145	0.7	194	1.4
0.2	630	0.4	434	0.3	155	0.3	210	0.5
0.1	636	0.2	439	0.2	156	0.3	219	0.2

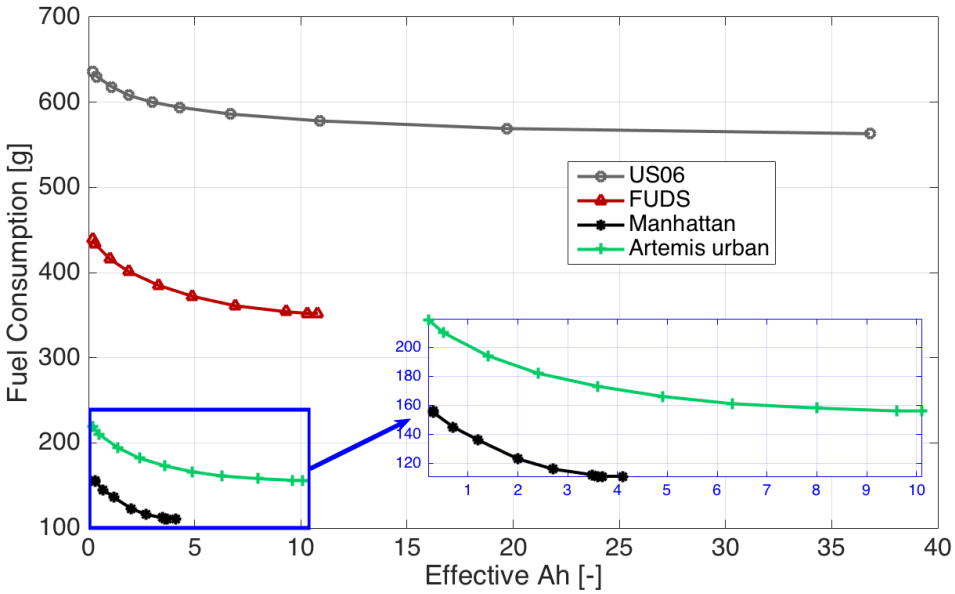

Figure 4.22: Pareto Front

same battery energy-throughput, less aging effects can be achieved by optimally using the energy.

4.4.4 Summary

In this section, an optimal control-based energy management strategy for HEVs is analyzed, which explicitly tradeoffs fuel consumption and battery capacity degradation. The method is called sequential optimization due to the fact that the ratio of a continuously variable transmission is pre-solved based on engine optimal operating line. The observations from the simulation results are:

- There exists a fundamental tradeoff between fuel economy and battery aging;
- The optimal controller reduces battery aging effect by either bringing down the total battery energy throughput or reducing the severity factor;
- It is possible to save battery life at virtually no cost of fuel economy, if an appropriate weighting factor is assigned to each objective;
- The optimal controller tries to avoid using the engine to charge the battery when aging cost is emphasized.

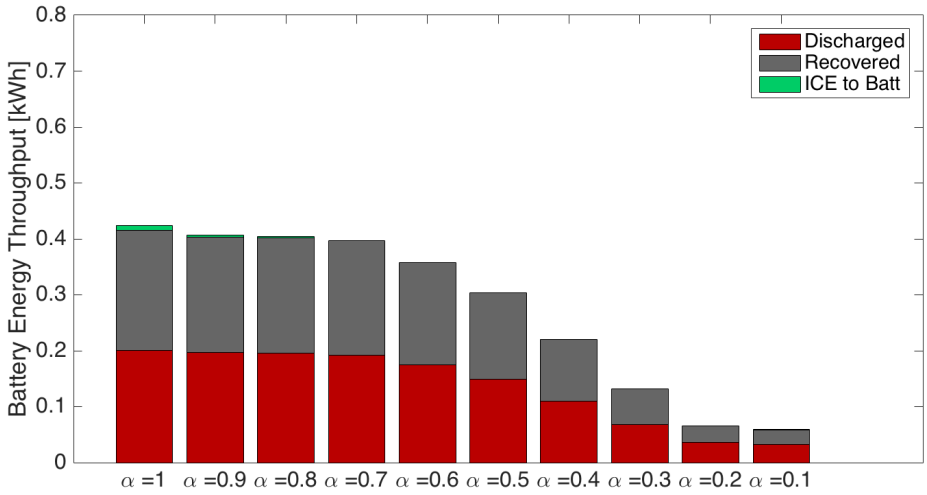

Figure 4.23: Battery energy throughput for Manhattan with different α values

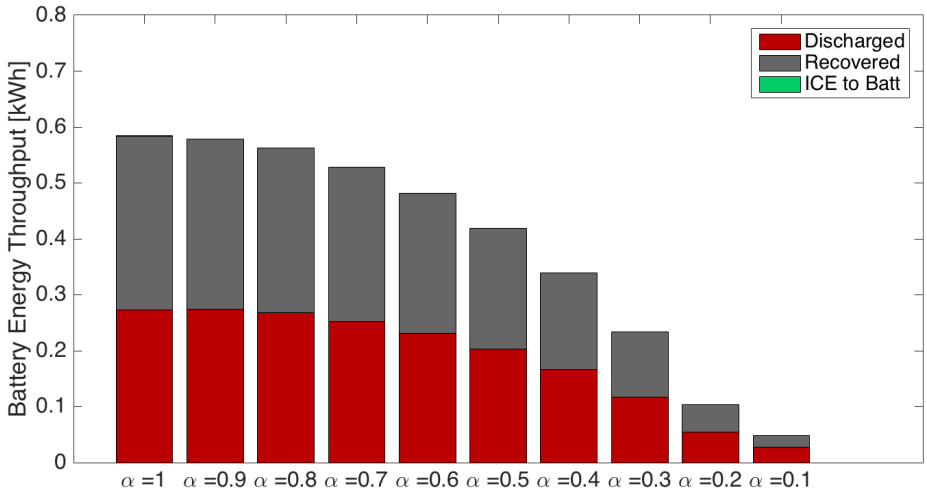

Figure 4.24: Battery energy throughput for Artemis-urban cycle with different α values

4.5 Systematic optimization strategy

While the CVT ratio is determined by the engine OOL, which aims to achieve minimum engine fuel consumption for a given engine power in the sequential optimization strategy, the CVT ratio is considered as a second control input in addition to torque split in the approach introduced in this section, which is called systematic optimization strategy. Instead of shifting only for best engine efficiency, the CVT ratio is optimally selected to account for the overall powertrain efficiency including the instances when regenerative braking is taking place.

4.5.1 Problem formulation

The objective function to be minimized is still (4.7), and the complete optimal control problem statement is (4.25). The difference lies in that $r_{cvt}(t)$ is a control variable instead of a disturbance, thus additional constraints on speed are added including physical limits of two machines and the connection among wheel speed, engine speed and electric machine speed.

$$\min : \int_0^{t_f} \alpha \cdot \frac{\dot{m}_f(t) - \bar{\dot{m}}_f}{m_{f,diff}} + (1-\alpha) \cdot \frac{\sigma(t) \cdot |I_{cell}(t)|}{Ah_{eff,diff}} dt$$

subject to

$$\begin{aligned}
&S\dot{O}C(t) = -\frac{I_{cell}(t)}{Q_{cell} \cdot 3600} \\
&\dot{\theta}_{batt}(t) = \frac{\dot{q}_{batt}(t) + h_{batt} \cdot A_{surface} \cdot (\theta_{cool} - \theta_{batt}(t))}{M_{batt} \cdot C_{p_{batt}}} \\
&T_{road}(t) = (T_{ice}(t) + T_{em}(t)) \cdot \eta_{cvt}^{k} \cdot r_{cvt}(t) \cdot r_{diff} + T_{brake}(t) \\
&\omega_{ice}(t) = \omega_{em}(t) = \omega_{wh}(t) \cdot r_{cvt}(t) \cdot r_{diff} \\
&0 \leqslant T_{ice}(t) \leqslant T_{ice_{max}}(\omega_{ice}(t)) \\
&T_{em_{min}}(\omega_{em}(t)) \leqslant T_{em}(t) \leqslant T_{em_{max}}(\omega_{em}(t)) \\
&T_{brake}(t) \leqslant 0 \\
&\omega_{ice_{min}} \leqslant \omega_{ice}(t) \leqslant \omega_{ice_{max}} \\
&\omega_{em_{min}} \leqslant \omega_{em}(t) \leqslant \omega_{em_{max}} \\
&r_{cvt_{min}} \leqslant r_{cvt}(t) \leqslant r_{cvt_{max}} \\
&I_{cell_{min}} \leqslant I_{cell}(t) \leqslant I_{cell_{max}} \\
&SOC_{min} \leqslant SOC(t) \leqslant SOC_{max} \\
&SOC(0) = SOC_0 \\
&SOC(t_f) = SOC_0 \\
&\theta_{batt}(0) = \theta_{batt,0}
\end{aligned} \tag{4.25}$$

One can clearly see the difference comparing the following mathematical expression with (4.15).

$$u^* = \underset{u}{\text{argmin}} : J = \int_0^{t_f} \alpha \cdot \frac{\dot{m}_f(u,t) - \bar{\dot{m}}_f}{m_{f,diff}} + (1-\alpha) \cdot \frac{\sigma(x,u,t) \cdot |I_{cell}(x,u,t)|}{Ah_{eff,diff}} dt$$

subject to

$$\begin{aligned} \dot{x} &= f(x,u,v) \\ x(0) &= x_0 \\ x(t_f) &= x_T \\ x(t) &\in \chi \\ u(t) &\in \mathcal{U} \end{aligned} \tag{4.26}$$

where

$$x = \begin{bmatrix} SOC \\ \theta_{batt} \end{bmatrix} \quad u = \begin{bmatrix} T_{em} \\ r_{cvt} \end{bmatrix} \quad v = \begin{bmatrix} T_{road} \\ \omega_{wh} \end{bmatrix}$$

Thus the problem to be solved is the energy management problem formulated as an optimal control problem with the objective function in (4.7) subjected to the vehicle model in (3.1)-(3.22) and charge-sustenance condition $SOC(0) = SOC(t_f) = SOC_0$ with SOC_0 being the initial state of charge.

4.5.2 PMP solution

As one of the two optimal control theories that can be applied to constrained optimal control problems, Pontryagin's Minimum Principle is very powerful in generating solution candidates with less computational time compared with Dynamic Programming. Moreover, PMP allows to redefine the global optimal control problem

in terms of local conditions expressed by equations (2.11)-(2.12) and by the instantaneous minimization (2.10), which will help to gain insights on designing the real-time implementable strategy. Therefore, PMP-based optimal solutions are presented and analyzed in this section.

According to the problem statement in (4.25), the Hamiltonian is written as:

$$\begin{aligned}\mathscr{H} =&\alpha \cdot \frac{\dot{m}_f(t) - \bar{\dot{m}}_f}{m_{f,diff}} + (1-\alpha) \cdot \frac{\sigma(t) \cdot |I_{cell}(t)|}{Ah_{eff,diff}} \\ &+ \lambda_1(t) \cdot (-\frac{I_{cell}(t)}{Q_{cell} \cdot 3600}) \\ &+ \lambda_2(t) \cdot \frac{I_{cell}^2(t) \cdot R_0 \cdot N_s \cdot N_r + h_{batt} \cdot A_{surface} \cdot (\theta_{cool} - \theta_{batt}(t))}{M_{batt} \cdot C_{p_{batt}}}\end{aligned} \tag{4.27}$$

where $\lambda_1(t)$ and $\lambda_2(t)$ are co-states correspond to SOC and θ_{batt} respectively. Based on the necessary conditions for optimal solution, the trajectory of λ_i should evolve with the dynamics described in (2.12), which are

$$\begin{aligned}\dot{\lambda}_1(t) =& -\frac{\partial \mathscr{H}}{\partial SOC} = -\frac{1-\alpha}{Ah_{eff,diff}} \cdot (\frac{\partial \sigma}{\partial SOC} \cdot |I_{cell}(t)| + \sigma \cdot \frac{\partial |I_{cell}|}{\partial SOC}) \\ &- \lambda_1(t) \cdot \frac{\partial \dot{SOC}}{\partial SOC} \\ &- \frac{\lambda_2(t)}{M_{batt} \cdot C_{p_{batt}}} \cdot (2I_{cell} \cdot R_0 \frac{\partial I_{cell}}{\partial SOC} + I_{cell}^2 \cdot \frac{\partial R_0}{\partial SOC})\end{aligned} \tag{4.28}$$

$$\begin{aligned}\dot{\lambda}_2(t) =& -\frac{\partial \mathscr{H}}{\partial \theta_{batt}} = -\frac{1-\alpha}{Ah_{eff,diff}} \cdot (\frac{\partial \sigma}{\partial \theta_{batt}} \cdot |I_{cell}(t)| + \sigma \cdot \frac{\partial |I_{cell}|}{\partial \theta_{batt}}) \\ &- \lambda_1(t) \cdot \frac{\partial \dot{SOC}}{\partial \theta_{batt}} \\ &- \frac{\lambda_2(t)}{M_{batt} \cdot C_{p_{batt}}} \cdot (2I_{cell} \cdot R_0 \frac{\partial I_{cell}}{\partial \theta_{batt}} + I_{cell}^2 \cdot \frac{\partial R_0}{\partial \theta_{batt}} - h_{batt} \cdot A_{surface})\end{aligned} \tag{4.29}$$

All the partial differential terms are pre-calculated and implemented as maps. The shape of each term is shown in Figure 4.25 and Figure 4.26. The evolution of

the co-states obtained by integration of (4.28) and (4.29) are used in the definition of the Hamiltonian function (4.34); in addition to this, the initial co-state values $\lambda_i(0)$ must satisfy all the boundary conditions. In this problem the boundary conditions are:

$$SOC(0) = SOC(t_f) = 0.5 \tag{4.30}$$

$$\theta_{batt}(0) = 30 \tag{4.31}$$

As the final value of battery temperature ($\theta_{batt}(t_f)$) is not specified, the additional necessary condition for optimality is

$$\lambda_2(t_f) = 0 \tag{4.32}$$

To impose boundary conditions on both the state and co-state variables, an iterative procedure is necessary, which is called shooting method. The procedure can be described as:

1. assign an arbitrary initial value to co-states $\lambda_i(0)$;
2. solve the problem by minimizing Hamiltonian and find the corresponding control sequence;
3. integrate both state dynamic equations and co-state dynamic equations to obtain the value of $SOC(t_f)$ and $\lambda_2(t_f)$, and compare them with the reference values;
4. repeat the above steps if the boundary conditions are not satisfied.

The shooting method can be implemented only when future driving conditions are known a priori, which can be explained by its iterative nature, which also demonstrates the fact that applying Pontryagins Minimum Principle requires a-priori knowledge of the entire optimization horizon, which confines real-time implementation to cases in which the load on the vehicle is either known or predictable.

4.5.3 Simulation results

The minimization of the Hamiltonian function with respect to the control variables, namely T_{em} and r_{cvt} can be done numerically. Given the admissible range of control values defined by (3.10) and (3.14). The combination of T^*_{em} and r^*_{cvt} that minimizes the Hamiltonian can be determined by enumeration of a finite number of admissible control values. In other words, at each instant, the Hamiltonian (4.34) is evaluated for each of the control combination in a set of total $N_{u1} \times N_{u2}$ options. The control inputs that minimize the Hamiltonian is chosen and applied to the system, and also used to update the numerical solution of the co-state dynamic equations. A way to illustrate the minimization of the Hamiltonian is to visualize it at a given instant, which is done in Figure 4.27. Infeasible conditions exist when the combination of T^*_{em} and r^*_{cvt} can not satisfy either the wheel speed or the wheel torque request. The decision point is the lowest point among all the feasible points, which is the red dot as in Figure 4.27. The methodology outlined is applied to multiple driving cycles, among which the results of US06 and FUDS are analyzed in detail.

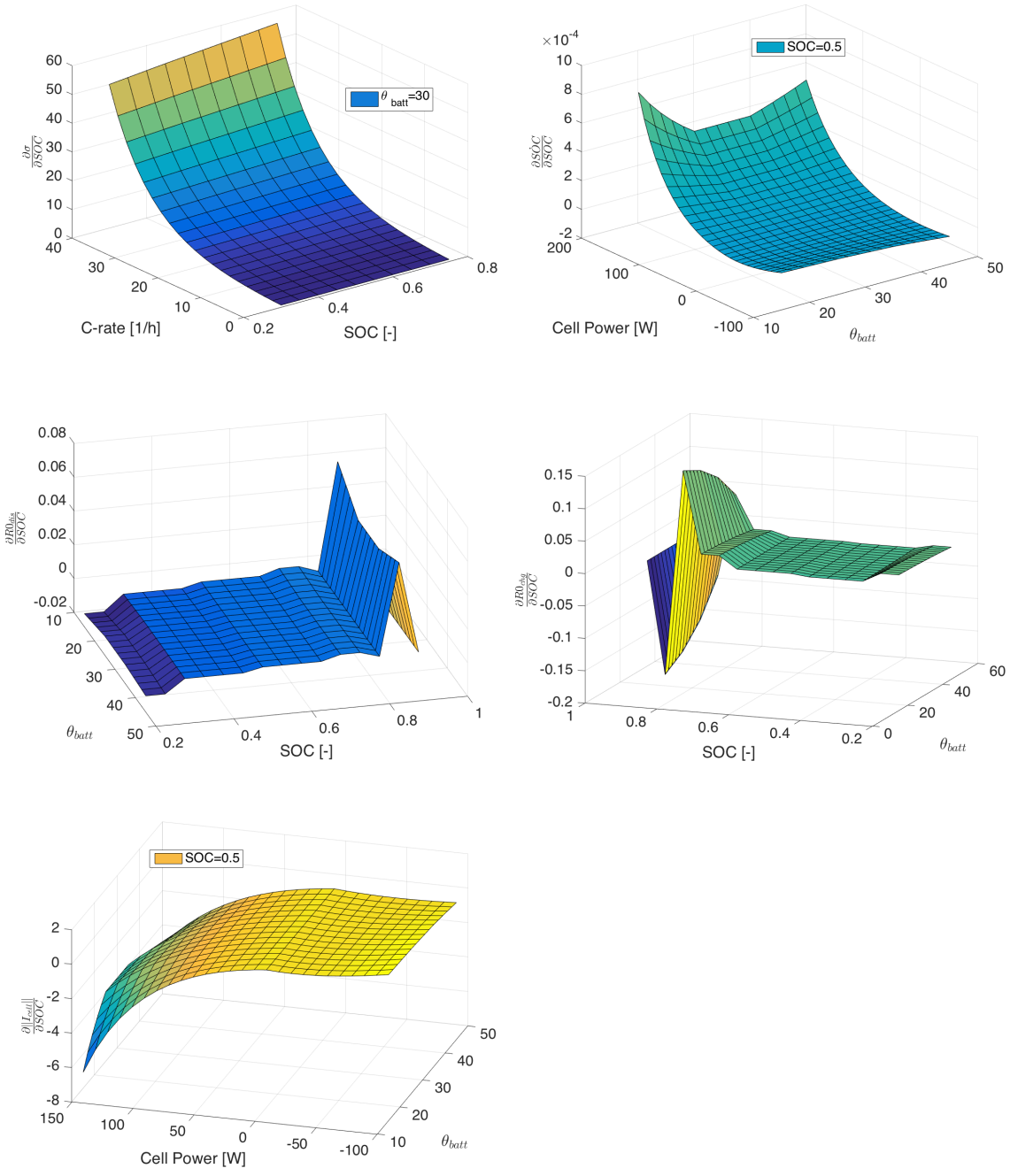

Figure 4.25: λ_1 Dynamics

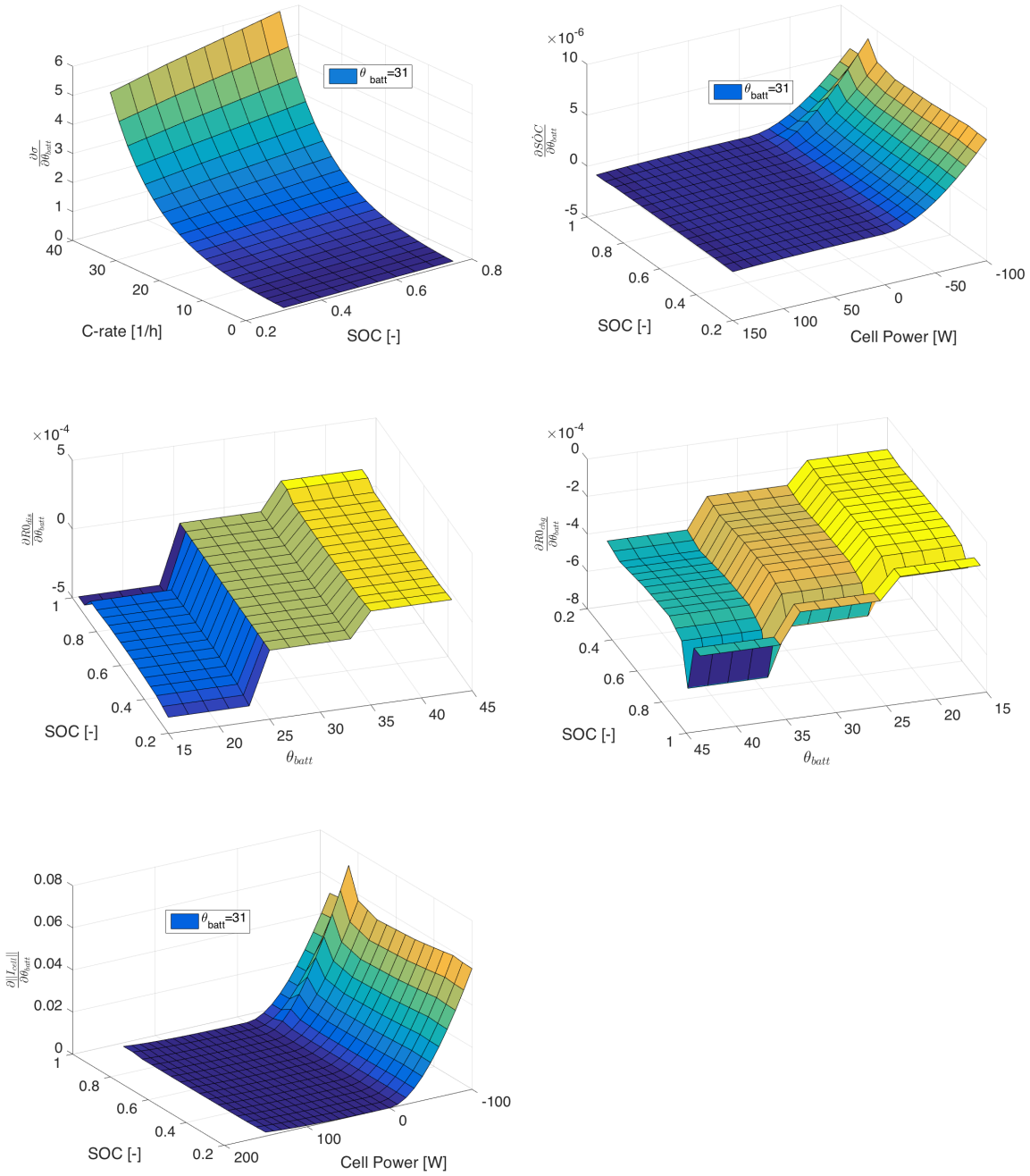

Figure 4.26: λ_2 Dynamics

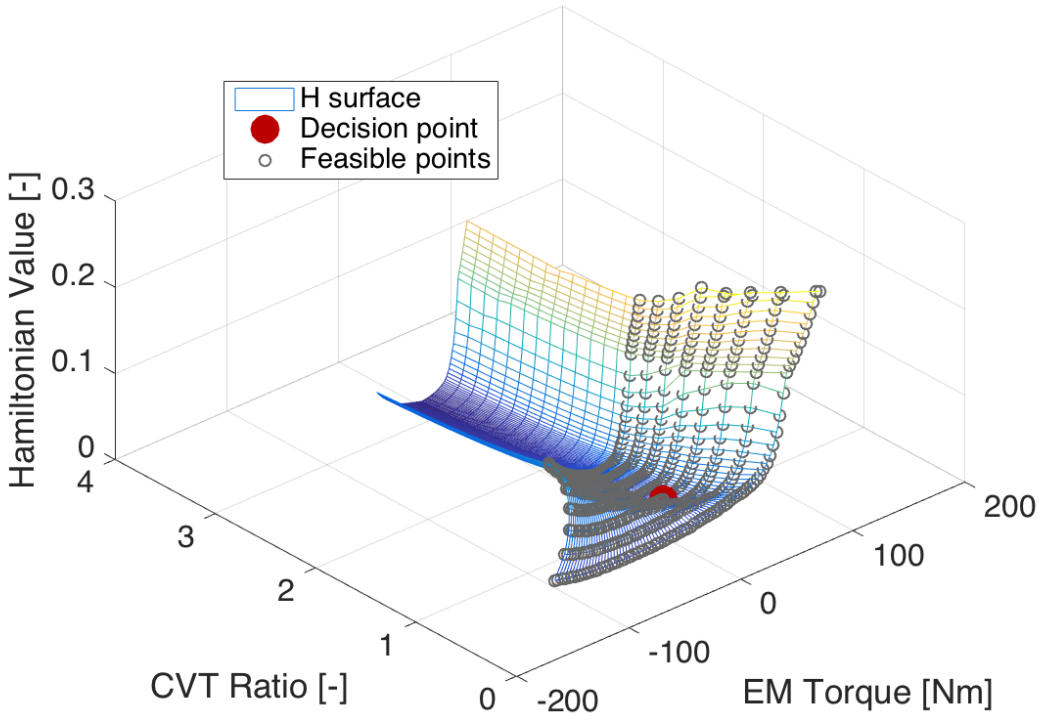

Figure 4.27: Visualization of the Hamiltonian at one instant (t = 300 s in driving cycle US06)

US06

It is well known that the optimality of PMP solution is highly sensitive to the initial co-state values [50, 26]. Thus, the optimal state trajectory and co-state trajectory are corresponding to each other. Figure 4.28 shows the results for US06 driving schedule, and the results of three different values of α are illustrated. With decreasing of α, SOC is less fluctuated thus less electric energy is used and less aging effects are expected, which demonstrates the right trend. The battery temperature trajectories can also confirm the fact that by varying the weight on aging cost, lower battery

temperature can be achieved, which implies less aging effects.

It can be observed that the optimal co-state trajectories show a trend when α varies. The magnitude of λ_1 is decreasing with α. It is clear that λ_1 is the most influential tuning parameter to keep the charge-sustanance criteria. If we interpret λ_1 as the weight required to fulfil the charge-sustaining constraint, this weight is decreasing when weight on aging increases. Since the use of battery is limited when weight on aging increases, which is when α decreases, the effort required to keep SOC sustaining becomes less, and therefore the magnitude of λ_1 decreases with α. The same behavior of λ_2 can be observed. First of all, $\lambda_2(t_f) = 0$ is a necessary condition for optimality, so all three trajectories converge to 0 at the end of the cycle. The trajectory is on top of each other and the magnitude is increasing with decreasing of α. According to equation (4.29), the rate of change of λ_2 is the sensitivity of Hamiltonian with respect to battery temperature θ_{batt}. In addition, the dominant term in (4.29) is $\frac{\partial \sigma}{\partial \theta_{batt}}$, which increases when θ_{batt} increases (Figure 4.29). Therefore the higher the battery temperature the bigger the rate of change of λ_2. With the same time window and final value, the initial value of λ_2 will be higher with higher battery temperature trajectory, which is resulted from a lower α. With the above observations, finding the optimal initial co-state value will be less time-consuming.

Another important observation is that both λ_1 and λ_2 are almost constant over the entire cycle. In Figure 4.28, the change of λ_1 is very small for all three cases. Although, it is clearly shown that λ_2 decreases from an initial value to zero over the driving cycle, the magnitude of λ_2 is so small that the absolute change is negligible.

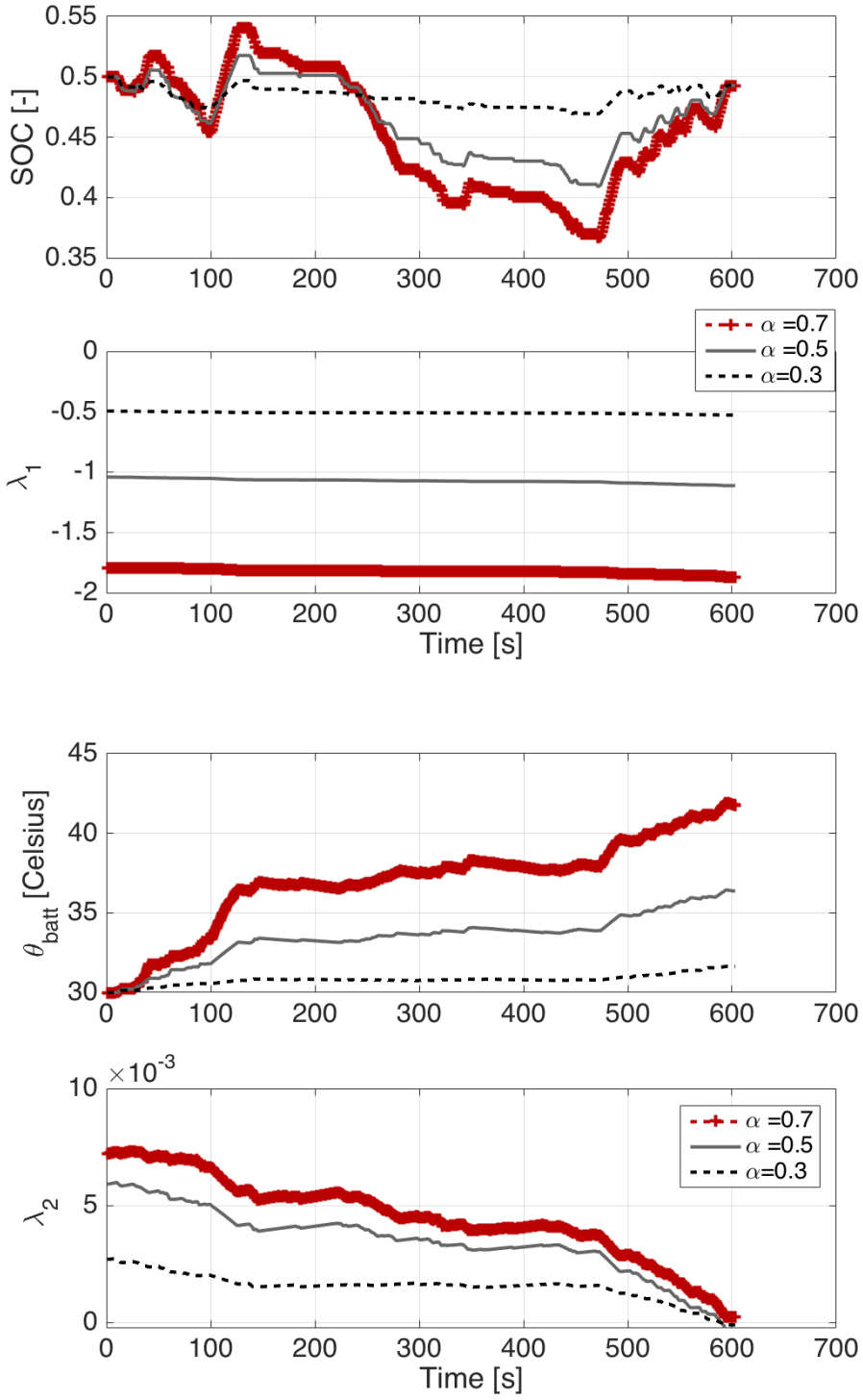

Figure 4.28: States and co-states trajectories over US06 with ambient temperature at 30 °C

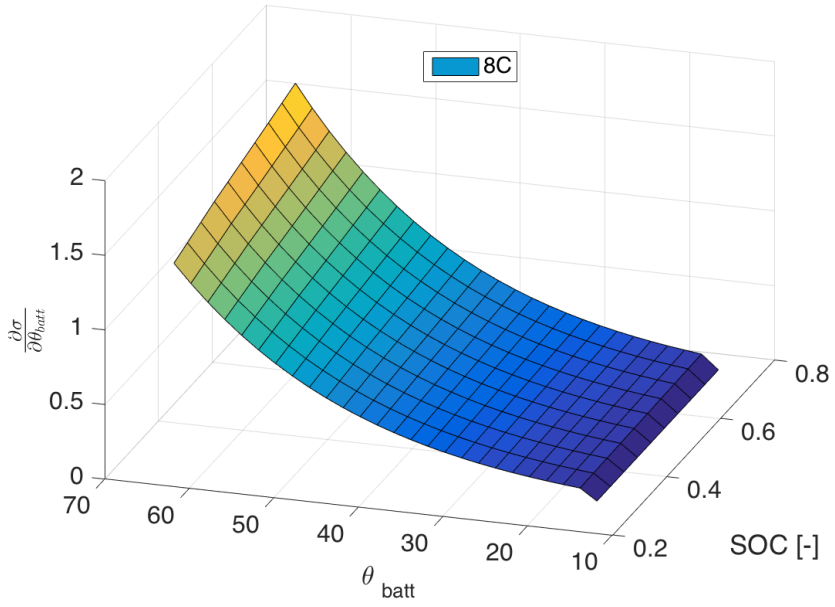

Figure 4.29: $\frac{\partial \sigma}{\partial \theta_{batt}}$ at 8C

Based on this observation, PMP with constant co-states are implemented and tested. The simulation results are compared with results from PMP with dynamic co-states. Results from dynamic programming are also included as a benchmark. Figure 4.30 shows the states trajectories with $\alpha = 0.7$. The SOC trajectories are very close to each other while the battery temperature profiles have some small differences. The performance measure of three controllers are summarized and listed in Table 4.4. The fuel consumption of three controllers are very similar for all α values, and the difference is less than 1%. On the other hand, effective Ah-throughput varies from different controllers, which is resulted from the difference on battery temperature profiles. Generally speaking, the three controllers can achieve comparable performance

when changing the value of α, thus Pareto front of similar shapes.

Table 4.4: Simulation Results for US06

	PMP with constant co-states		PMP with dynamic co-states		DP	
α	Fuel [g]	Ah_{eff}	Fuel [g]	Ah_{eff}	Fuel [g]	Ah_{eff}
1	535	72.6	536	74.3	539	67.1
0.7	562	11.0	565	9.0	568	8.3
0.5	581	4.3	584	3.6	586	3.4
0.3	604	1.1	606	0.59	607	0.8

FUDS

Similar analysis is conducted for FUDS cycle to demonstrate the generality of some properties that PMP solutions have. First of all, PMP based controller reduces the use of battery energy when weight on battery increases (α decreases), which is as expected, thus lower battery temperature and less aging effects (Figure 4.31). The same trend on co-states can be observed when change the value of α, which is that the magnitude of both co-states decreases when α decreases. In addition, the dynamics of both co-states are very small, which makes the constant co-state approximation still valid. The performance of the PMP controller with constant co-state are compared with the results from PMP with dynamic co-state and Dynamic Programming, which are shown in Figure 4.32. The behavior of the states from PMP controller with constant co-state are very close to the global optimal solution that is generated by DP. In fact, the PMP controller with constant co-state performs better with FUDS than it does with US06 in terms of the closeness to DP solution. The performance measure of

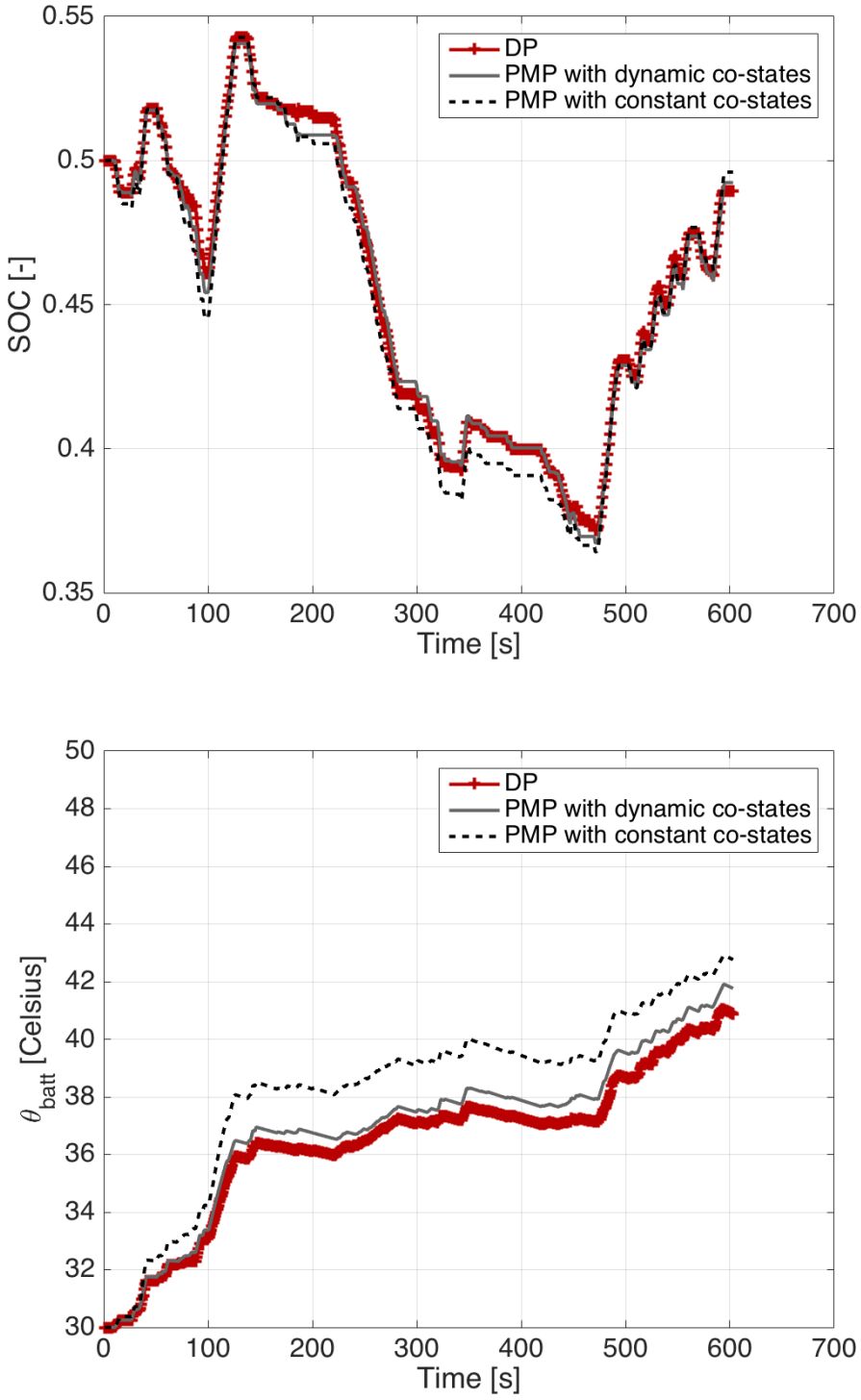

Figure 4.30: States trajectories from different controllers with $\alpha = 0.7$ over US06 with ambient temperature at 30 °C

three controllers with different α values are summarized in Table 4.5, which confirms the above statement.

Table 4.5: Simulation Results for FUDS

	PMP with constant co-states		PMP with dynamic co-states		DP	
α	Fuel [g]	Ah_{eff}	Fuel [g]	Ah_{eff}	Fuel [g]	Ah_{eff}
1	335	11.9	336	11.9	332	11.3
0.7	341	8.9	346	7.5	343	7.2
0.5	364	4.1	369	3.4	367	3.3
0.3	402	0.8	403	0.8	402	0.9

4.5.4 Summary

In this section, a PMP-based energy management strategy for HEVs is analyzed, which explicitly tradeoffs fuel consumption and battery capacity degradation. The difference between the problem solved in this section and the one solved in the previous section is that the ratio of a continuously variable transmission is included as a second control variable in addition to torque split. The insights gained from the simulation results are the following:

- There exists a fundamental tradeoff between fuel economy and battery capacity degradation;
- PMP-based controller can achieve similar performance as that from DP
- The PMP controller with constant co-states is able to provide close-to-optimal solutions with much simplified implementation and less computational time.

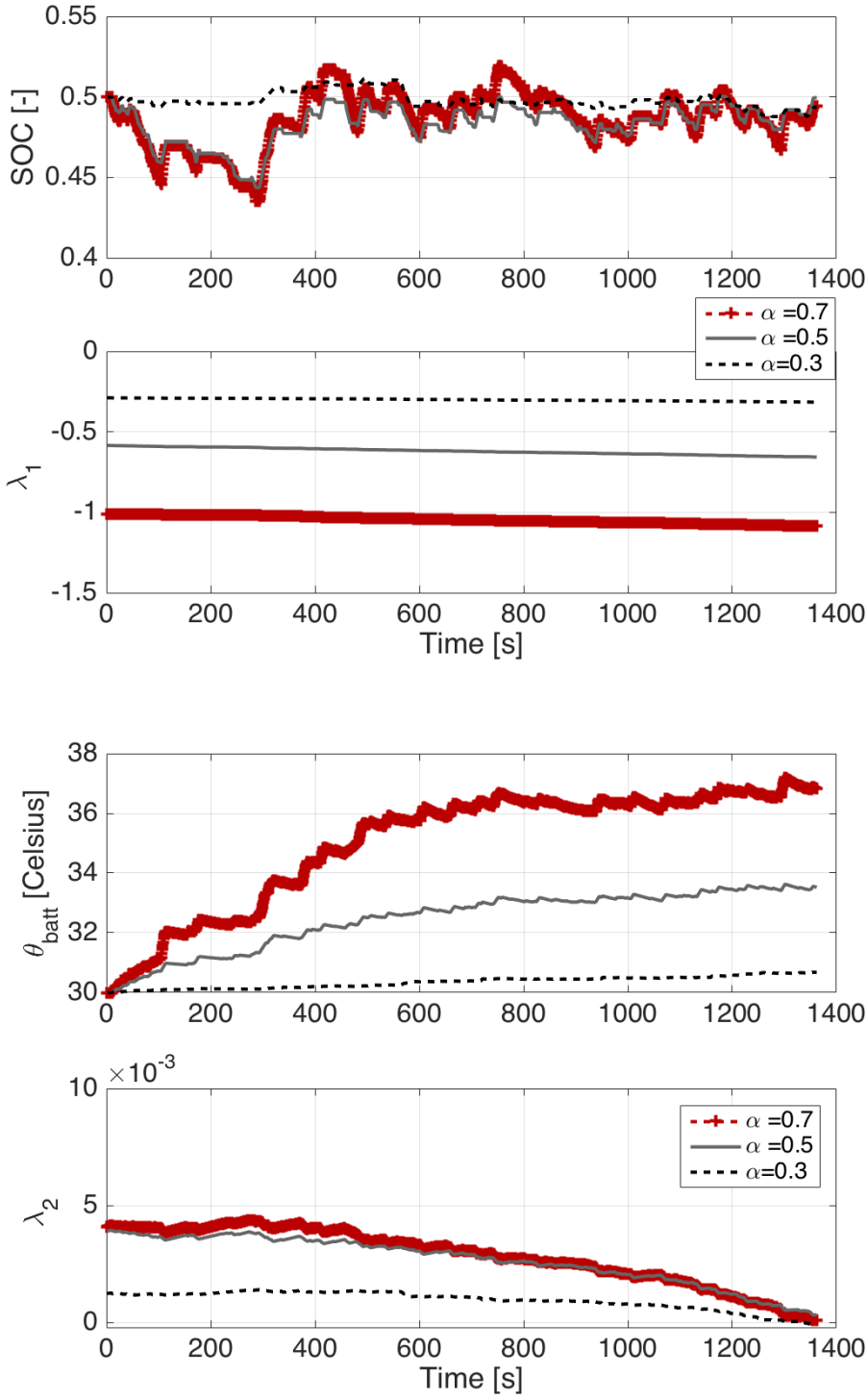

Figure 4.31: States and co-states trajectories over FUDS with ambient temperature at 30 °C

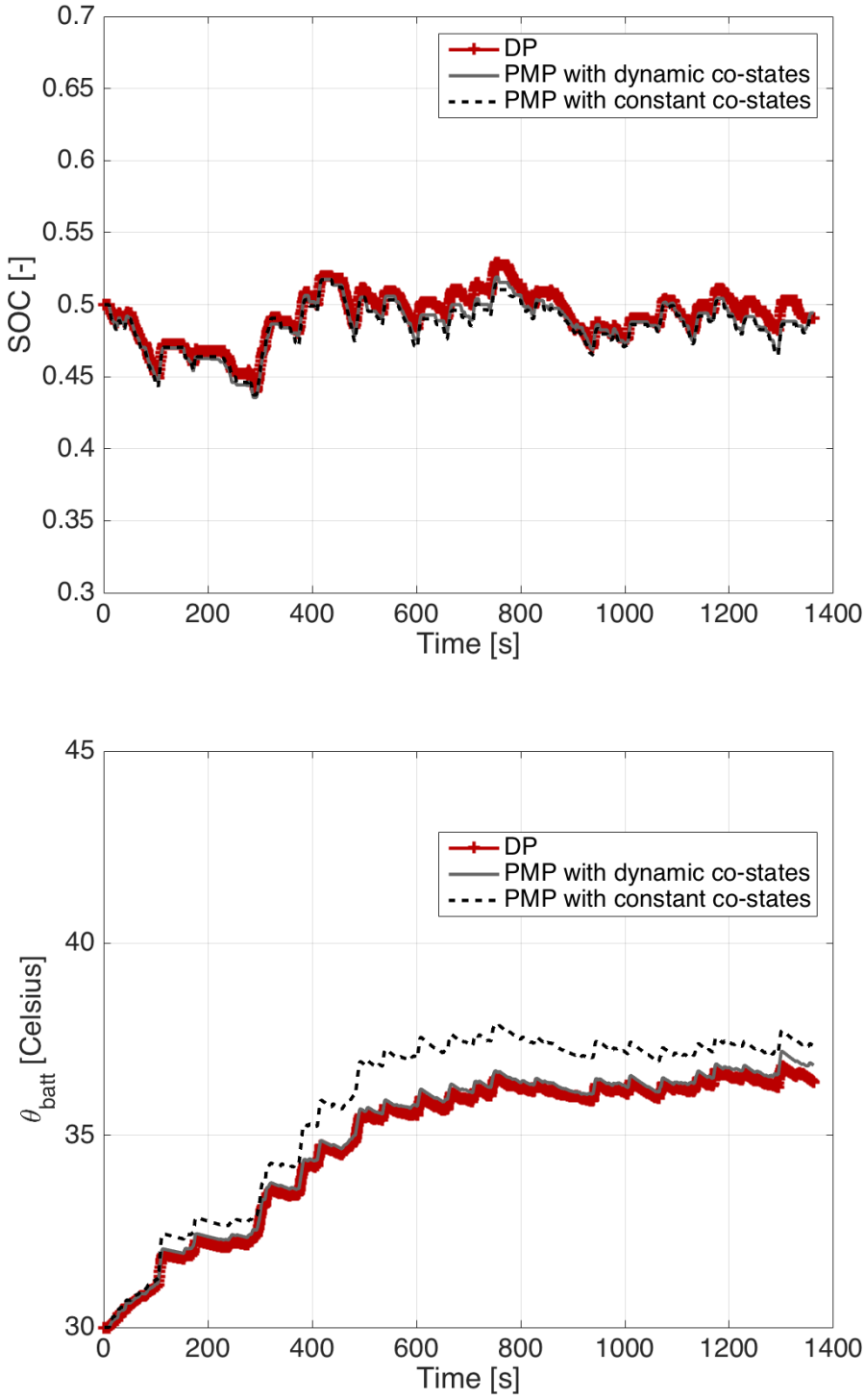

Figure 4.32: State trajectories from different controllers with $\alpha = 0.7$ over FUDS with ambient temperature at 30 °C

4.6 Comparison of sequential optimization and systematic optimization

In this section, two methods that solve the energy management problem for HEVs with consideration of battery capacity degradation are compared, namely sequential optimization and systematic optimization. With the sequential optimization, the CVT ratio is pre-optimized based on engine optimal operating line followed by optimal torque split, which is determined by solving an optimal control problem. On the other hand, in the systematic approach, optimal CVT ratio and torque split are obtained simultaneously by solving one optimal control problem. Generally speaking, the only difference between these two methods is that the transmission shifts maximize the efficiency of the engine in sequential optimization, while in systematic optimization, the transmission shifts to maximize the efficiency of the overall powertrain or the system efficiency. The solutions of both strategies presented in this section are solved by Dynamic Programming to make sure that they are comparable.

The Pareto front of US06 driving cycle is shown in Figure 4.33. It is clear that the shape of the two Pareto fronts are very similar, however, the Pareto front from systematic optimization is under the one from sequential optimization, which means that the performance of systematic optimization in terms of fuel economy is superior across the whole set of α. The performance measure of both methods are summarized and listed in Table 4.6. Looking into the data, the following observations can be made: with α decreasing, the differences of the two approaches in both fuel consumption and battery aging are decreasing. The reason is that when aging cost is more emphasized, electric machine is used less, thus the best engine efficiency is closer

to the best system efficiency, which drives the result from the sequential approach close to the result from the systematic approach. The range of Ah_{eff} from systematic optimization, which is between 0.1 and 67.1, is much wider than that from sequential optimization, which is between 0.2 and 36.8, which implies that when battery aging cost is not considered ($\alpha = 1$), the systematic approach can further exploit battery energy to save more fuel. When only fuel consumption is minimized ($\alpha = 1$), the fuel consumption from systematic optimization is 4.4% less than that from sequential optimization with almost doubled battery aging effects. It is clear that the use of battery energy is limited in the sequential method. This can be confirmed by Figure 4.34, which shows the battery energy throughput. At $\alpha = 1$, the total battery energy throughput from sequential method is approximately 0.63 kWh, while the number from systematic method is around 0.72 kWh. As α decreases, the total battery energy throughput declines in both methods and the number becomes similar. However, with similar battery energy throughput, the systematic optimization can always achieve better fuel economy, which means the amount of batter energy is used in a more efficient way.

In order to illustrate how transmission can improve the overall efficiency of the hybrid powertrain, simulation results with $\alpha = 0.4$ from both approaches are compared and analyzed in detail. The reason for choosing $\alpha = 0.4$ is that the aging cost from two approaches are very close to each other while the fuel consumption are different.

In Figure 4.35 (a), the SOC trajectories and battery temperature profiles are very close to each other, therefore similar aging effects are resulted. However, the CVT

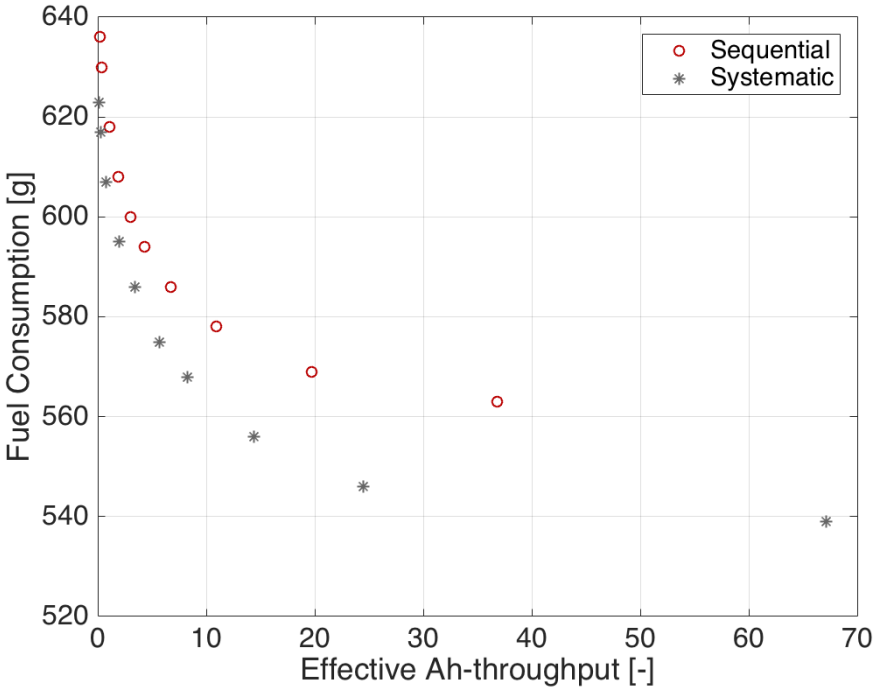

Figure 4.33: Pareto Front of US06

Table 4.6: Performance Measure of US06 for Two Approaches

	Sequential		Systematic	
α	Fuel [g]	Ah_{eff}	Fuel [g]	Ah_{eff}
1	563	36.8	539	67.1
0.9	569	19.7	546	24.5
0.8	578	10.9	556	14.4
0.7	586	6.7	568	8.3
0.6	594	4.3	575	5.7
0.5	600	3.0	586	3.4
0.4	608	1.9	595	2.0
0.3	618	1.1	607	0.8
0.2	630	0.4	617	0.3
0.1	636	0.2	623	0.1

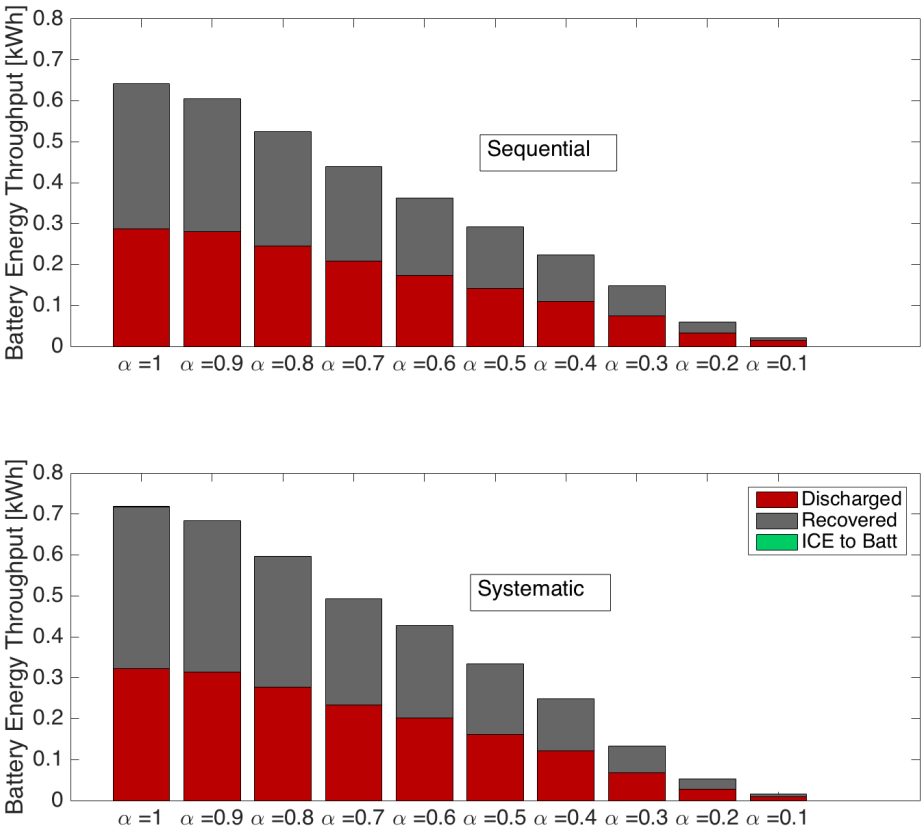

Figure 4.34: Battery Energy Throughput of US06

ratio r_{cvt} profiles are different from each other. Generally speaking, the CVT ratio from the systematic optimization is higher than that from the sequential optimization. For a given wheel speed, higher CVT ratio will result in higher crankshaft speed (4.13), which is as illustrated in Figure 4.35 (b). Theoretically, high engine speed corresponds to high fuel consumption, however, it is not necessarily true when a hybrid powertrain is in place. As indicated in Figure 4.36 (a), the sequential method puts the engine operating points very close to the OOL while the systematic method spreads

the engine operating points. The fuel consumption difference is not immediately obvious on the engine fuel map. The instantaneous fuel flow rate is shown in Figure 4.36(b), which indicates the fact that the systematic optimization consumes less fuel. Even though the engine does not operate on the minimum fuel consumption line, it is possible to lower the fuel consumption by requesting power assist from the electric machine. In fact, the electric machine is more efficiently operated in the systematic optimization. In Figure 4.37(a), in the systematic approach, the electric machine operating points spread out, which occupy better efficiency region compared with what from the sequential approach, which are relatively confined to low speed and high torque region. One of the consequences is that with lower electric machine efficiency, more electric energy is consumed when motoring and less electric energy is recovered when generating. Therefore the useful power from the electric machine is different even though the battery energy throughput is similar. Another consequence is that the regenerative braking power is constrained by the minimum torque limit of the electric machine at low speed, thus less energy is recovered, less energy is available for power assist and more fuel consumption. The behavior of electric machine can be understood from Figure 4.37(b), in which the electric machine power and torque are shown. When look at the regenerative torque, the electric machine torque from the sequential optimization is saturated at $-150N$, which leads to less regenerative power thus less recovered energy compared with the performance from the systematic optimization that has higher regenerative power. This is more influential in the case of $\alpha = 1$, when electric machine tries to recover energy as much as possible without considering battery aging.

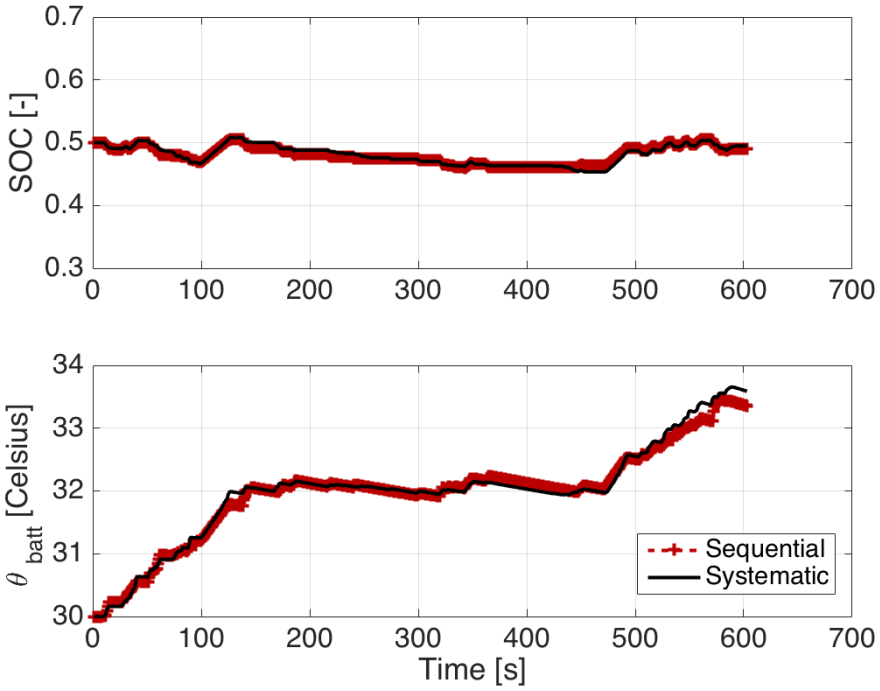

(a) State trajectories

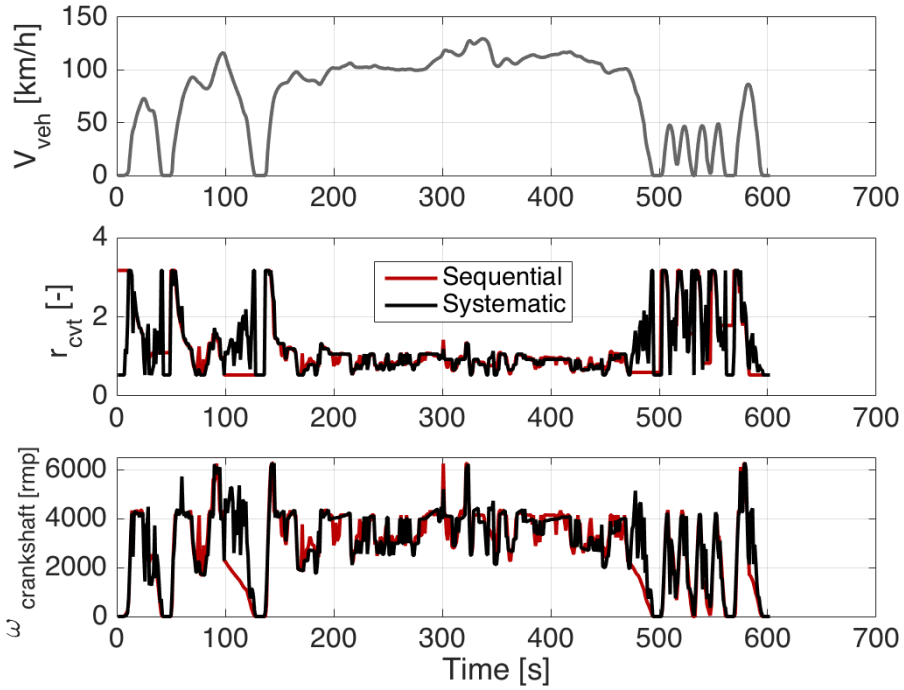

(b) CVT ratio

Figure 4.35: State trajectories and CVT ratio for US06 with $\alpha = 0.4$ at 30 °C

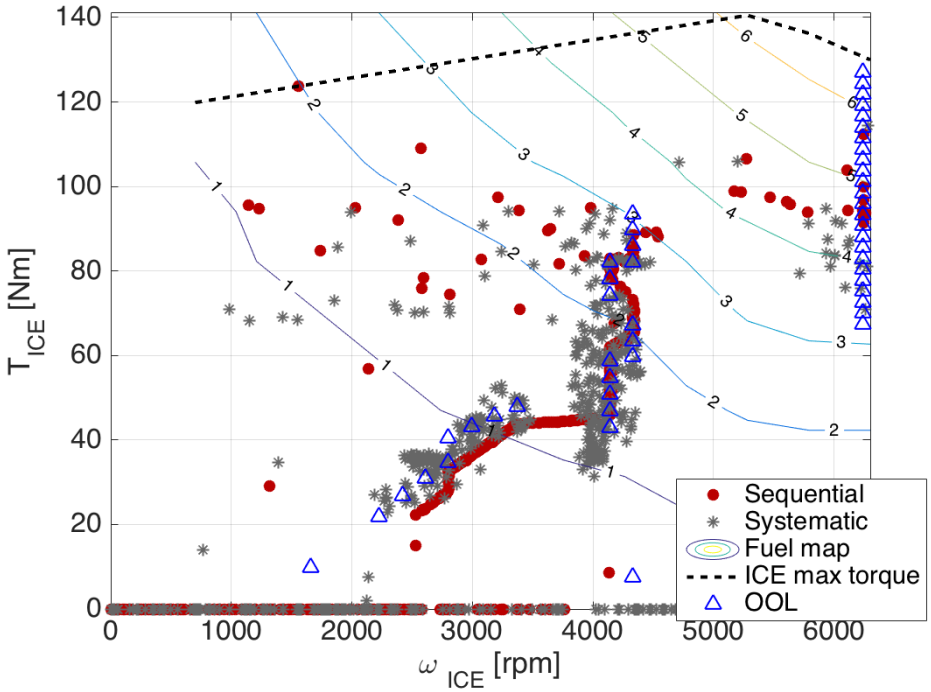

(a) Engine operating points on fuel map

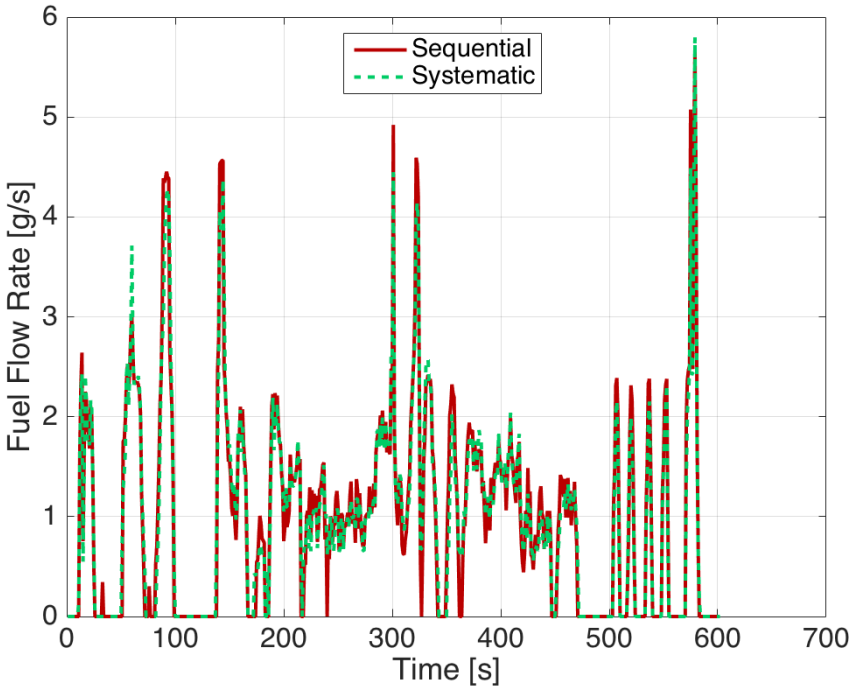

(b) Engine Fuel Flow Rate of US06

Figure 4.36: Engine Operating Conditions for US06 with $\alpha = 0.4$ at 30 °C

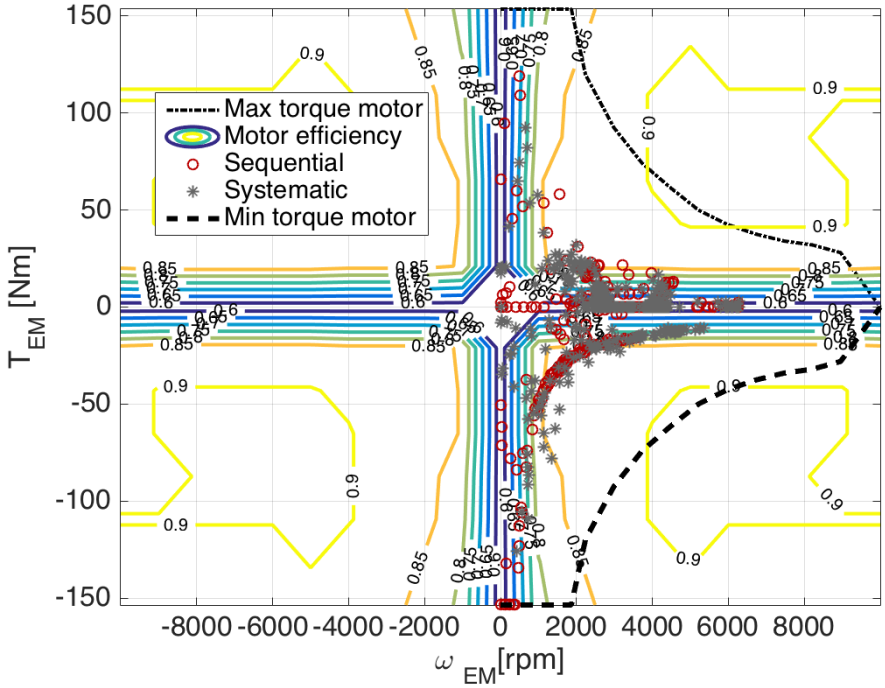

(a) Electric machine operating points

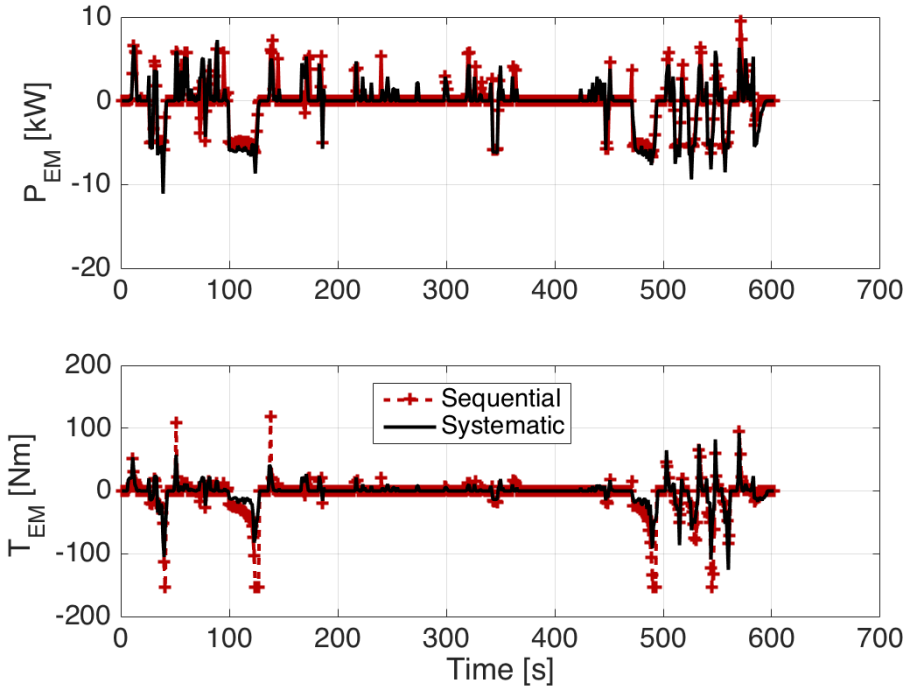

(b) Electric machine power and torque

Figure 4.37: Electric Machine Operating Conditions for US06 with $\alpha = 0.4$ at 30 °C

Similar comparison and analysis are conducted over FUDS as well, and the graphic results are included in appendix A. In general, the following conclusions can be made through the comparative study:

- A Pareto front exists for both sequential optimization and systematic optimization, and the shapes are similar;
- The performance of system optimal solution is superior than the sequential solution;
- A transmission shifting strategy that is optimized for the overall hybrid powertrain efficiency can further reduce both fuel consumption and battery aging effects.

4.7 Hybrid and electric vehicle charging optimization accounting for battery aging

This section presents an optimal control based charging strategy for plug-in hybrid electric vehicles and battery electric vehicles (BEVs). It has been shown by the previous section that both the performance and energy consumption of hybrid and electric vehicles are highly influenced by the health of the on-board energy storage systems. When compared with the time a vehicle spends in driving, the time a PHEV or BEV spends in charging occupies more of its lifetime. This work proposes a method to minimize battery capacity degradation incurred during charging by optimizing the charging current profile. A generic control-oriented vehicle cabin thermal model is developed to describe the battery surroundings taking into account solar radiation. Optimal control solution offered by Pontryagin's Minimum Principle (PMP) is presented and analysed. Simulation-based results show that the benefit of this strategy

in terms of decreasing battery aging is significant, when compared with the existing strategies, such as the widely accepted constant current constant voltage (CC-CV) protocol.

4.7.1 Background and literature

A common charging strategy, that will be used as a reference in this work is called constant-current/constant-voltage (CC-CV) charging. The charger limits the amount of current to a pre-set level until the battery reaches a pre-set voltage level. The current then reduces as the battery becomes fully charged. This strategy allows fast charging without the risk of over-charging. Overvoltage or excessive charging current begins to break down Li-ion cells, reducing overall battery life or even resulting in catastrophic failures. This charge strategy can effectively increase the battery-charge speed, avoid overcharge, and achieve an almost 100% full battery charge. The charging time with CC-CV is dependent on the charging current in the CC mode. In general, the commercial charging equipment is commonly categorized into one of three types described below:

- AC level 1 charging provides charging through a 120V, alternating-current (AC) plug and requires a dedicated circuit. Generally speaking, Level 1 charging refers to the use of a standard household outlet.

- AC level 2 charging offers charging through a 240V, up to 80A, 19.2KW AC plug and requires installation of home charging or public charging equipment.

- DC fast charging charges through a 480V DC plug. Most DC fast chargers provide an 80% charge in 30 minutes or less.

The CC-CV strategy is well developed and widely adopted because of its simplicity and easy implementation.[135]. Moreover, it can be used with every kind of battery. However, the charge speed of the CC-CV strategy is still too slow to satisfy the users' requirement, which is mainly due to the time-consuming CV phase. If one tries to shorten the charging time by increasing the current rate in CC phase, the efficiency drops and the battery ages faster as well. Therefore, innovative charging strategies are necessary.

The literature has examined xEV charging patterns from a number of different perspectives. In [30], a pulse-current based CC-CV approach is presented. The main idea is to reduce the charging time and improve efficiency using a pulse current protocol during the CV mode. A similar approach is proposed in [78], which reduces the charging time using a multi-current protocol based on battery internal resistance during the CV mode. Instead of modifying the CV phase, a built-in resistance compensator technique is presented in [83] to increase the period of the CC phase, which reduces the charging time by smoothing the CC-CV transmission by estimating the battery open circuit voltage (OCV). Multi-stage constant current charging strategy has been studied in [87, 63, 86, 41]. The main idea is to find an optimal set of decreasing current that minimizes the charging time and maximize the charged capacity. The pulse charger has been claimed to be a fast and efficient charging algorithm for lithium-ion batteries, because pulse charging strategy is designed to establish the link

between charging current profile and the chemical reaction process so that electrochemical reactions neither produce heat nor cause the accumulation of pressure inside the battery [79, 28, 29].

Significant research has been conducted on optimal PHEV charging and power management. An optimal control problem is formulated to minimize the charging time while not excessively aging the cell, in which battery life is treated as a constraint and which is solved by nonlinear model predictive control (NMPC) [75]. In [62], the authors optimally tradeoff charging time and energy loss during charging by designing a weighted objective function, and the problem is solved by nonlinear programming (NLP). To account for electricity cost, [61] optimizes the charging power to minimize a combined cost of electricity and battery aging. The optimization is solved using the Matlab® build-in constrained function $fmincon$. With the assumption that next-day energy needs are known, as-needed charging strategy is proposed in [60] to minimize battery degradation by minimizing time spent at high state-of-charge. In [13], the authors present a charging strategy for PHEVs using genetic algorithm, which takes into account the combined effects of total energy cost, battery health, electricity pricing, and PHEV driving patterns. In [112], the authors study the tradeoffs and synergies between optimal charging and power management in minimizing the overall CO_2 emissions, and the optimal control problem is solved by dynamic programming (DP).

One common limitation of the approaches reviewed here is that they all assume constant ambient temperature without considering seasonal and regional climate effects, which are actually highly influential on battery aging behaviour during charging. The work presented in this paper is a significant extension of [142]. The main contribution of this work is that an optimal charging algorithm is developed, which aims to minimize battery capacity degradation for any given time window taking into account the environmental conditions. Combining the battery aging model and the battery thermal model, an optimal charging current profile is determined by solving an optimal control problem with Pontryagin's minimum principle (PMP). An experimentally calibrated semi-empirical battery capacity degradation model is directly linked to the control strategy. A generic vehicle cabin thermal model is developed and applied for designing the optimal charging strategy, which takes into account not only the ambient temperature but also the solar radiation. This paper is organized in the following way: in section 3, all the models are described including battery electric model, battery heat generation model, battery aging model as well as the vehicle cabin and battery thermal model. In section 3, optimal control problem formulation is presented. In section 4, the optimal solutions from PMP are studied; simulation results for various charging scenarios are analyzed; and comparisons between optimal charging and CC-CV protocol are conducted. Conclusions are made in the last section.

4.7.2 Optimal control problem formulation with PMP

The objective of the optimal control problem is to minimize battery capacity degradation incurred during charging for xEVs, therefore the concept of battery

severity factor and effective Ah-throughput are applicable here as well.The states of interest are battery state of charge $x_1 = SOC$ and battery temperature $x_2 = \theta_{batt}$. The corresponding dynamics are described by equation (3.18) and (3.26) respectively. Charging current is chosen as control input $u = I_{cell}$ and the surrounding temperature is measured disturbance. The aim of the optimal charger is to increase battery SOC from a low initial value to a desired final value in a specified amount of time while minimizing the effective Ah-throughput with considerations of ambient conditions. Thus the optimal control problem takes the following mathematical form:

$$\min : J = \int_0^{t_f} \sigma(x_1(t), x_2(t), u(t)) \cdot |u(t)| dt$$

subject to

$$\begin{aligned}
\dot{x}_1 &= -\frac{u(t)}{3600 \cdot Q_{cell}} \\
\dot{x}_2 &= \frac{R_0 \cdot N_s \cdot N_p}{M_{batt}} \cdot u^2(t) + \frac{1}{K_{bc} \cdot M_{batt}}(\theta_{cab} - x_2) \\
&\quad + \frac{1}{K_{ab} \cdot M_{batt}}(\theta_{amb} - x_2) \\
&\quad + \frac{U}{M_{batt}} \cdot (\theta_{cool} - x_2) \\
x_1(0) &= x_{1_0} \\
x_1(t_f) &= x_{1_{t_f}} \\
x_2(0) &= x_{2_0} \\
x(t) &\in \chi \\
u(t) &\in \mathcal{U}
\end{aligned} \tag{4.33}$$

where χ and $\mathcal{U}$ are defined as the admissible state and control sets respectively. Among methods for solving optimal control problems, Pontryagin's Minimum Principle is chosen to give numerical solution. According to PMP, minimizing the cost function in (4.33) is equivalent to minimizing the Hamiltonian:

$$\begin{aligned}\mathscr{H}(x_1(t), x_2(t), u(t), t) =& \sigma(x_1(t), x_2(t), u(t)) \cdot |u(t)| \\ &+ \lambda_1(t) \cdot \dot{x}_1(t) + \lambda_2(t) \cdot \dot{x}_2(t)\end{aligned} \tag{4.34}$$

where $\lambda_i(t)$, $i = 1, 2$, are the co-states which evolve with the dynamics described by

$$\dot{\lambda}_i(t) = -\frac{\partial \mathscr{H}(x_1, x_2, u, t)}{\partial x_i} \tag{4.35}$$

Since the final value of $x_2(T)$ is not specified, the additional necessary condition for optimal solution is

$$\lambda_2(t_f) = 0 \tag{4.36}$$

The optimal control trajectory is given by

$$u^*(t) = \arg\min_{u \in \mathcal{U}} \mathscr{H}(x_1^*(t), x_2^*(t), u(t), \lambda_1^*(t), \lambda_2^*(t), t) \tag{4.37}$$

Initial valuea of co-state $\lambda_i(0)$ can be determined by shooting method, if and only if a priori knowledge of the future weather conditions are available [74].

4.7.3 Simulation results

The battery pack considered has the size of approximately 5 kWh and 15 Ah, which represents the size of a battery pack in PHEVs. Simulation results are divided into two groups: level 2 charging and fast charging. In the case of level 2 charging, time window of 3 hours is tested, which is enough to get the battery pack fully charged. For fast charging, charging in 10 minutes, 30 minutes are considered. In all cases, the initial and final battery SOC are 0.2 and 0.95 respectively.

AC level 2 charging

In order to show the effects that the ambient conditions have on battery aging and the effectiveness of the optimal charging strategy on saving battery life during charging, Phoenix is selected to represent an environment capable of rapidly degrading battery health due to its extreme weather represented by high ambient temperature and strong solar radiance. The hourly weather condition in one day of July is shown in Fig.3.14, which leads to the vehicle cabin temperature profile shown in Fig. 3.15 with the assumption that the vehicle cabin temperature reaches steady state that equals to the ambient temperature at 5 am. The vehicle cabin temperature is treated as a measured input when solving the optimal control problem. The reason is that the battery thermal condition has insignificant influence on the vehicle cabin temperature when compared with that of ambient conditions. In addition, if the vehicle cabin temperature would be a state, the optimal control problem was difficult if not impossible to solve with three states and three co-states.

The simulation scenario is that after a trip, the vehicle sits in the parking lot between 9 am and 5 pm, which is the typical situation for a working day. The vehicle is plugged in at 9 am, with the initial battery temperature of $\theta_{batt}(0) = 40°\text{C}$. The battery is air cooled and the coolant temperature is equal to the ambient temperature. For level 2 charging, the common power rates are 3.3kW and 6.6kW, and therefore these values are used in CC-CV strategy. In the optimal charging strategy, the power limit is set to be 6.6kW, which makes it comparable to CC-CV strategy.

Simulation results are presented in Fig. 4.38 and Fig. 4.39. It is evident that , among three cases, PMP-based optimal strategy gives the lowest battery temperature profile. In fact, the optimal charging power is dominated by battery temperature: the controller chooses to wait at the beginning when the temperature is high; the charging power reaches the peak when the temperature drops to the lowest point, which happens a little after 10 am; then the power becomes smaller when battery temperature starts to climb. As the controller knows the future ambient conditions, it is able to recognize the best timing to trigger charging so that high temperature can be avoided. If one take a look at the battery severity factor (Fig. 4.39), the optimal strategy is able to achieve less aging effect that comes with lower C-rate and lower temperature. The summary of level 2 charging is listed in Table 4.7. The root mean square value of C-rate, severity factor and battery temperature gives the average performance of each case. PMP-based strategy is superior in every aspect when compared with CC-CV strategy. The effective battery life depletion characterized by Ah_{eff} shows that the optimal aging-aware charging strategy can potentially reduce capacity degradation by up to 20.7 % with respect to CC-CV strategies.

Table 4.7: Summary of Level 2 Charging

	CC-CV 3.3kW	CC-CV 6.6kW	PMP
Ah_{eff}	29.1	33.8	26.8
C-rate rms	0.38	0.52	0.29
σ rms	2.9	3.1	2.6
θ_{batt} rms	38.9	39.7	38.7

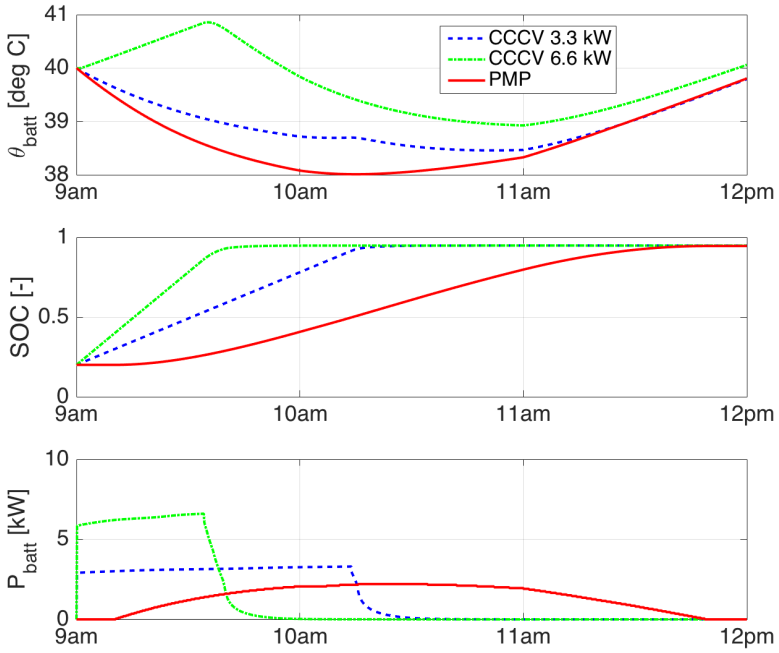

Figure 4.38: Level 2 Charging Battery Temperature and SOC

Fast charging

DC fast chargers is going to supersede AC level 1 and AC level 2 charging stations, and are designed to charge xEVs quickly with an electric output ranging between 50 kW 120 kW. Tesla decided to move forward with its own standard, the Supercharger, which has provided 120 kW of power since its launch. Most xEVs can be equipped with DC fast charge capability, and there are currently nearly 2,200 high-speed chargers in the United States capable of adding significant range to an EV in not much longer than the time it takes to fill the gas tank. According to the SAE charging configurations and ratings terminology defined in SAE J1772^{TM}, there are multiple DC fast charging ratings: level 1 with 200-450V, up to 36kW and 80A; level 2 with

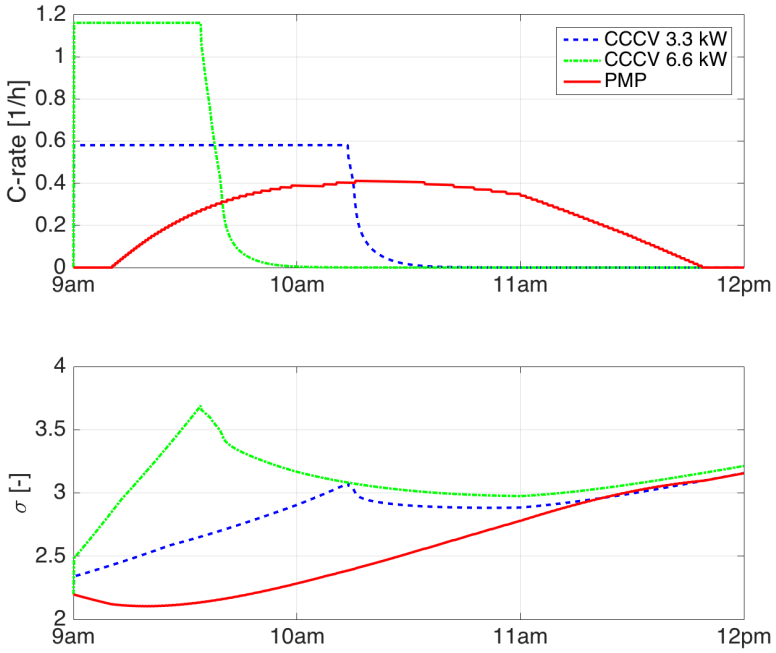

Figure 4.39: Level 2 Charging Battery Severity and C rate

200-450V, up to 90kW and 200A; level 3, which is still to be determined, with proposed power up to 240kW and 400A. In this work, DC level 1 and level 2 protocols are simulated to compare with the optimal charging strategy in 30-minute fast charging and 10-minute fast charging.

The same initial value of battery temperature is used as what in AC level 2 charging, which is equal to 40°C. Since the duration is short for fast charging, both of the ambient temperature and the temperature of the surroundings are kept as constant, which is 25°C. Simulation results for 30 minutes and 10 minutes are shown in Fig. 4.40 and Fig. 4.41 respectively. The current limit of 80A is applied for both

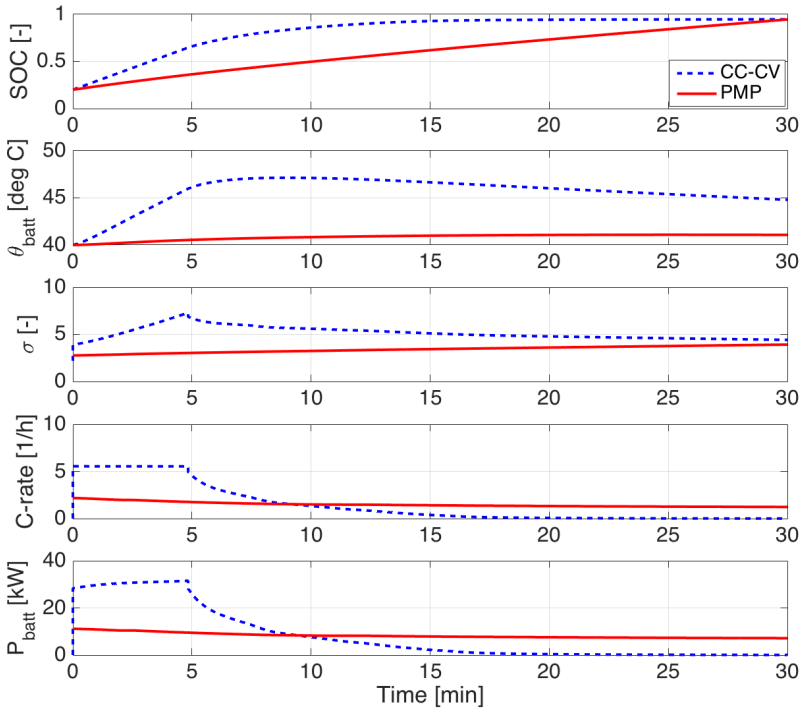

Figure 4.40: Fast Charging in 30 minutes

strategies in the case of 30-minute, while 200A is applied in the case of 10-minute. As shown by both cases, the optimal controller is able to keep the battery temperature much lower than that from CC-CV strategy, which leads to smaller severity factor σ. The summary of fast charging is listed in Table 4.8. It is clear that the value of the aging-related parameters resulted from PMP-based optimal charging strategy is significantly lower than that from the CC-CV strategy. Based on the effective Ah-throughput, the optimal strategy achieve 39.9% less capacity degradation in the case of 30-minute charging and 31.4% less in the case of 10-minute charging.

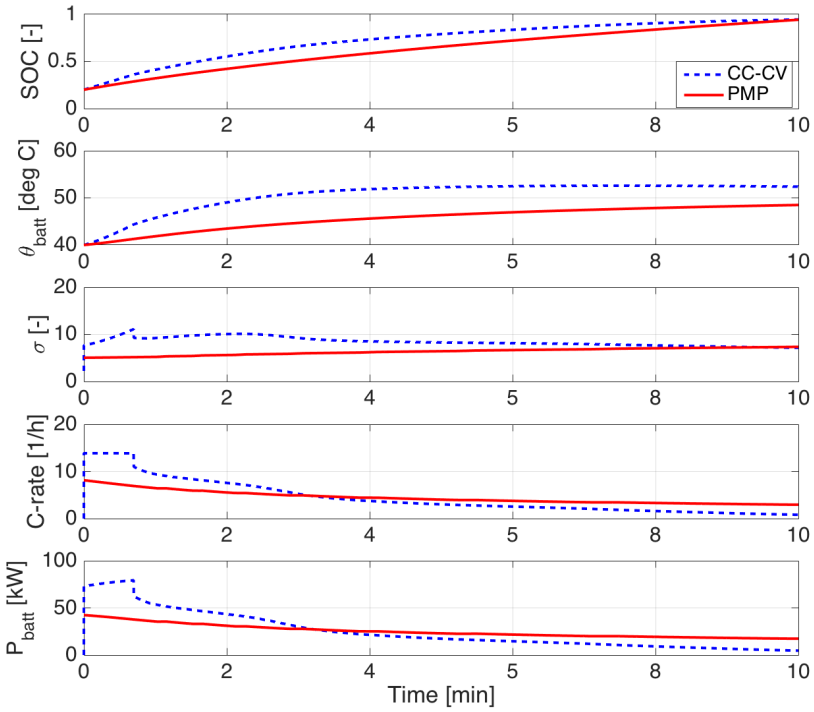

Figure 4.41: Fast Charging in 10 minutes

Table 4.8: Summary of Fast Charging

	30 Min		10 Min	
	CC-CV 80A	PMP	CC-CV 200A	PMP
Ah_{eff}	60.6	36.4	97.1	66.6
C-rate rms	2.52	1.51	5.83	4.68
σ rms	5.2	3.4	8.5	6.4
θ_{batt} rms	45.7	40.9	50.7	45.7
θ_{batt} max	47.1	41.1	52.6	48.5

Conclusion

In this section, an optimal control based aging-aware charging strategy for xEVs is proposed and solved by PMP. Simulation based results show that the optimal charging strategy is capable to save battery capacity loss and extend battery life by reducing the severity factor, when compared with the widely accepted CC-CV protocol. One of the essential observations is that the charging event is primarily dominated by battery temperature, which demonstrates the importance of including consideration of ambient conditions. With the help of a vehicle cabin thermal model and the weather forecast, it is realistic to predict the surrounding conditions of the battery pack, which enables the real-time implementation of the optimal charging algorithm.

4.8 Summary

In this chapter, a complete set of optimal control problems related to xEVs with consideration of battery aging are studied, which includes energy management strategies for hybrid electric vehicles and battery charging strategy for plug-in hybrid and

electric vehicles. The presented energy management strategies for hybrid electric vehicles can be equally applied for plug-in hybrid vehicles in charge-sustaining mode. Different optimal control theories are applied to solve the proposed problems, and the solutions show that battery life can be significantly extended with small extra cost on fuel consumption by an appropriately designed control algorithm.

Chapter 5: Real-time Energy Management Strategy for HEVs with Consideration of Battery Aging

Learning from the results of Chapter 4, we know that there is a fundamental trade-off between fuel economy and battery capacity degradation; however, it is realistic to expect dramatic savings on battery life with a small penalty in fuel consumption. So far, the optimal energy management strategy has been solved by DP and PMP, neither of which are causal, which means the entire cycle or future driving conditions must known a priori. In the literature [102, 131], it has been shown that Adaptive Equivalent Consumption Minimization Strategy (A-ECMS) is a real-time implementable strategy, which works well for the fuel optimal scenario. In this chapter, we propose a control strategy inspired by A-ECMS, which accounts for battery capacity degradation.

To reduce battery aging effects, a cost is assigned to battery use based on the operating conditions. The concept of battery severity factor σ is used to quantify the battery aging effect or cost based on the present conditions. Thus the battery output will be reduced when conditions could results in accelerated aging effects, which is characterized by σ. The control diagram of Figure 5.1 is proposed.

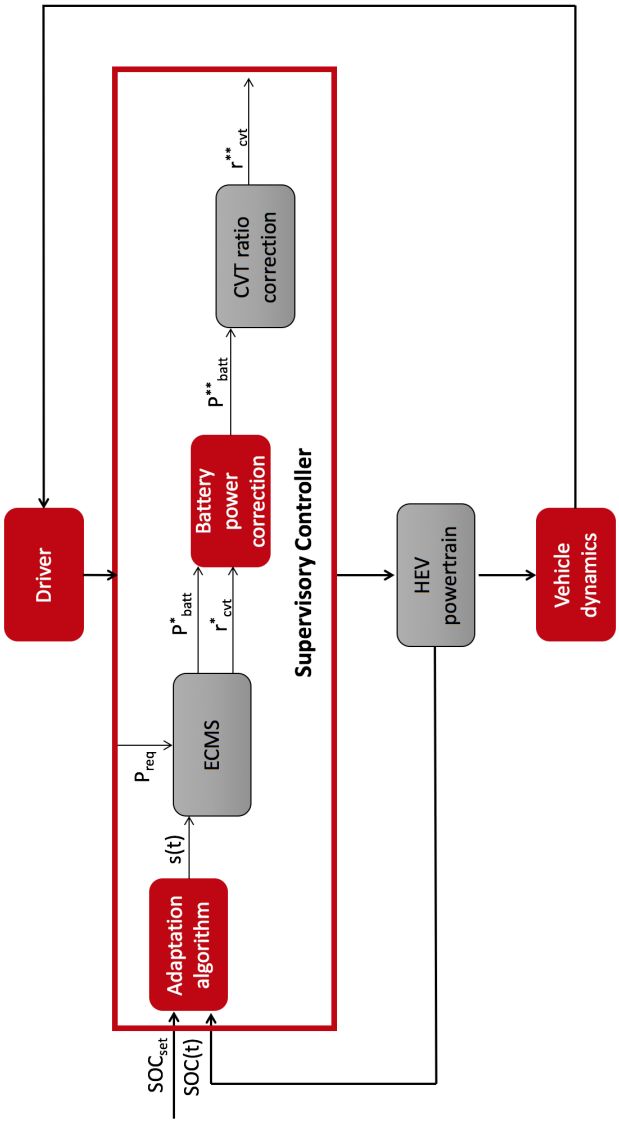

Figure 5.1: Control Diagram of A-ECMS Accounting for Battery Aging

Each block inside the supervisory controller is described in detail in the following sections.

5.1 Adaptive equivalent consumption minimization strategy

In [130, 131, 129], Serrao et al. established the equivalence between ECMS and PMP showing that the equivalence factor, s, is related to the co-state in the PMP solution. Thus only one parameter must be adapted for online optimization, e.g., the co-state λ, which is shown to be related to the equivalence factor in ECMS. The mechanism used to perform the parameter adaptation in this dissertation is adaptation based exclusively on feedback from SOC, as the vehicle being studied is a charge-sustaining HEV. The idea is to change dynamically the value of the equivalence factor at present time by contrasting the SOC deviation from the reference value. In this section, the adaptive ECMS is briefly reviewed before delving into the battery aging aspect of the problem.

5.1.1 ECMS formulation

The original ECMS formulation is introduced in Section 2.1.4. The essence of ECMS is that in a charge-sustaining HEV, the energy change in the battery pack at the end of one trip is negligible, which means almost all of the energy is ultimately from the fuel. Thus the battery energy usage is converted to an equivalent amount of fuel and added to the real fuel consumption, thus defining an equivalent fuel consumption, which is minimized instantaneously [130].

$$\dot{m}_{f,eqv}(t) = \dot{m}_f(t) + \dot{m}_{ress}(t)$$

Following the same idea, the instantaneous cost to be minimized is

$$\dot{m}_{f,eqv}(t) = \dot{m}_f(t) + s^*(t) \cdot \frac{I_{cell}(t)}{3600 \cdot Q_{cell}} \tag{5.1}$$

where $\dot{m}_f(t)$ is the fuel flow rate, $s^*(t)$ is the equivalence factor in units of grams (of fuel), $I_{cell}(t)$ is battery cell current, Q_{cell} is cell capacity in Ah. If one compares (5.1) with the original ECMS formulation in (2.15-2.17), the following equation can be derived:

$$s^*(t) = \frac{s(t) \cdot V_{oc} \cdot N_s \cdot N_p \cdot Q_{cell} \cdot 3600}{LHV} \tag{5.2}$$

where V_{oc} is the battery cell open circuit voltage, LHV is the gasoline lower heating value, N_s and N_p are the battery cell number in series and parallel respectively.

5.1.2 Adaptation based on feedback from SOC

The online adaptation of equivalence factor uses the difference between the present SOC value and the target value. One adaptation law based on a proportional-integral (PI) controller was proposed in [69], in which the equivalence factor continuously changes with:

$$s^*(t) = s_0^* + k_p(SOC_0 - SOC(t)) + k_I \int_0^t (SOC_0 - SOC(\tau)d\tau \tag{5.3}$$

where s_0^* is the initial value of s^*, and k_p and k_I are the proportional and integral gains of the adaptation law. The choice of s_0^* can be made by averaging different optimal initial values obtained offline. This continuous adaptation law may prevent the use of battery energy when tracking a constant target value of SOC, which results

in not fully exploiting the benefit of hybridization.

To allow the battery SOC to span a wider range, a discrete-time adaptation law was proposed in [102]:

$$s^*(k+1) = \frac{s^*(k-1) + s^*(k)}{2} + k_p \cdot (SOC_0 - SOC(t)), t = k \cdot T, k = 1, 2, \ldots \quad (5.4)$$

where $s^*(k+1)$ represents the new value of equivalence factor, which will be applied in time window $t \in [kT, (k+1)T]$, while $s^*(k-1)$ and $s^*(k)$ are the equivalence factor corresponding to the previous two time intervals. k_p is the proportional gain of the feedback controller and T is the duration of one interval. Both k_p and T are tuning parameters for the strategy.

5.1.3 Calibration of adaptive strategies

In order to study the effects of the gain k_p and of the adaptation interval T on the performance of the strategy, simulation results are compared and summarized. In Figure 5.2 and Figure 5.3, the results obtained from five consecutive US06 cycles are shown, in which three different values of k_p are studied, while the duration is fixed $T = 60s$. The shape of SOC trajectories are generally the same with minor differences. A similar observation can be made on the equivalence factor profiles (Figure 5.3), which is that the overall shapes are the same, and that as k_p increases, the SOC profile has larger fluctuations. In Figure 5.4 and Figure 5.5, results with different adaptation intervals are shown, and the proportional gain is chosen to be $k_p = 8$. Figure 5.5 shows that the equivalence factor trajectories are different, leading

to different SOC profiles. In general, the smaller the adaptation interval is, the more dynamic the equivalence factor behavior is. Ideally, if T equals to the entire driving time, s^* would be the optimal constant equivalence factor for that driving cycle. The effect of the calibration parameters on US06 is summarized in Table 5.1, in which $\frac{m_f}{m_f^*}$ represents the fuel consumption normalized by optimal fuel consumption from DP. The Table shows that the A-ECMS is withing 1% of the DP results for this cycle, confirming that this sup-optimal algorithm is an excellent choice. The same analysis is conducted over five consecutive FUDS and the results are shown in Appendix B. Based on the simulation results from the two driving cycles, $T = 60s$ and $k_p = 8$ are selected for the rest of the studies.

Table 5.1: Effect of Calibration Parameters

k_p	6	8	10
T [s]	$\frac{m_f}{m_f^*}$	$\frac{m_f}{m_f^*}$	$\frac{m_f}{m_f^*}$
30	1.008	1.012	1.012
60	1.008	1.008	1.010
120	1.007	1.009	1.008

Theoretically, SOC boundary conditions should be enforced by the adaptation, however, if the adaptation interval T is long enough, SOC can touch the boundary or even break the constraints. To prevent this situation, a penalty function can be applied, which is used to guarantee that the SOC does not exceed the admissible limits (4.8). As one example, the penalty function can take the form in (5.5). The allowable SOC range is between 0.3 and 0.7, thus the penalty function takes the shape shown in Figure 5.6.

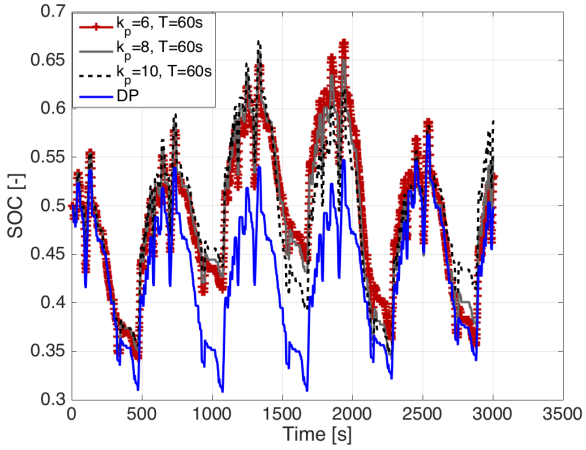

(a) SOC Trajectories

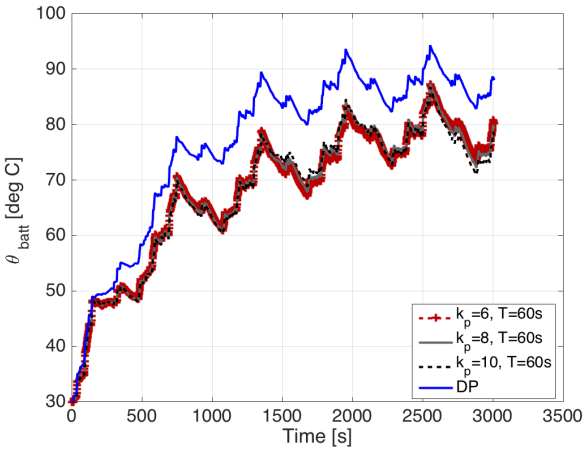

(b) Battery Temperature Trajectories

Figure 5.2: Results obtained from five US06 cycles with different k_p

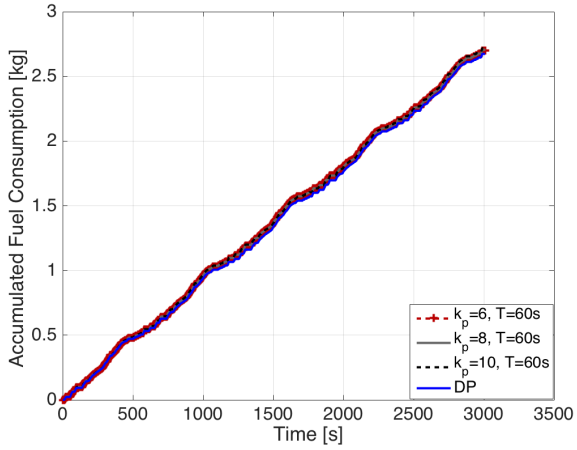

(a) Accumulated Fuel

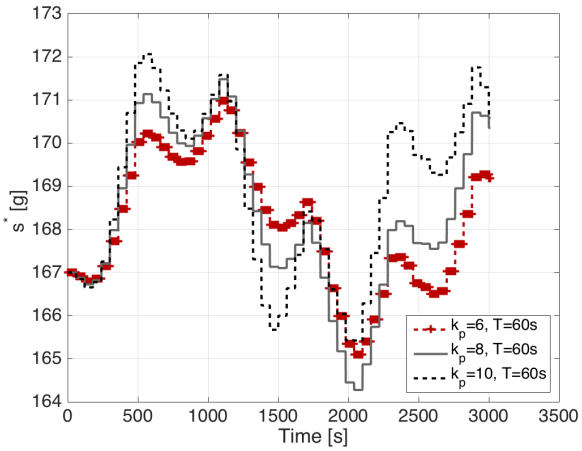

(b) s^* Trajectories

Figure 5.3: Results obtained from five US06 cycles with different k_p

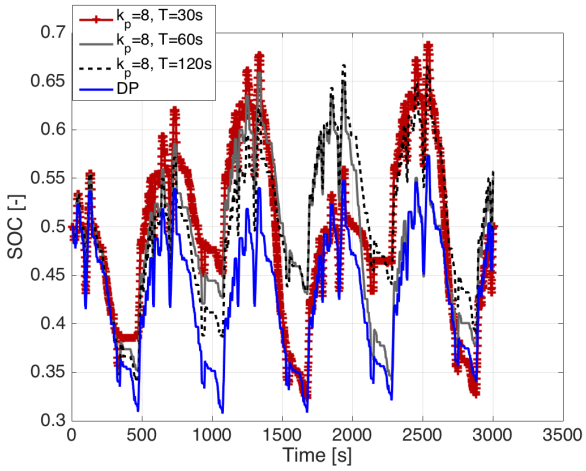

(a) SOC Trajectories

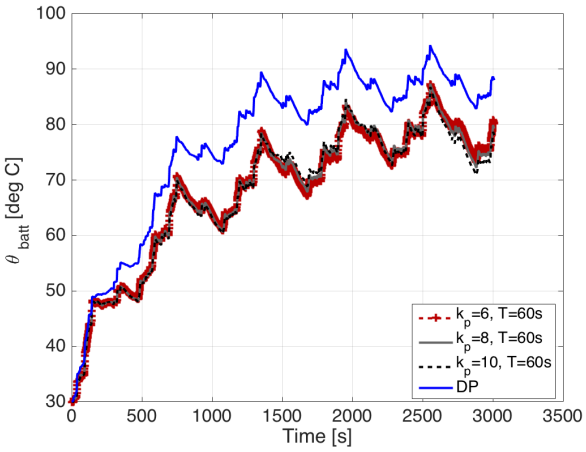

(b) Battery Temperature Trajectories

Figure 5.4: Results obtained from five US06 cycles with different T

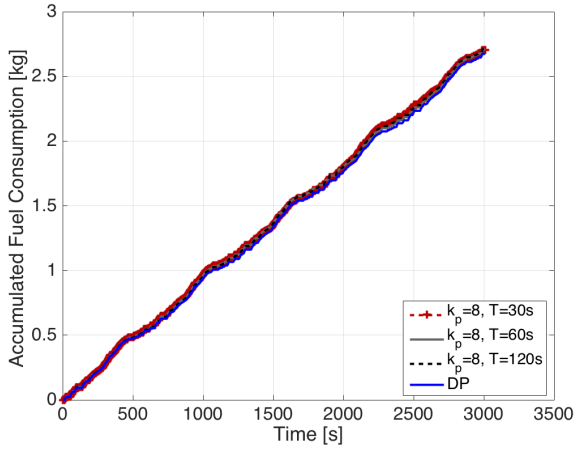

(a) Accumulated Fuel

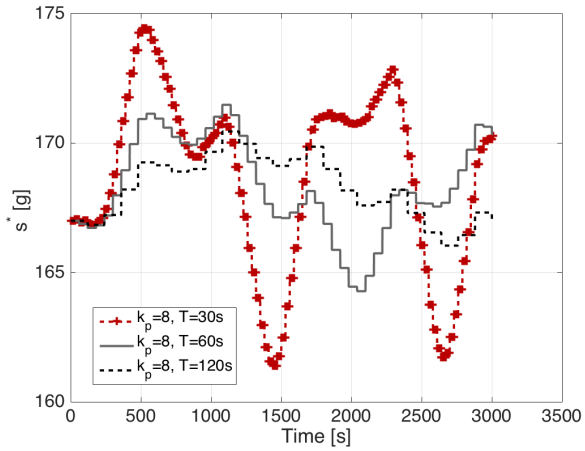

(b) s_{eqv} Trajectories

Figure 5.5: Results obtained from five US06 cycles with different T

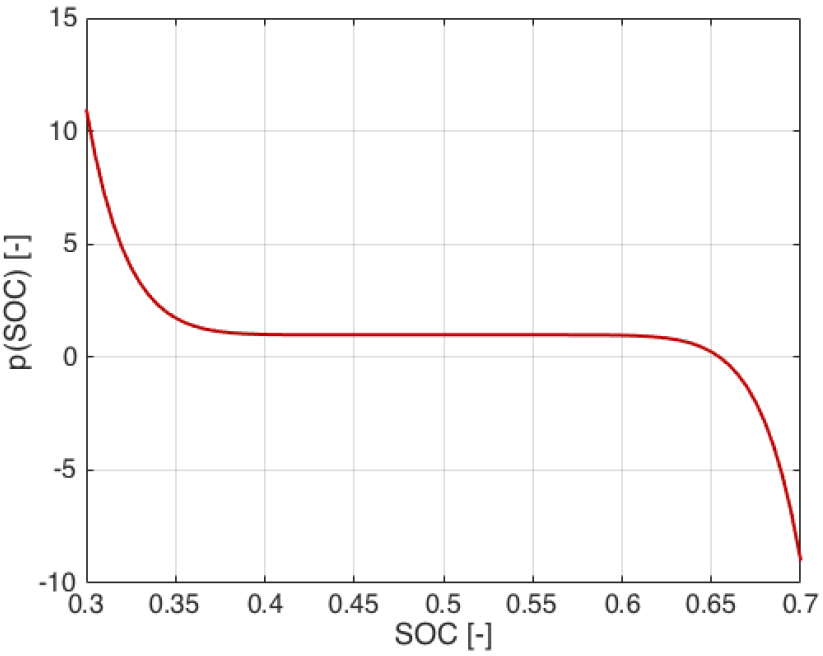

Figure 5.6: SOC Penalty Function

$$p(SOC) = 1 - (\frac{SOC(t) - SOC_0}{(SOC_{max} - SOC_{min})/2})^9 \tag{5.5}$$

5.2 Aging-severity-based battery power correction

The most important conclusion from all the optimal solutions, regardless of sequential or systematic approaches, is that there exists a fundamental tradeoff between fuel economy and battery capacity degradation, and that it is possible to reduce battery capacity loss with a small sacrifice in fuel economy. The idea is to correct battery power output if a sever aging condition is recognized, and to otherwise follow the command issued by the A-ECMS controller, which is nearly fuel-optimal.

Let σ^* be the battery severity factor that results when the commands from A-ECMS controller are followed, and let $\bar{\sigma}$ be the severity factor threshold that defines accelerated aging condition. Then battery power should be reduced any time when $\sigma^* > \bar{\sigma}$ to limit aging acceleration. The proposed correction law is:

$$|P_{batt}^{**}| = |P_{batt}^{*}| \cdot (1 - w \cdot \ln \frac{\sigma^*}{\bar{\sigma}}) \tag{5.6}$$

where P_{batt}^{**} is the battery power after correction, P_{batt}^{*} is the battery power corresponding to σ^*, which is the command from A-ECMS controller, and w is a calibration parameter to be determined. The reasoning behind the correction law is based on the definition of severity factor (4.3-4.5):

$$\begin{aligned} \frac{\sigma^*}{\bar{\sigma}} &= \exp(\frac{163.3 \cdot (I_c^* - \bar{I}_c)}{0.57 \cdot R \cdot \theta_{batt}}) \\ &= \exp(\frac{163.3 \cdot (|P_{batt}^{*}| - |\bar{P}_{batt}|)}{0.57 \cdot R \cdot \theta_{batt} \cdot V_{oc} \cdot N_s \cdot N_p \cdot Q_{cell}}) \end{aligned} \tag{5.7}$$

where I_c^* and $\bar{I}_c$ are the C-rate corresponding to σ^* and $\bar{\sigma}$, and R is the gas constant. Therefore the following expression can be derived:

$$\begin{aligned} |\bar{P}_{batt}| &= |P_{batt}^{*}| - \frac{0.57 \cdot R \cdot \theta_{batt} \cdot V_{oc} \cdot N_s \cdot N_p \cdot Q_{cell}}{163.3} \cdot \ln \frac{\sigma^*}{\bar{\sigma}} \\ &= |P_{batt}^{*}| \cdot (1 - \frac{0.57 \cdot R \cdot \theta_{batt} \cdot V_{oc} \cdot N_s \cdot N_p \cdot Q_{cell}}{163.3 \cdot |P_{batt}^{*}|} \cdot \ln \frac{\sigma^*}{\bar{\sigma}}) \end{aligned} \tag{5.8}$$

Comparing (5.8) with (5.6), one can conclude that

$$|P_{batt}^{**}| = |\bar{P}_{batt}| \tag{5.9}$$

if

$$w = \frac{0.57 \cdot R \cdot \theta_{batt} \cdot V_{oc} \cdot N_s \cdot N_p \cdot Q_{cell}}{163.3 \cdot |P_{batt}^{*}|} \tag{5.10}$$

However, if the above equations were applied, the battery severity factor, during one trip, would be either below $\bar{\sigma}$ or exactly equal to $\bar{\sigma}$, which is not the desired behavior. The severity factor should be allowed to oscillate to have flexible battery operation to permit good drive quality, for example. Since driving conditions, and therefore the severity factor, change dynamically, the values of $\bar{\sigma}$ should not be an instantaneous value, but could, for example, be the root mean square (RMS) value σ during a driving cycle. It is shown later that $\bar{\sigma}$ can be interpreted as a calibration parameter.

At this point, it is very instructive to analyze the systematic optimization results obtained from DP with four different driving cycles and four values of α at three ambient temperatures. The RMS value of severity factor σ_{rms} and root mean square value of battery power $P_{batt,rms}$ are visualized in Figure 5.7. In Figure 5.7 (a), the data is grouped by ambient temperature and α, while the same data in (b) is grouped by ambient temperature and driving cycle. A trend can be observed between σ_{rms} and $P_{batt,rms}$ when looking at data obtained at the same ambient temperature regardless of α values and driving cycles. The equation in (5.6) is used to fit the data with the assumption that σ^* equals to the biggest σ_{rms} at each ambient temperature, and P^*_{batt} equals to the $P_{batt,rms}$ corresponding to the biggest σ_{rms}, thus the curve fitting result is shown in Figure 5.8, and the value of w is listed in Table 5.2. To have a general expression of w as a function of ambient temperature, an exponential function is used to fit the data presented in Table 5.2, which gives:

$$w = 0.19 \cdot \exp(0.02 \cdot \theta_{amb}) \tag{5.11}$$

Therefore, a battery power correction law could be formulated as

$$|P_{batt}^{**}| = |P_{batt}^{*}| \cdot [1 - 0.19 \cdot \exp(0.02 \cdot \theta_{amb}) \cdot \ln \frac{\sigma^*}{\bar{\sigma}}] \tag{5.12}$$

The correction function is active only when $\sigma^* > \bar{\sigma}$, and $|P_{batt}^{**}|$ is bounded by 0 and $|P_{batt}^{*}|$. Ideally, the controller is expected to have a Pareto-like behavior by changing the value of $\bar{\sigma}$.

Table 5.2: w Value from Curve Fitting

θ_{amb}	15 °C	30 °C	45 °C
w	0.26	0.31	0.44

In this section, a battery power correction law (5.12) is developed based on the optimal battery aging behavior obtained from the DP solutions. The correction law has two parameters namely θ_{amb} and $\bar{\sigma}$. θ_{amb} is the ambient temperature, which is always known, while $\bar{\sigma}$ is a calibration parameter, which is dependent on the type of the battery, the powertrain architecture and the desired performance measure. The battery power correction is applied after the A-ECMS, leading to not only the correction on battery power but also the adjustment of the entire powertrain operating point, which is explained in the following section.

5.3 CVT ratio correction

When battery power output is corrected due to high-severity conditions, it is clear that $|P_{batt}^{**}| < |P_{batt}^{*}|$. As a result the corrected engine power output P_{ice}^{**} will be higher than the command generate by A-ECMS i.e. P_{ice}^{*}, so that the total power

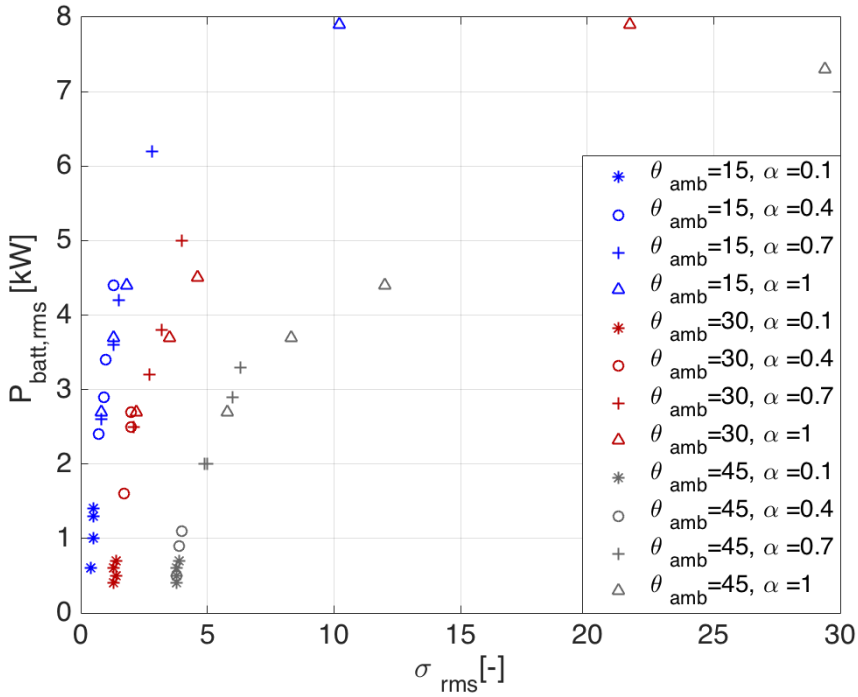

(a)

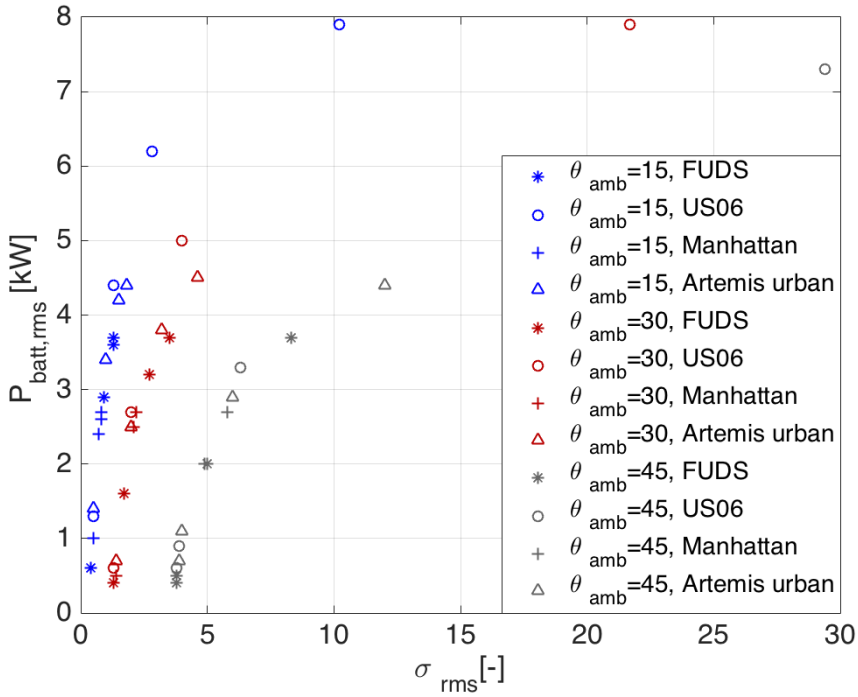

(b)

Figure 5.7: σ_{rms} and $P_{batt,rms}$ at different driving conditions obtained from Dynamic Programming

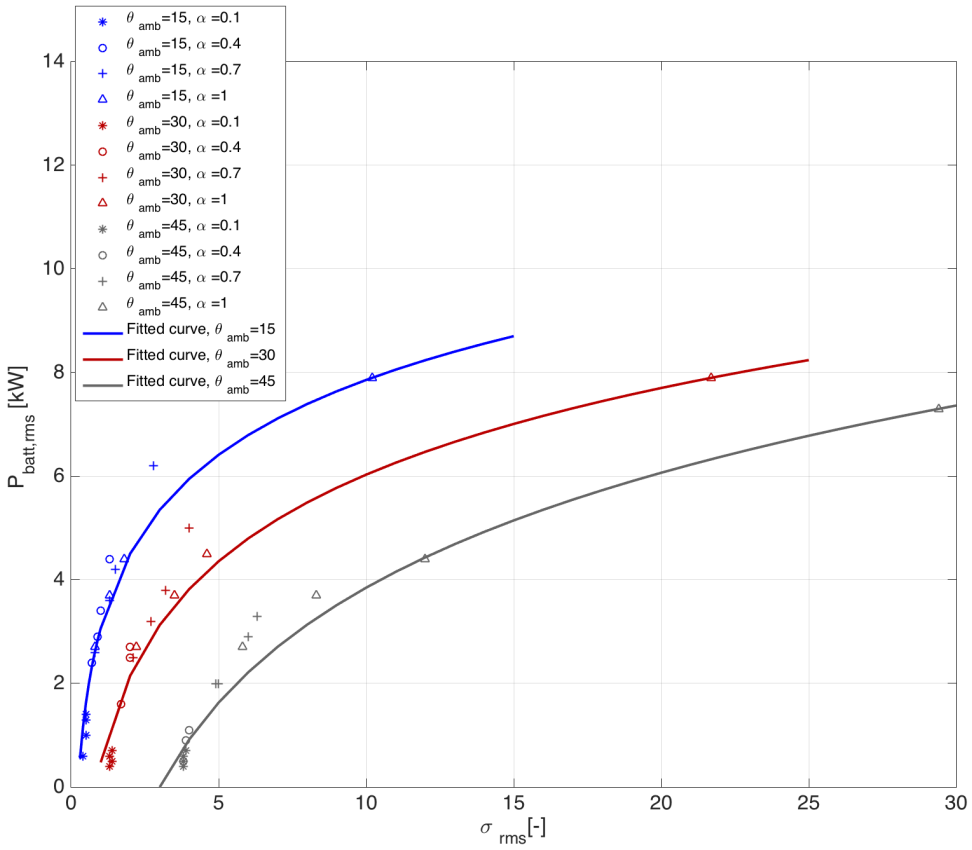

Figure 5.8: Curve fitting results for data obtained from Dynamic Programming

request is satisfied. With the new power split, the CVT ratio should be updated as well. Learning from the comparison between systematic optimization and sequential optimization, we know that transmission shifting with consideration of the total powertrain efficiency gives superior results. Therefore, an optimization problem is formulated and solved to search for the new optimal CVT ratio r_{cvt}^{**} for the corrected power split P_{batt}^{**} and P_{ice}^{**}.

Although the battery power output is fixed, the mechanical power output from the electric machine is dependent on the operating point of the machine on the efficiency map, which is determined by the CVT ratio, thus the engine operating point and fuel consumption are functions of CVT ratio. Figure 5.9 shows an example of engine fuel consumption as a function of CVT ratio with different batter power at a fixed road power request. Although the battery power is fixed, the mechanical power from the electric machine is not determined, which is dependent on the operating point of electric machine on the efficiency map, which is a function of transmission ratio. Since the sum of electric machine power and engine power should meet the wheel power request, engine power output as well as operating point are dependent on transmission ratio. Thus, with a given P_{batt}^{**}, the engine fuel consumption varies as CVT ratio r_{cvt} changes, and the r_{cvt} that yields the minimum fuel consumption should be selected as r_{cvt}^{**}.

An optimization problem is formulated and solved to determine r_{cvt}^{**}. To obtain an analytical expression of the engine fuel consumption and of the energy consumption of the electric machine, Willans line models for both the engine and electric machine

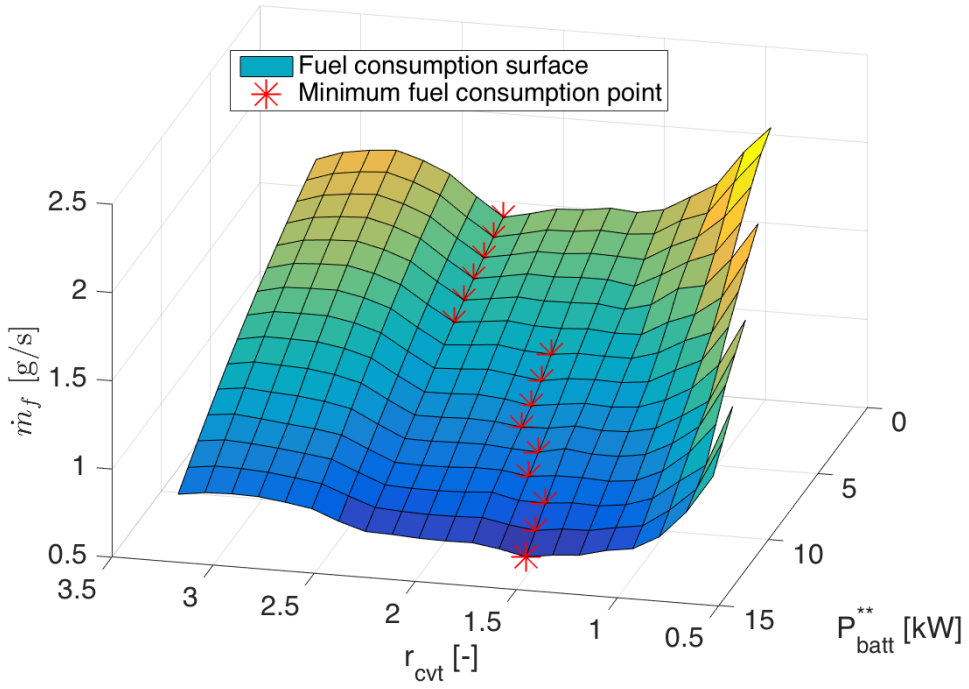

Figure 5.9: Possible engine fuel consumption at wheel power request of 21 kW

are developed [123]. The Willans line model was originally developed to represent the relationship between input and output power in an IC engine [106]. In this representation, the energy conversion efficiency is only dependent on the speed of the machine as described in (5.13). The Willans line model was later expanded to also represent the energy conversion efficiency of electric machines [123] (5.13).

$$\begin{aligned} P_{fuel} &= b_1(\omega_{ice}) \cdot P_{ice} + b_2(\omega_{ice}) \\ P_{ele} &= c_1(\omega_{em}) \cdot T_{em}^2 + c_2(\omega_{em}) \cdot T_{em} + c_3(\omega_{em}) \end{aligned} \tag{5.13}$$

The resulting model for both the engine and electric machine is visualized in Figure 5.10. To compute the new optimal CVT ratio, r_{cvt}^{**}, an optimization problem is formulated (5.14) and solved using the Matlab® build-in constrained function *fmincon*.

$$\min : P_{fuel}(t)$$

subject to

$$\begin{aligned} & T_{road}(t) = (T_{ice}(t) + T_{em}(t)) \cdot \eta_{cvt} \cdot r_{cvt}(t) \cdot r_{diff} \\ & \omega_{ice}(t) = \omega_{em}(t) = \omega_{wh}(t) \cdot r_{cvt}(t) \cdot r_{diff} \\ & \omega_{em}(t) \cdot T_{em}(t) \cdot c_1(\omega_{em}) + c_2(\omega_{em}) = P_{batt}^{**}(t) \\ & 0 \leqslant T_{ice}(t) \leqslant T_{ice_{max}}(\omega_{ice}(t)) \\ & T_{em_{min}}(\omega_{em}(t)) \leqslant T_{em}(t) \leqslant T_{em_{max}}(\omega_{em}(t)) \\ & \omega_{ice_{min}} \leqslant \omega_{ice}(t) \leqslant \omega_{ice_{max}} \\ & \omega_{em_{min}} \leqslant \omega_{em}(t) \leqslant \omega_{em_{max}} \\ & r_{cvt_{min}} \leqslant r_{cvt}(t) \leqslant r_{cvt_{max}} \end{aligned} \tag{5.14}$$

With P_{batt}^{**} and r_{cvt}^{**}, the corrected operating condition of the powertrain is determined for the given wheel power request. In general, if A-ECMS does not give

commands that accelerate battery aging ($\sigma^* \leqslant \bar{\sigma}$), the control outputs from A-ECMS (P^*_{batt} and r^*_{cvt}) are followed, otherwise the corrected battery power and corresponding CVT ratio (P^{**}_{batt} and r^{**}_{cvt}) are issued. The flow chart of the A-ECMS based energy management strategy with consideration of battery aging is shown in Figure 5.11.

5.4 Calibration and Simulation Results

In order to compare the performance of the aging-conscious A-ECMS with the optimal solution as well as to study the effects of the calibration parameter $\bar{\sigma}$ on the strategy, simulation results are compared and analyzed in this section. In the following simulation activities, the ambient temperature is 30 °C, and the parameters related to A-ECMS are: gain $k_p = 8$ and the adaptation interval $T = 60s$.

The performance of the aging-conscious A-ECMS strategy over US06 driving cycle is summarized in Table 5.3. When varying the value of $\bar{\sigma}$, a Pareto behavior of the controller can be observed, and the results of systematic optimization from DP with comparable performance measure are listed as well. It is clear that $\bar{\sigma}$ in the real-time controller plays the role of α in the optimal controller. As A-ECMS can not guarantee that the final battery SOC is exactly equal to its initial value, the final fuel consumption is corrected for charge sustenance. Although the fuel consumption from the real-time controller is a little bit higher, the general performance is quite close to the optimal controller. In the real world application, $\bar{\sigma}$ needs to be carefully selected based on the ambient conditions as well as the preference on the tradeoff.

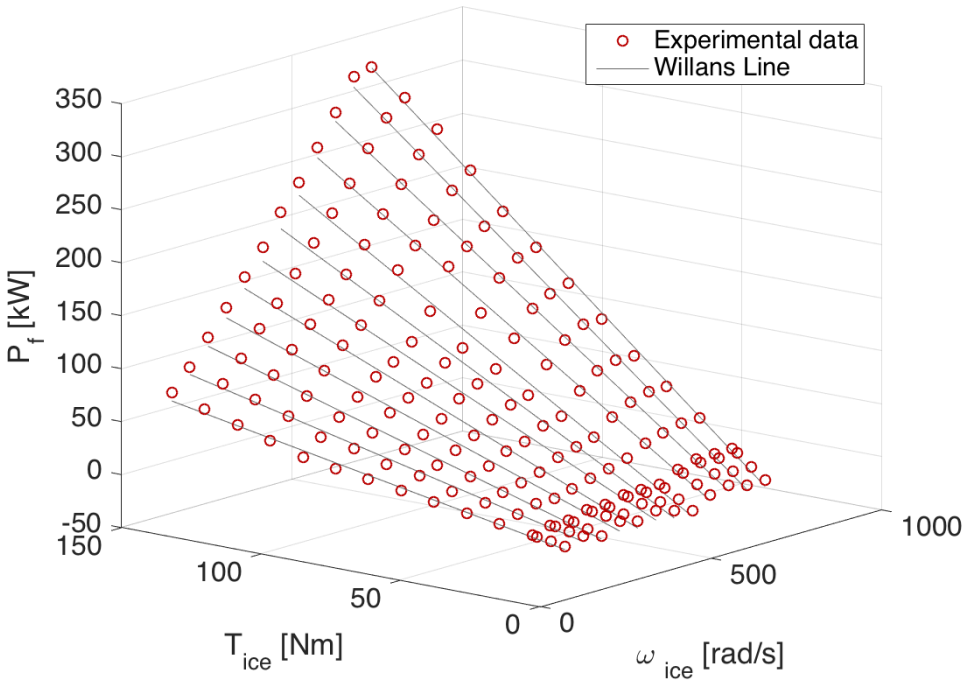

(a) Engine Willans Line Model

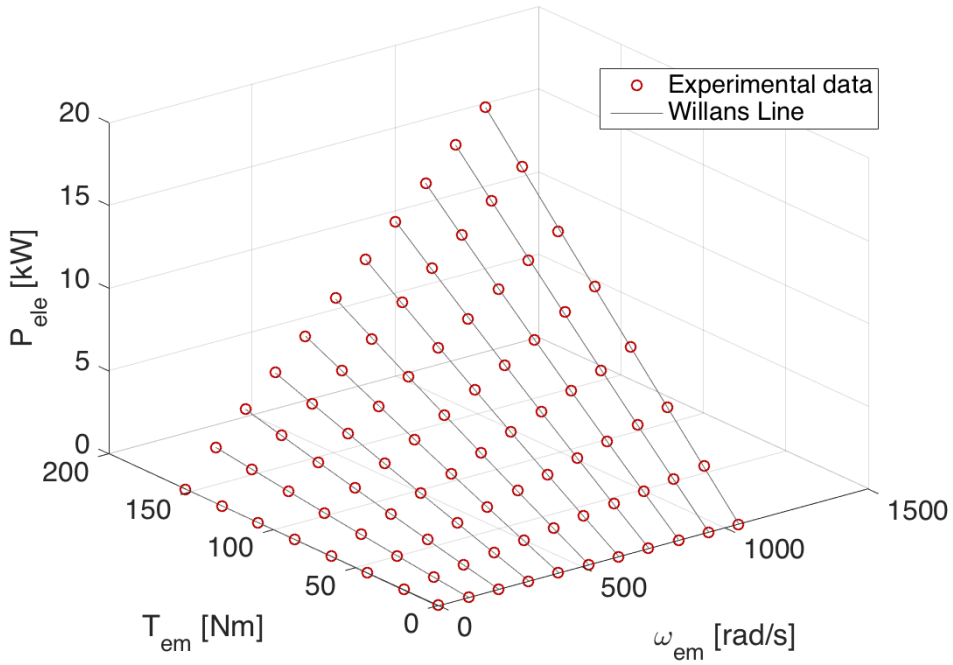

(b) Electric Machine Willans Line Model

Figure 5.10: Comparison between Willans line mode and experimental data

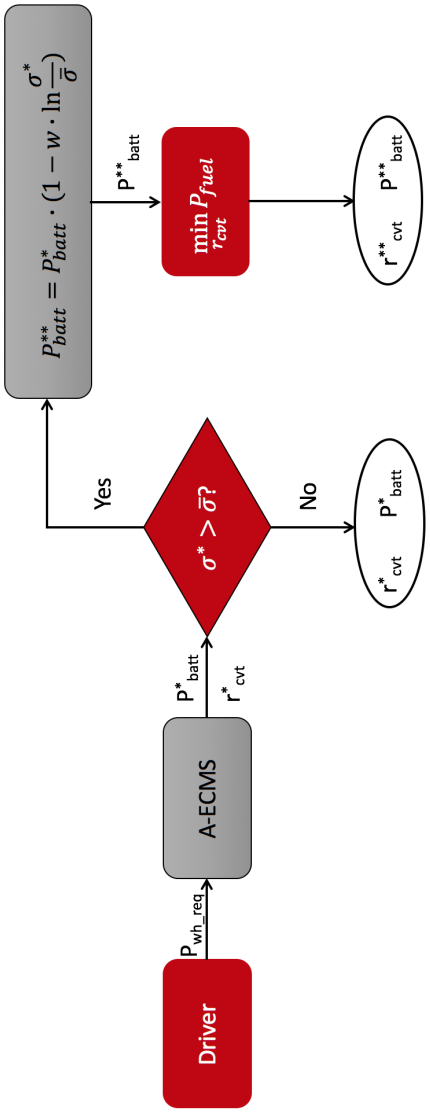

Figure 5.11: Control Flow Chart of A-ECMS Accounting for Battery Aging

Table 5.3: Performance of Aging-conscious A-ECMS over US06

Aging-conscious A-ECMS			DP		
$\bar{\sigma}$	Fuel [g]	Ah_{eff}	α	Fuel [g]	Ah_{eff}
20	559	24.6	0.9	546	24.5
10	568	14.6	0.8	556	14.4
5	578	7.7	0.7	568	8.3
2	594	3.0	0.5	586	3.4

Detailed simulation results for three different values of $\bar{\sigma}$ are studied to understand the control algorithm. In Figure 5.12, the SOC trajectories show that with lower severity factor threshold, battery energy is used in a less dynamical way, leading to lower battery temperature. The equivalence factor s^* is a result of the SOC profile. When SOC is much lower than the target value, which is 0.5 in this case, s^* increases to bring back battery energy. On the other hand, s^* decreases when SOC is higher than the target value. As the SOC trajectory with $\bar{\sigma} = 5$ has less fluctuation, the corresponding s^* is more stable than what from the other two cases.

In Figure 5.13, the battery power correction are shown for the three different severity factor threshold. When $\bar{\sigma}$ decreases, battery power output P^{**}_{batt} is further corrected compared with P^{*}_{batt}. In fact, P^{*}_{batt} from three cases is also different, because P^{**}_{batt} will influence SOC, which will have an impact on s^*, thus the commands from A-ECMS are different, which is P^{*}_{batt}.

The severity factor profiles in Figure 5.14 indicate that though battery power is corrected every time the severity factor reaches the threshold, a P^{**}_{batt} that yields a

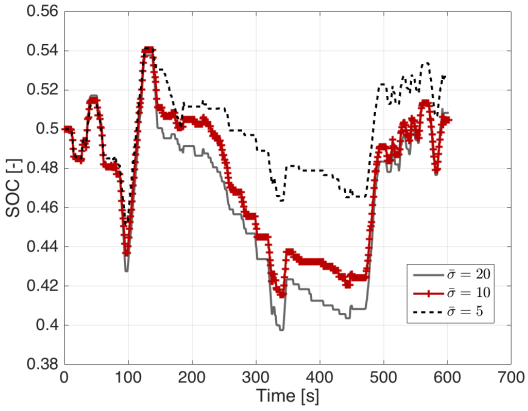

(a) SOC

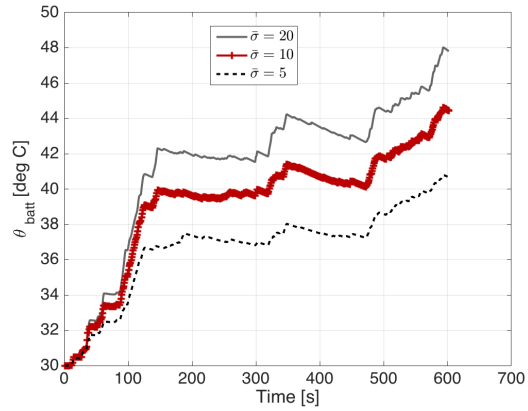

(b) θ_{batt}

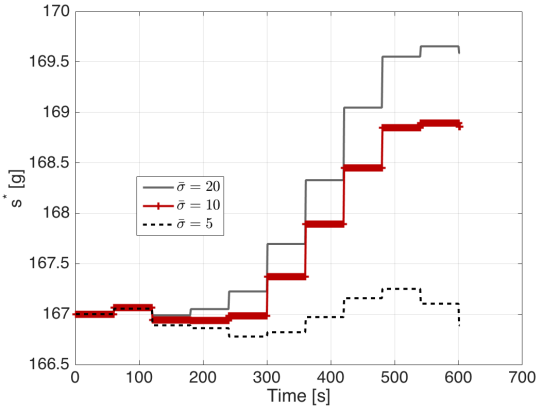

(c) s^*

Figure 5.12: Aging-conscious A-ECMS Controller Output over US06

severity factor bigger than the threshold ($\sigma^{**} > \bar{\sigma}$) is allowed when needed by the performance, and this is the intention for having the correction function in (5.12) instead of (5.8).

Similar observations can be made on the simulations results with FUDS, which are included in Appendix C.

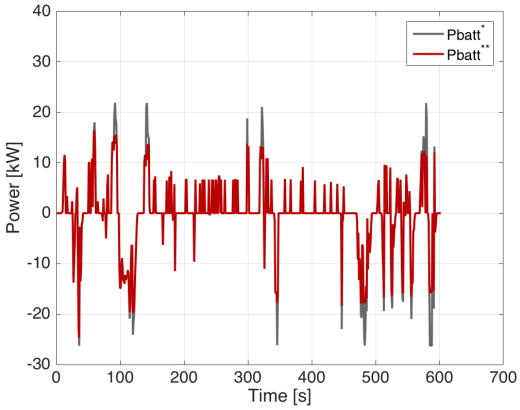

(a) $\bar{\sigma} = 20$

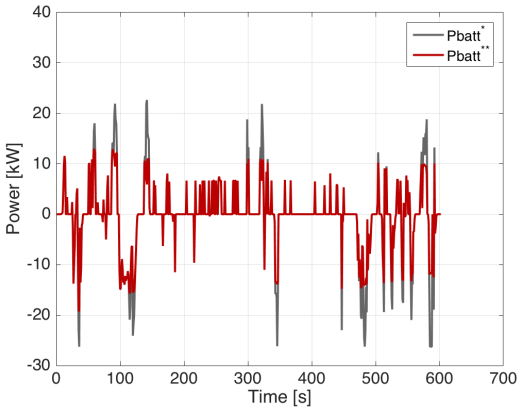

(b) $\bar{\sigma} = 10$

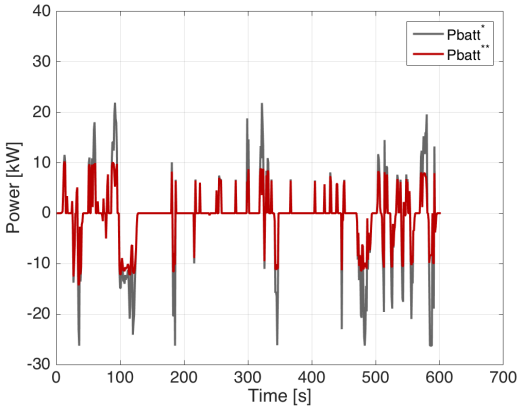

(c) $\bar{\sigma} = 5$

Figure 5.13: Battery Power Correction with Different $\bar{\sigma}$ over US06

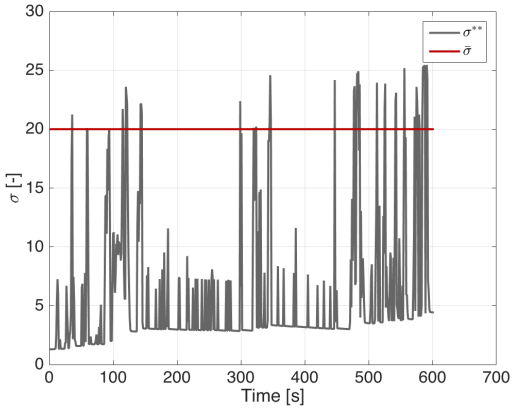

(a) $\bar{\sigma} = 20$

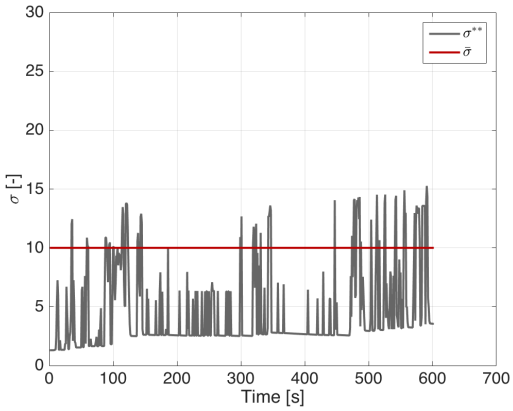

(b) $\bar{\sigma} = 10$

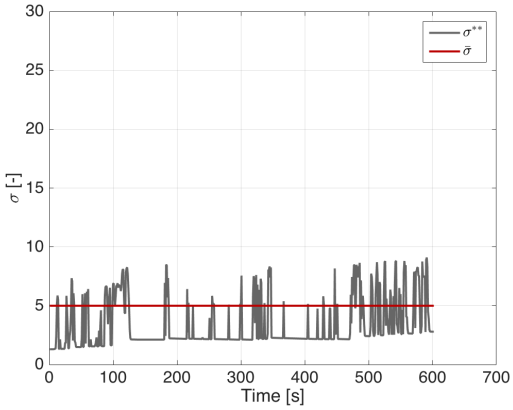

(c) $\bar{\sigma} = 5$

Figure 5.14: Battery Severity Factor with Different $\bar{\sigma}$ over US06

5.5 Validation

The last step in the process is to evaluate the performance of the controller under conditions that are substantially different from the driving cycles used in the development and analysis of the real-time control algorithm. The driving cycle used for the validation of the real-time controller is shown in Figure 5.15. The test cycle is a slight modification of a real-world test cycle used in the EcoCAR2 competition, with the addition of a low-speed urban driving section at the end.The test cycle covers various driving scenarios, ranging from highway driving at relatively high speed to stop-and-go urban driving to demonstrate the causality and effectiveness of the control algorithm. The simulation results shown in this section compare the real-time AA-ECMS algorithm to the DP solution obtained on the EcoCAR2 test cycle, the ambient temperature is 30 °C, and the same parameters related to A-ECMS are used as before: gain $k_p = 8$ and the adaptation interval $T = 60s$.

The simulation results for the test cycle are summarized in Table 5.4, in which the results of systematic optimization from DP are listed as benchmarks. As already explained, the choice of $\bar{\sigma}$ is arbitrary, and depends on the tradeoff one intends to achieve between fuel economy and battery aging. In general, the performance of the real-time controller is very close to the optimal solution. The detailed simulation results of the test cycle are shown in Figure 5.16, 5.17 and 5.18.

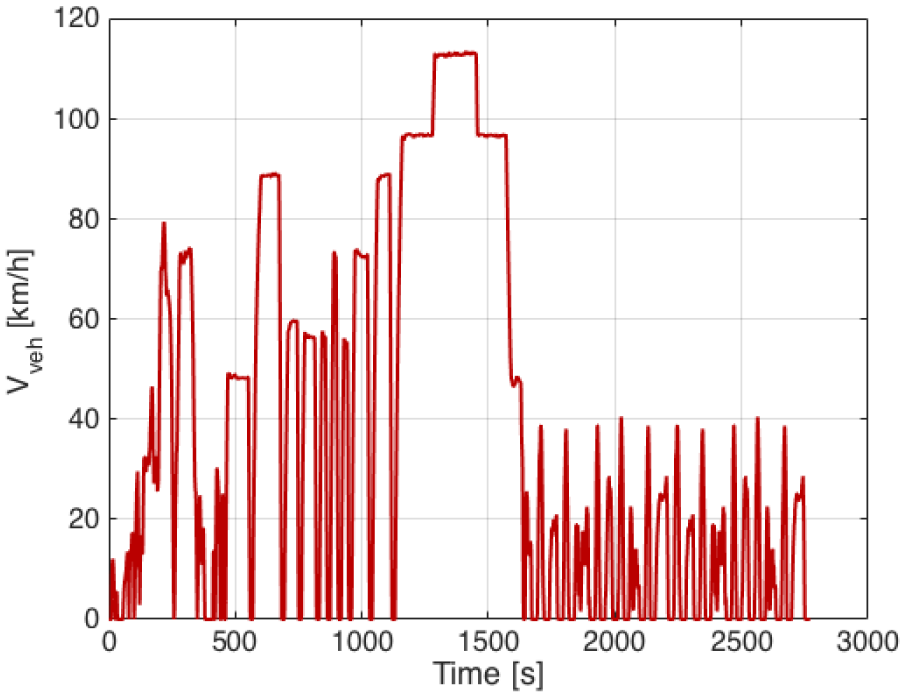

Figure 5.15: Speed Profile of Test Cycle

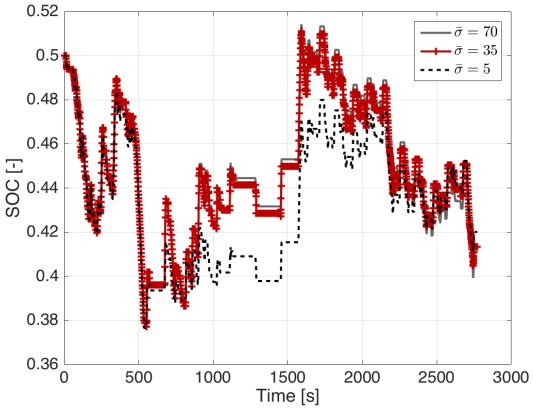

(a) SOC

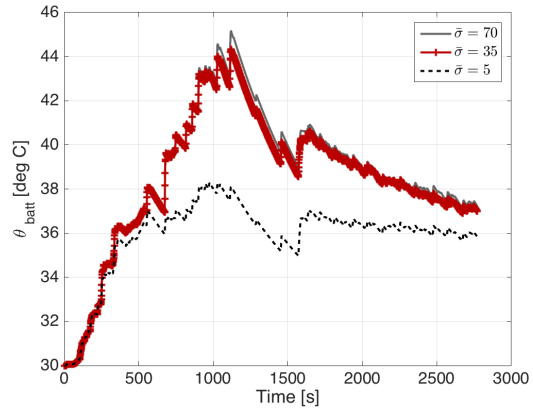

(b) θ_{batt}

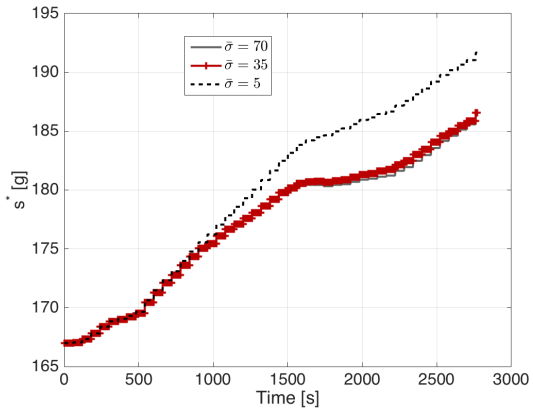

(c) s^*

Figure 5.16: Aging-conscious A-ECMS Controller Output over Test Cycle

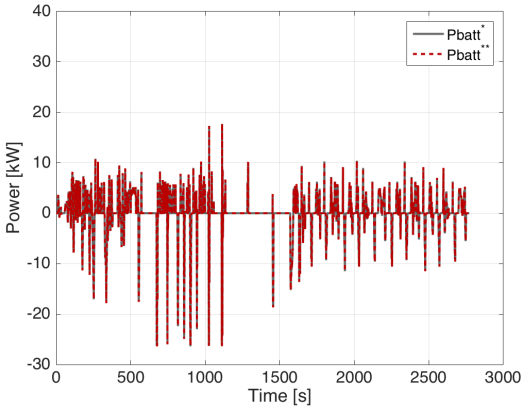

(a) $\bar{\sigma} = 70$

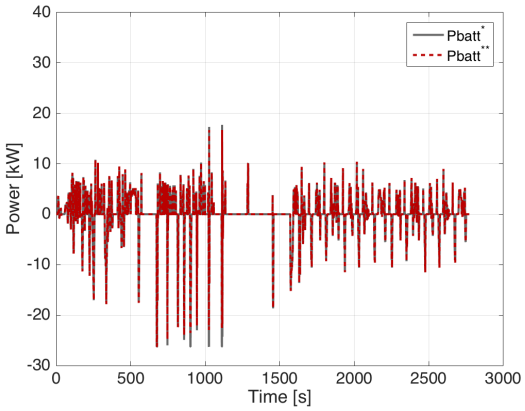

(b) $\bar{\sigma} = 35$

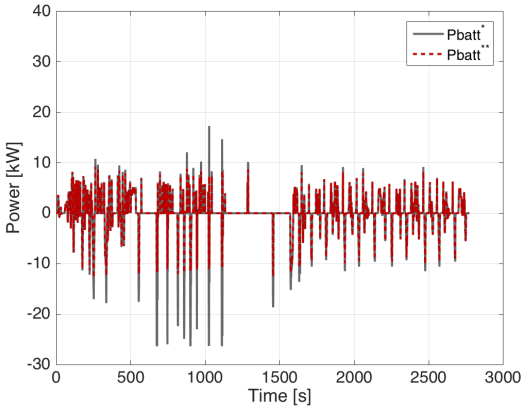

(c) $\bar{\sigma} = 5$

Figure 5.17: Battery Power Correction with Different $\bar{\sigma}$

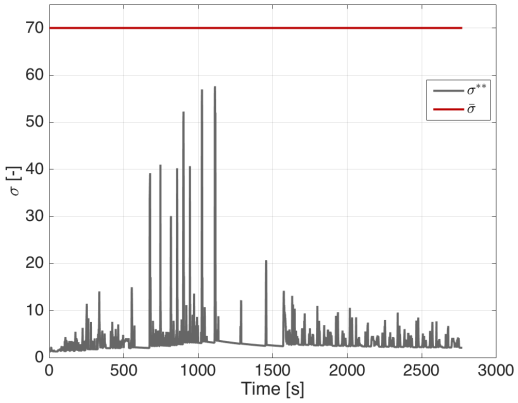

(a) $\bar{\sigma} = 70$

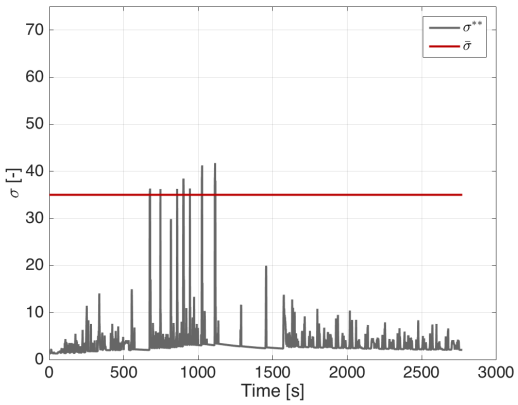

(b) $\bar{\sigma} = 35$

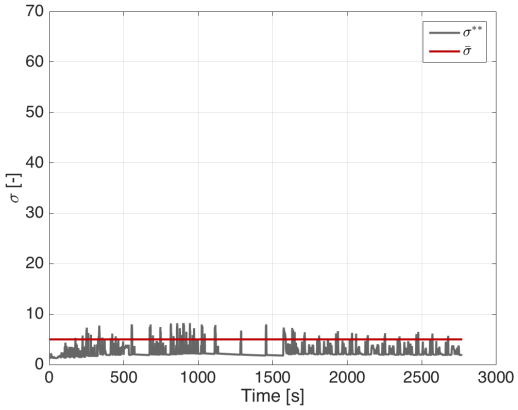

(c) $\bar{\sigma} = 5$

Figure 5.18: Battery Severity Factor with Different $\bar{\sigma}$

Table 5.4: Validation of Aging-conscious A-ECMS

Aging-conscious A-ECMS			DP		
$\bar{\sigma}$	Fuel [g]	Ah_{eff}	α	Fuel [g]	Ah_{eff}
70	1067	39.4	1	1088	39.7
35	1069	34.3	0.8	1104	34.2
5	1086	14.3	0.5	1141	15.2

5.6 Summary

In this chapter, a real-time implementable energy management strategy with consideration of battery aging is proposed, which is based on the Adaptive Equivalent Consumption Minimization Strategy. An aging severity based battery power correction function is developed based on the optimal performance from Dynamic Programming. In addition, a strategy for CVT ratio adjustment is proposed to account for additional fuel saving from optimal shifting. The simulation results show that the presented control algorithm can achieve performance comparable to optimal solutions.

The key elements for implementing the proposed strategy are an engine fuel consumption map, an electric machine efficiency map and a battery severity factor map, which is actually developed from the battery capacity degradation model. Those maps are available when the powertrain configuration is determined. In addition, there are three calibration parameters to be tuned for the desired performance, which are the adaptation gain k_p, the adaptation interval T, and severity factor threshold $\bar{\sigma}$. It has been shown that the overall performance of A-ECMS is robust with respected to k_p and T. The selection of $\bar{\sigma}$ is dependent on the location of the desired performance on the Pareto front.

Chapter 6: Conclusion

Electric and hybrid vehicles represent a steadily increasing segment of the automotive market due to many favorable features. The overall performance of xEVs, which includes drive quality, fuel economy and the total cost of ownership, is highly dependent on the design and control of the powertrain. This dissertation focuses on offering a systematic understanding of the relationship between fuel consumption and battery capacity degradation and developing energy management strategies that can optimally tradeoff between fuel consumption and capacity loss during the vehicle operation.

An appropriate model of the vehicle powertrain is necessary to study the performance and effect of the energy management strategy. A charge-sustaining parallel hybrid electric vehicle model is presented in Chapter 3 and is used to demonstrate the process of developing the control algorithm. Among all the modeling work, the most critical part is the control-oriented battery capacity degradation model. In this dissertation, a semi-empirical capacity degradation model that considers the battery Ah-throughput as a measure of battery life is adopted, and all the parameters are calibrated by the experimental data obtained from the HEV operating conditions. Therefore, the aging model is able to capture the aging behavior under the load cycle

of HEV operation, which directly influences the decision point of the controller.

In Chapter 4, the energy management problem in HEVs is formulated as an optimal control problem in which the control algorithm is required to tradeoff between two objectives: minimizing fuel consumption, and minimizing battery degradation. The battery capacity degradation model is directly linked to the optimal control problem through battery severity factor, which is a dimensionless variable that projects the long-term aging effect to the present and which allows the effective battery life depletion to be quantified. The optimal control problem is solved by both Dynamic Programming and the Pontryagin's Minimum Principle. Simulation-based results show that there is a fundamental tradeoff between fuel consumption and battery life, and it is possible to have a big saving on battery life with small sacrifice on fuel economy. In addition, transmission shifting strategy that considers the powertrain system efficiency can improve fuel economy significantly.

Given the fact that, charging is another battery aging source for plug-in hybrid electric vehicles, an optimal control based charging strategy is proposed, which aims to minimize battery capacity degradation incurred during charging by optimizing the charging current profile. A generic control-oriented vehicle cabin thermal model is developed to describe the battery surroundings taking into account solar radiation. Optimal solutions offered by Pontryagin's Minimum Principle show significant improvement on reducing aging effects, when compared with the results from the existing strategies. It is totally realizable to implement the optimal charging algorithm with the help of the vehicle cabin thermal model, the battery aging model and the

weather forecast.

Learning from the optimal solutions analyzed in Chapter 4, a real-time implementable battery aging-conscious energy management strategy is described in Chapter 5. The control algorithm is developed based on the frame work of Adaptive ECMS but with two additional features: aging-based battery power correction and CVT ratio correction. The essence is to correct or reduce the battery power whenever accelerated aging condition is recognized, and then the CVT ratio is corrected for the minimum fuel consumption given the corrected battery power. Simulation results show that the sub-optimal strategy can achieve performance comparable to optimal solutions with calibrations.

The effectiveness of the strategies proposed in this dissertation is demonstrated by a charge-sustaining parallel hybrid electric vehicle, however, the method can be applied equally well for hybrid electric vehicles with any powertrain configurations in charge-sustaining mode. The methodology proposed in this work can serve not only as a general way to design energy management strategies that incorporates battery aging, but also as a tool to assess the optimality of powertrain design in terms of the total cost of ownership.

Appendix A: The Comparison between Sequential Optimization and Systematic Optimization over FUDS

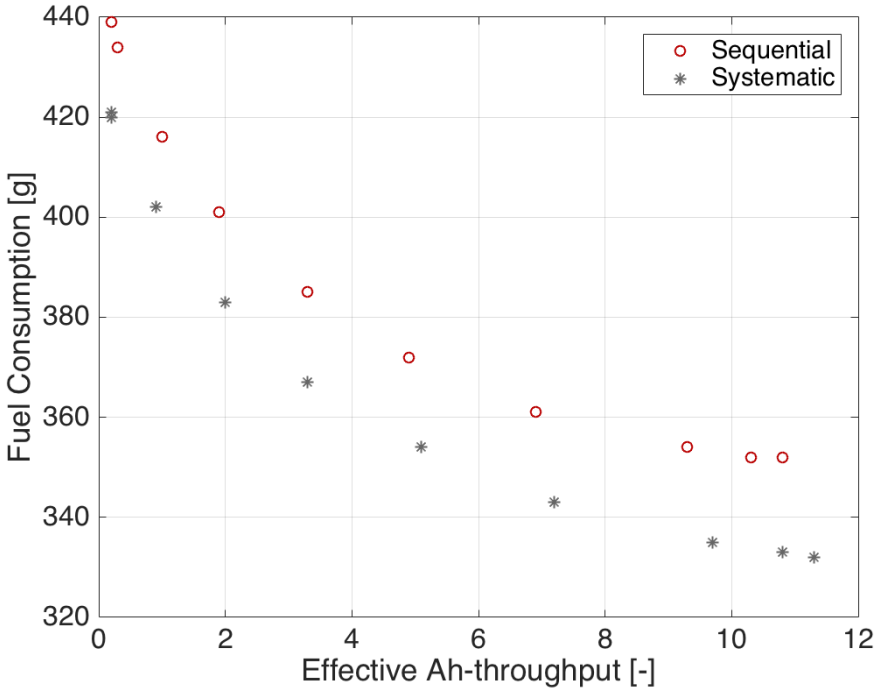

Figure A.1: Pareto Front of FUDS

Table A.1: Performance Measure of FUDS for Two Approaches

	Sequential		Systematic	
α	Fuel [g]	Ah_{eff}	Fuel [g]	Ah_{eff}
1	352	10.8	332	22.3
0.9	352	10.3	333	10.8
0.8	354	9.3	335	9.7
0.7	361	6.9	343	7.2
0.6	372	4.9	354	5.1
0.5	385	3.3	367	3.3
0.4	401	1.9	383	2.0
0.3	416	1.0	402	0.9
0.2	434	0.3	420	0.2
0.1	439	0.2	421	0.2

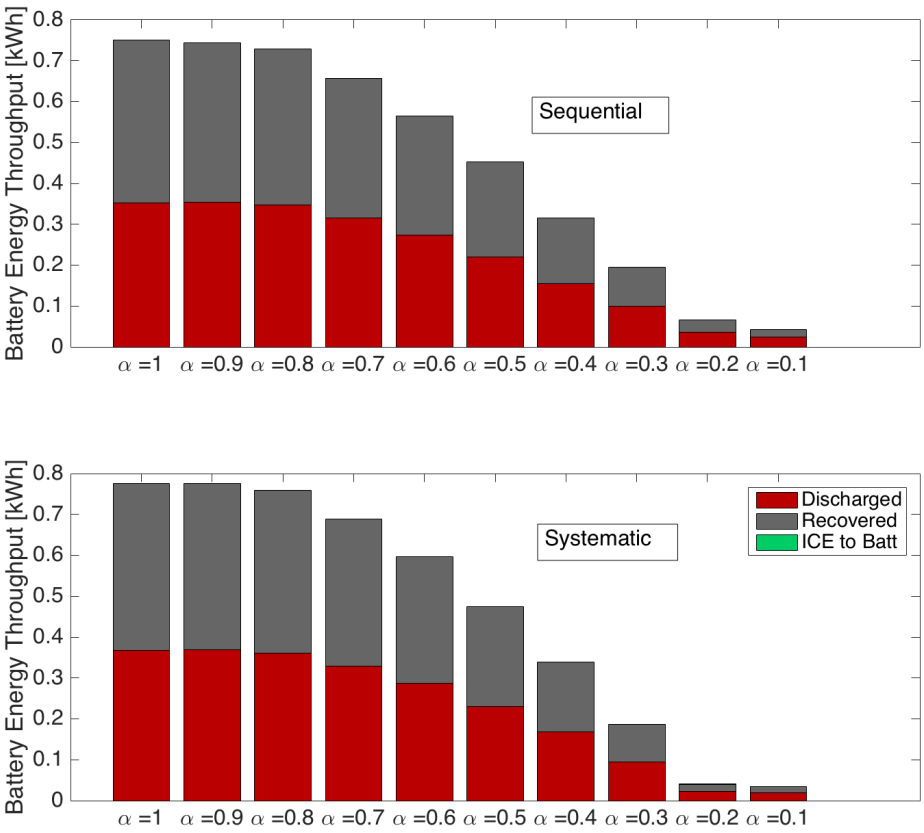

Figure A.2: Battery Energy Throughput of FUDS

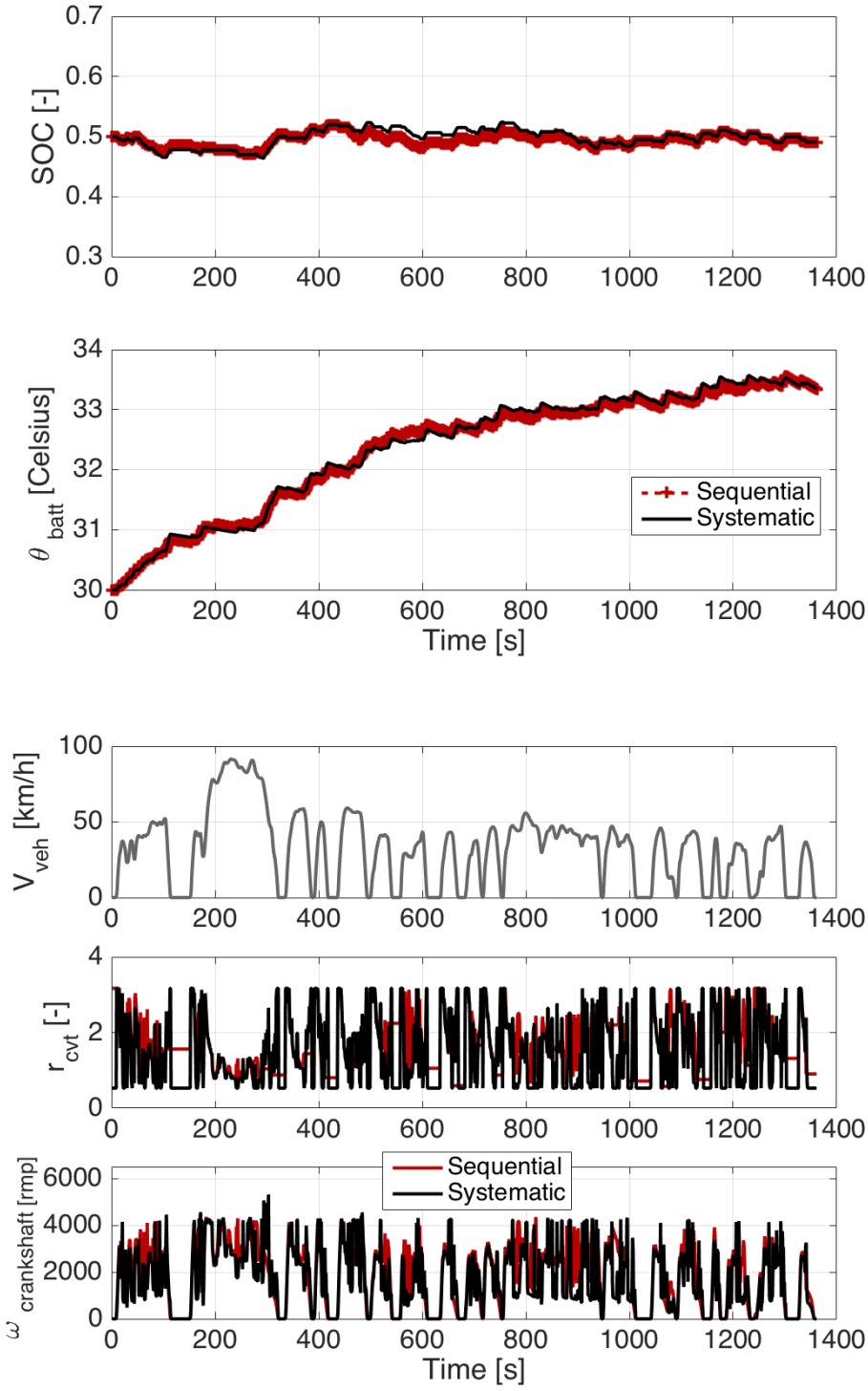

Figure A.3: State trajectories and CVT ratio for FUDS with $\alpha = 0.5$ at 30 °C

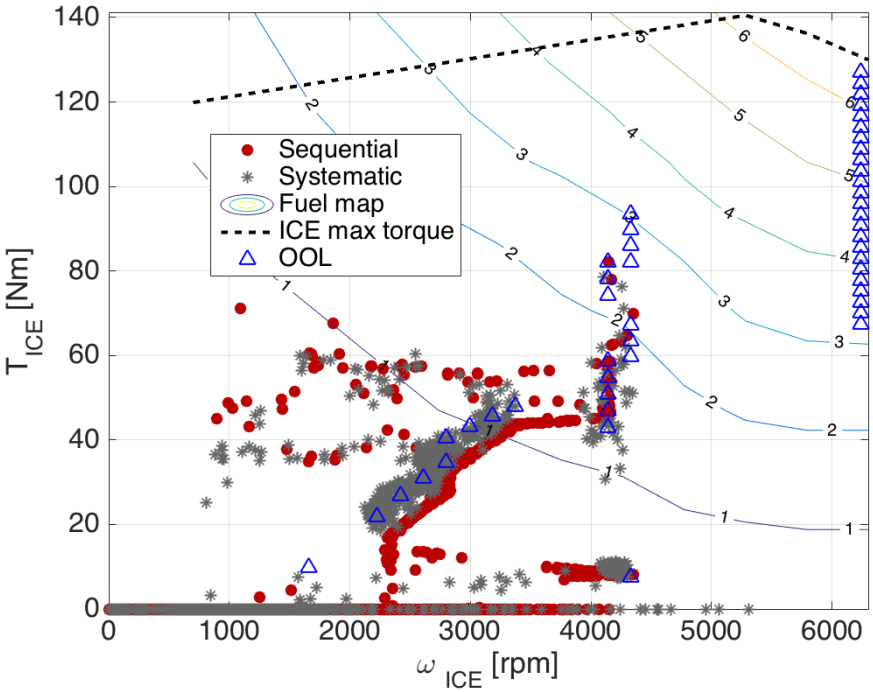

(a) Engine operating points

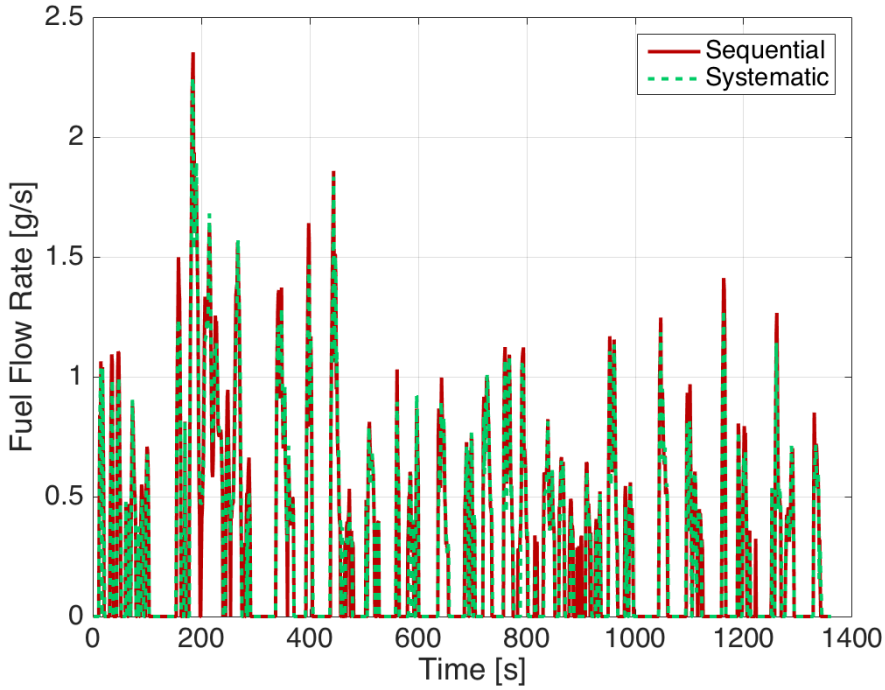

(b) Engine fuel flow rate

Figure A.4: Engine operating conditions for FUDS with $\alpha = 0.5$ at 30 °C

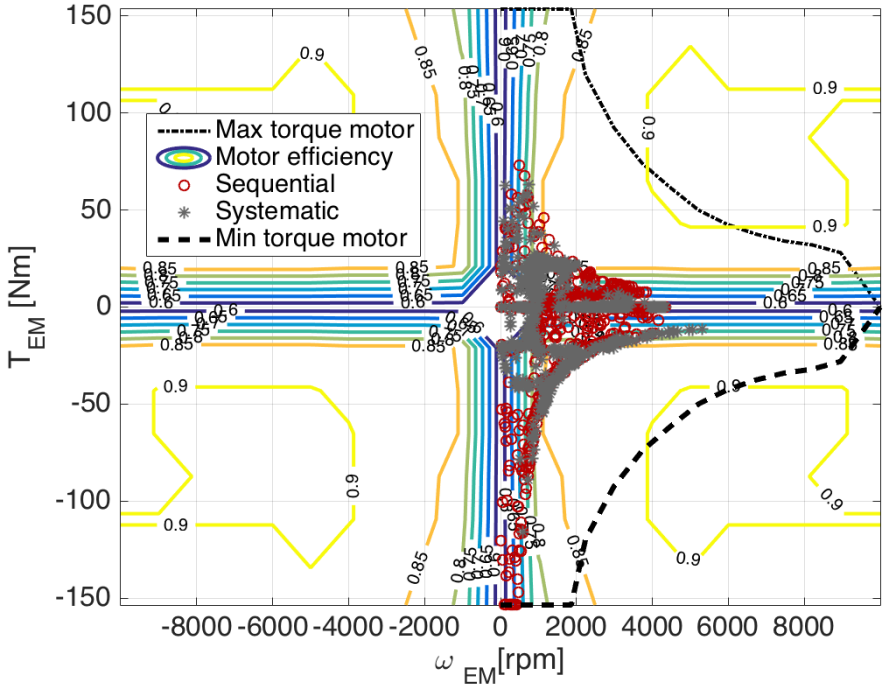

(a) Electric machine operating points

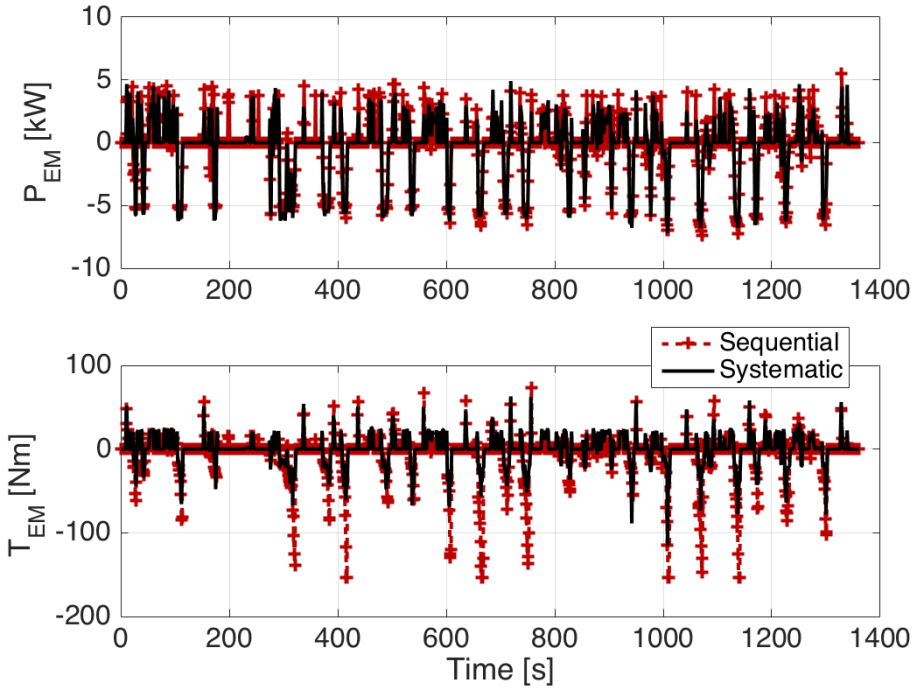

(b) Electric machine power and torque

Figure A.5: Electric machine operating conditions for FUDS with $\alpha = 0.5$ at 30 °C

Appendix B: Effects of Calibration Parameters on A-ECMS Performance over FUDS

Table B.1: Effect of Calibration Parameters

k_p	6	8	10
T [s]	$\frac{m_f}{m_f^*}$	$\frac{m_f}{m_f^*}$	$\frac{m_f}{m_f^*}$
30	1.023	1.015	1.016
60	1.016	1.016	1.021
120	1.022	1.019	1.017

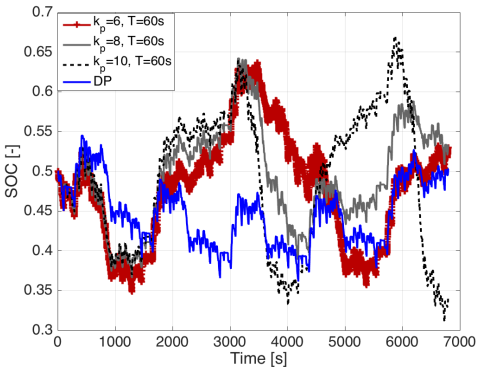

(a) SOC Trajectories

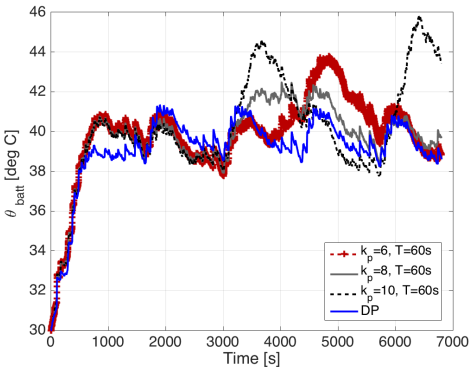

(b) Battery Temperature Trajectories

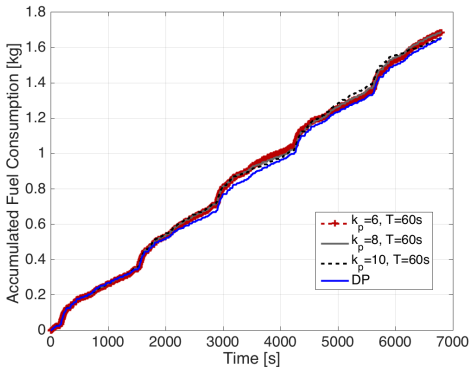

(c) Accumulated Fuel

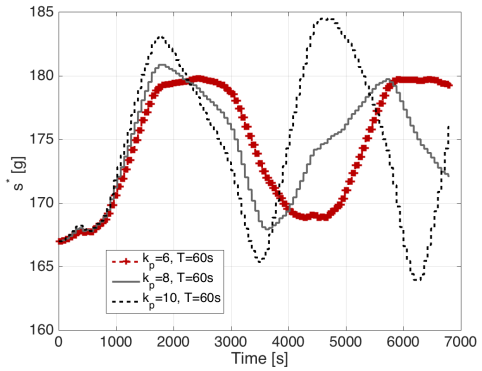

(d) s_{eqv} Trajectories

Figure B.1: Results obtained from five FUDS cycles with different k_p

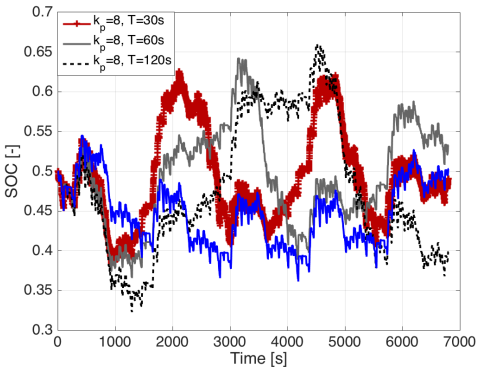

(a) SOC Trajectories

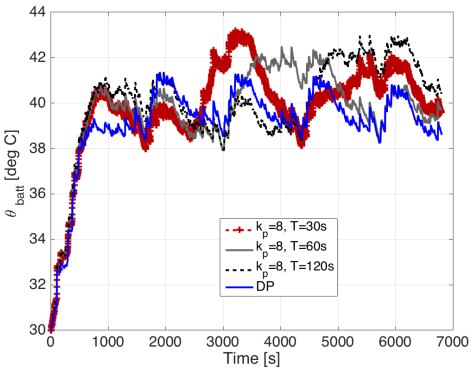

(b) Battery Temperature Trajectories

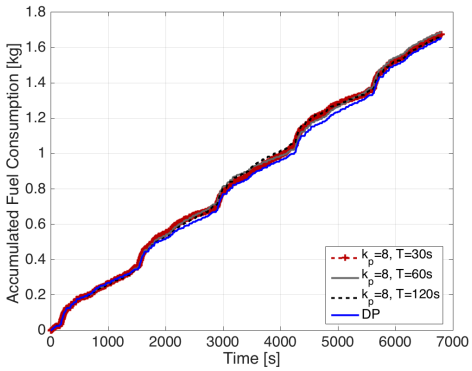

(c) Accumulated Fuel

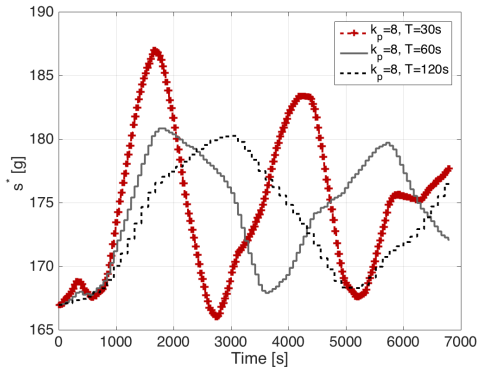

(d) s_{eqv} Trajectories

Figure B.2: Results obtained from five FUDS cycles with different T

Appendix C: Calibration and Simulation Results of Aging-concious A-ECMS over FUDS

Table C.1: Performance of Aging-concious A-ECMS over FUDS

Aging-concious A-ECMS			DP		
$\bar{\sigma}$	Fuel [g]	Ah_{eff}	α	Fuel [g]	Ah_{eff}
6	340	11.2	0.9	333	10.8
4	351	9.0	0.8	335	9.7
3	359	7.5	0.7	343	7.2
2	367	5.8	0.6	354	5.1

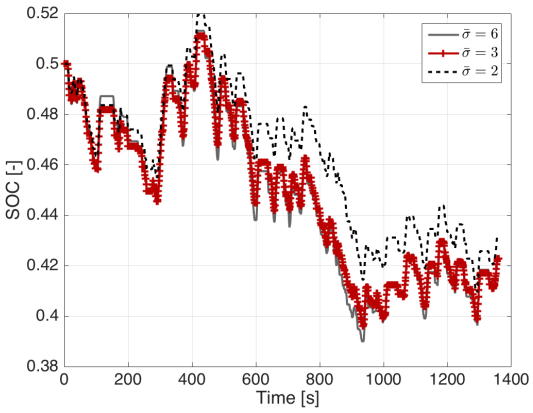

(a) SOC

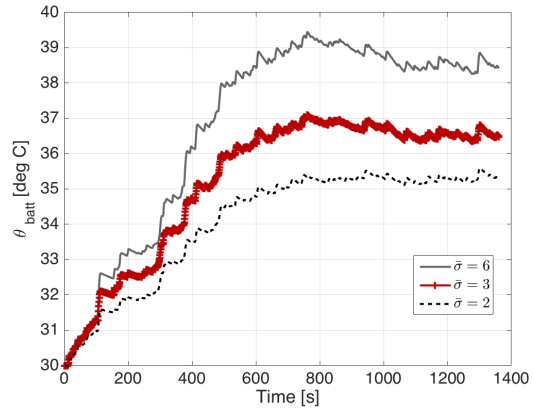

(b) θ_{batt}

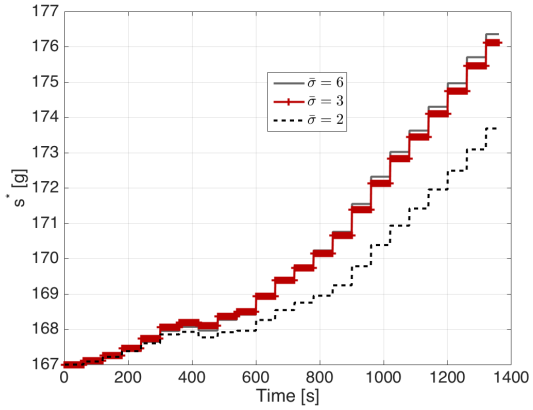

(c) s^*

Figure C.1: Aging-concious A-ECMS Controller Output over FUDS

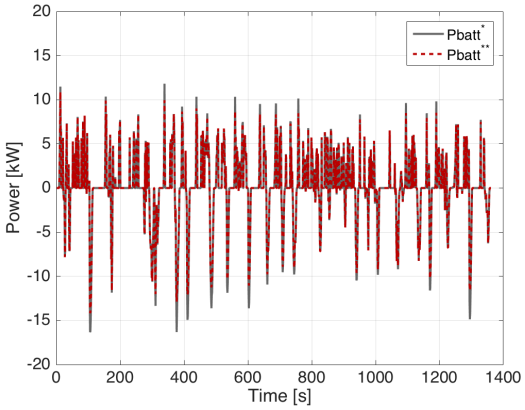

(a) $\bar{\sigma} = 6$

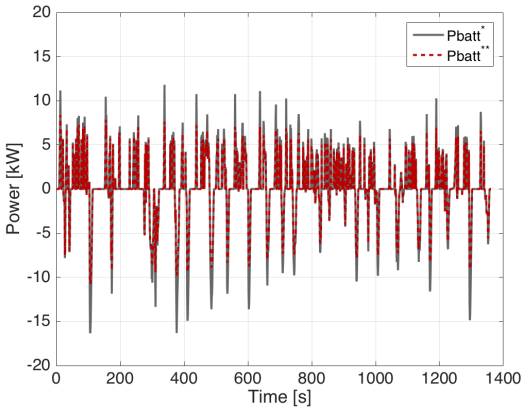

(b) $\bar{\sigma} = 3$

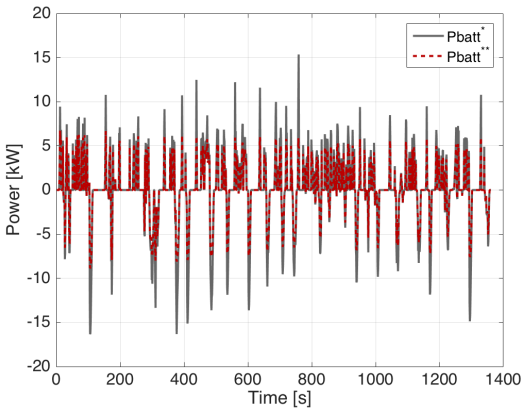

(c) $\bar{\sigma} = 2$

Figure C.2: Battery Power Correction with Different $\bar{\sigma}$ over FUDS

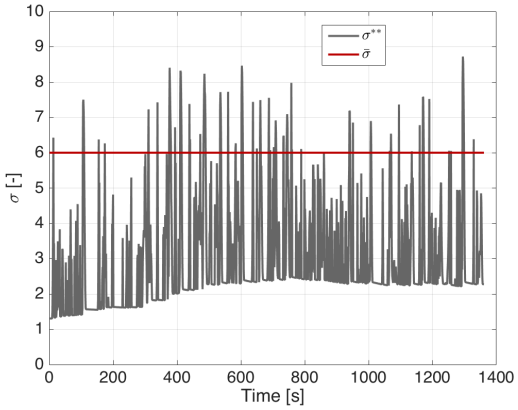

(a) $\bar{\sigma} = 6$

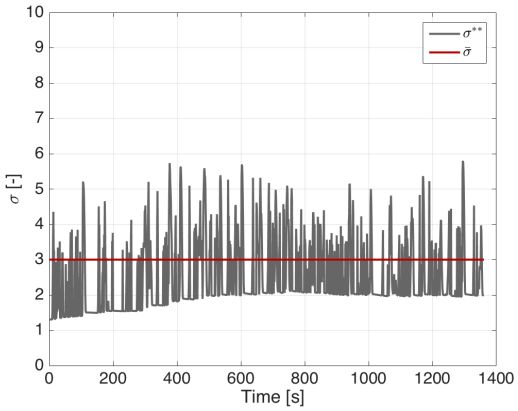

(b) $\bar{\sigma} = 3$

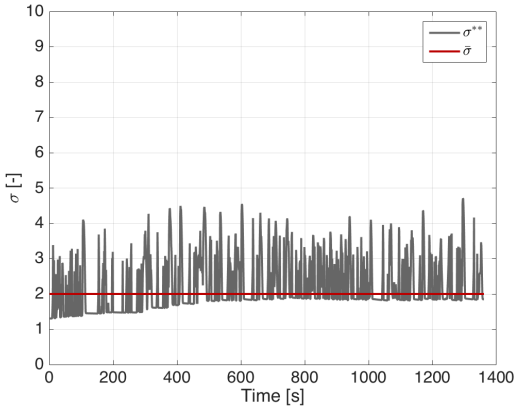

(c) $\bar{\sigma} = 2$

Figure C.3: Battery Severity Factor with Different $\bar{\sigma}$ over FUDS

Bibliography

[1] D Ambühl, A Sciarretta, C Onder, L Guzzella, S Sterzing, K Mann, D Kraft, and M Küsell. A causal operation strategy for hybrid electric vehicles based on optimal control theory. In *4th Symposium Hybrid Vehicles and Energy Management, Braunschweig*, 2007.

[2] Daniel Ambuhl and Lino Guzzella. Predictive reference signal generator for hybrid electric vehicles. *IEEE Transactions on Vehicular Technology*, 58(9):4730–4740, 2009.

[3] Pankaj Arora, Ralph E White, and Marc Doyle. Capacity fade mechanisms and side reactions in lithium-ion batteries. *Journal of the Electrochemical Society*, 145(10):3647–3667, 1998.

[4] HVAC APP SI HDBK ASHRAE. Hvac applications handbook. *IP Edition*, 2011.

[5] Dennis Assanis, G Delagrammatikas, R Fellini, Z Filipi, J Liedtke, N Michelena, P Papalambros, D Reyes, D Rosenbaum, A Sales, et al. Optimization approach to hybrid electric propulsion system design. *Journal of Structural Mechanics*, 27(4):393–421, 1999.

[6] D Aurbach. Electrode–solution interactions in Li-ion batteries a short summary and new insights. *Journal of power sources*, 119:497–503, 2003.

[7] Doron Aurbach. Review of selected electrode–solution interactions which determine the performance of Li and Li ion batteries. *Journal of Power Sources*, 89(2):206–218, 2000.

[8] Doron Aurbach, Boris Markovsky, Gregory Salitra, Elena Markevich, Yossi Talyossef, Maxim Koltypin, Linda Nazar, Brian Ellis, and Daniella Kovacheva. Review on electrode–electrolyte solution interactions related to cathode materials for Li-ion batteries. *Journal of Power Sources*, 165(2):491–499, 2007.

[9] Doron Aurbach, Yosef Talyosef, Boris Markovsky, Elena Markevich, Ella Zinigrad, Liraz Asraf, Joseph S Gnanaraj, and Hyeong-Jin Kim. Design of electrolyte solutions for Li and Li-ion batteries: a review. *Electrochimica Acta*, 50(2):247–254, 2004.

[10] Doron Aurbach, Ella Zinigrad, Yaron Cohen, and Hanan Teller. A short review of failure mechanisms of lithium metal and lithiated graphite anodes in liquid electrolyte solutions. *Solid state ionics*, 148(3):405–416, 2002.

[11] Michael Back, Matthias Simons, Frank Kirschaum, and Volker Krebs. Predictive control of drivetrains. In *Proc. in 2002 World Congress*, volume 15, pages 1506–1506, 2002.

[12] Harpreetsingh Banvait, Sohel Anwar, and Yaobin Chen. A rule-based energy management strategy for plug-in hybrid electric vehicle (PHEV). In *Proc. of 2009 American Control Conference*, pages 3938–3943. IEEE, 2009.

[13] Saeid Bashash, Scott J Moura, Joel C Forman, and Hosam K Fathy. Plug-in hybrid electric vehicle charge pattern optimization for energy cost and battery longevity. *Journal of power sources*, 196(1):541–549, 2011.

[14] Richard Bellman. Dynamic programming and lagrange multipliers. *Proceedings of the National Academy of Sciences*, 42(10):767–769, 1956.

[15] Richard Bellman and Robert E Kalaba. *Dynamic programming and modern control theory*, volume 81. Citeseer, 1965.

[16] Richard E Bellman and Stuart E Dreyfus. *Applied dynamic programming*. Princeton university press, 2015.

[17] Jeffrey R Belt, Chinh D Ho, Ted J Miller, M Ahsan Habib, and Tien Q Duong. The effect of temperature on capacity and power in cycled lithium ion batteries. *Journal of Power Sources*, 142(1):354–360, 2005.

[18] Rangeet Bhattacharyya, Baris Key, Hailong Chen, Adam S Best, Anthony F Hollenkamp, and Clare P Grey. In situ nmr observation of the formation of metallic lithium microstructures in lithium batteries. *Nature materials*, 9(6):504–510, 2010.

[19] Domenico Bianchi, Luciano Rolando, Lorenzo Serrao, Simona Onori, Giorgio Rizzoni, Nazar Al-Khayat, Tung-Ming Hsieh, and Pengju Kang. A rule-based strategy for a series/parallel hybrid electric vehicle: an approach based on dynamic programming. In *ASME 2010 Dynamic Systems and Control Conference*, pages 507–514. American Society of Mechanical Engineers, 2010.

[20] I Bloom, BW Cole, JJ Sohn, SA Jones, EG Polzin, VS Battaglia, GL Henriksen, C Motloch, R Richardson, T Unkelhaeuser, et al. An accelerated calendar and cycle life study of Li-ion cells. *Journal of Power Sources*, 101(2):238–247, 2001.

[21] Bram Bonsen, M Steinbuch, and PA Veenhuizen. CVT ratio control strategy optimization. In *Proc. 2005 IEEE Conf. Vehicle Power Propulsion*, volume 9, 2005.

[22] Hoseinali Borhan, Ardalan Vahidi, Anthony M Phillips, Ming L Kuang, Ilya V Kolmanovsky, and Stefano Di Cairano. Mpc-based energy management of a power-split hybrid electric vehicle. *IEEE Trans. Control Syst. Technol*, 20(3):593–603, 2012.

[23] Katherine Bovee. *Optimal control of electrified powertrains with the use of drive quality criteria*. PhD thesis, The Ohio State University, 2015.

[24] A Brahma, Y Guezennec, and G Rizzoni. Dynamic optimization of mechanical/electrical power flow in parallel hybrid electric vehicles. In *Proc. of 5th Intl Symposium on Advanced Vehicle Control, Ann Arbor, MI*, 2000.

[25] M Broussely, Ph Biensan, F Bonhomme, Ph Blanchard, S Herreyre, K Nechev, and RJ Staniewicz. Main aging mechanisms in Li-ion batteries. *Journal of Power Sources*, 146(1):90–96, 2005.

[26] Arthur E Bryson. Optimal control-1950 to 1985. *IEEE Control Systems*, 16(3):26–33, 1996.

[27] Alexandre Chasse, Antonio Sciarretta, and Jonathan Chauvin. Online optimal control of a parallel hybrid with costate adaptation rule. *IFAC Proceedings Volumes*, 43(7):99–104, 2010.

[28] Liang-Rui Chen. A design of an optimal battery pulse charge system by frequency-varied technique. *IEEE Transactions on Industrial Electronics*, 54(1):398–405, 2007.

[29] Liang-Rui Chen. Design of duty-varied voltage pulse charger for improving Li-ion battery-charging response. *IEEE Transactions on Industrial Electronics*, 56(2):480–487, 2009.

[30] Liang-Rui Chen, Jin-Jia Chen, Neng-Yi Chu, and Gia-Yo Han. Current-pumped battery charger. *IEEE Transactions on Industrial Electronics*, 55(6):2482–2488, 2008.

[31] Soo Seok Choi and Hong S Lim. Factors that affect cycle-life and possible degradation mechanisms of a Li-ion cell based on LiCoO2. *Journal of Power Sources*, 111(1):130–136, 2002.

[32] Jake Christensen. Modeling diffusion-induced stress in Li-ion cells with porous electrodes. *Journal of the Electrochemical Society*, 157(3):A366–A380, 2010.

[33] John Christensen and John Newman. Cyclable lithium and capacity loss in Li-ion cells. *Journal of the Electrochemical Society*, 152(4):A818–A829, 2005.

[34] Andrea Cordoba-Arenas, Simona Onori, Yann Guezennec, and Giorgio Rizzoni. Capacity and power fade cycle-life model for plug-in hybrid electric vehicle lithium-ion battery cells containing blended spinel and layered-oxide positive electrodes. *Journal of Power Sources*, 278:473–483, 2015.

[35] Andrea Cordoba-Arenas, Simona Onori, Giorgio Rizzoni, and Guodong Fan. Aging propagation in advanced battery systems: preliminary results. *IFAC Proceedings Volumes*, 46(21):313–318, 2013.

[36] Robert Darling and John Newman. Modeling side reactions in composite li y mn2 o 4 electrodes. *Journal of The Electrochemical Society*, 145(3):990–998, 1998.

[37] Daniele De Vito. Power flow management with predictive capabilities for a hybrid fuel cell vehicle. *IFAC Proceedings Volumes*, 40(10):9–16, 2007.

[38] Sebastien Delprat, Jimmy Lauber, Thierry-Marie Guerra, and Janette Rimaux. Control of a parallel hybrid powertrain: optimal control. *IEEE Transactions on Vehicular Technology*, 53(3):872–881, 2004.

[39] Stefano Di Cairano, Daniele Bernardini, Alberto Bemporad, and Ilya V Kolmanovsky. Stochastic MPC with learning for driver-predictive vehicle control and its application to HEV energy management. *IEEE Trans. Control Syst. Technol*, 22(3):1018–1031, 2014.

[40] Marc Doyle and John Newman. Analysis of capacity–rate data for lithium batteries using simplified models of the discharge process. *Journal of Applied Electrochemistry*, 27(7):846–856, 1997.

[41] Lan-Ron Dung and Jieh-Hwang Yen. Ilp-based algorithm for lithium-ion battery charging profile. In *2010 IEEE International Symposium on Industrial Electronics*, pages 2286–2291. IEEE, 2010.

[42] Soren Ebbesen, Christian Dönitz, and Lino Guzzella. Particle swarm optimisation for hybrid electric drive-train sizing. *International Journal of Vehicle Design*, 58(2-4):181–199, 2012.

[43] Soren Ebbesen, Philipp Elbert, and Lino Guzzella. Battery state-of-health perceptive energy management for hybrid electric vehicles. *IEEE Transaction on Vehicular Technology*, 61(7):2893–2900, 2012.

[44] Christian-Simon Ernst, André Hackbarth, Reinhard Madlener, Benedikt Lunz, Dirk Uwe Sauer, and Lutz Eckstein. Battery sizing for serial plug-in hybrid electric vehicles: A model-based economic analysis for germany. *Energy Policy*, 39(10):5871–5882, 2011.

[45] Rolf Findeisen, Lars Imsland, Frank Allgower, and Bjarne A Foss. State and output feedback nonlinear model predictive control: An overview. *European Journal of Control*, 9(2):190–206, 2003.

[46] Joel C Forman, Saeid Bashash, Jeffrey Stein, and Hosam Fathy. Reduction of an electrochemistry-based Li-ion battery health degradation model via constraint linearization and padé approximation. In *ASME 2010 Dynamic Systems and Control Conference*, pages 173–183. American Society of Mechanical Engineers, 2010.

[47] Lina Fu, Ö Ümit, Pinak Tulpule, and Vincenzo Marano. Real-time energy management and sensitivity study for hybrid electric vehicles. In *Proceedings of the 2011 American Control Conference*, pages 2113–2118. IEEE, 2011.

[48] Thomas F Fuller, Marc Doyle, and John Newman. Simulation and optimization of the dual lithium ion insertion cell. *Journal of the Electrochemical Society*, 141(1):1–10, 1994.

[49] Vincenzo Galdi, Lucio Ippolito, Antonio Piccolo, and Alfredo Vaccaro. A genetic-based methodology for hybrid electric vehicles sizing. *Soft Computing*, 5(6):451–457, 2001.

[50] Hans P Geering. *Optimal control with engineering applications*, volume 113. Springer, 2007.

[51] Kai Goebel, Bhaskar Saha, Abhinav Saxena, Jose R Celaya, and Jon P Christophersen. Prognostics in battery health management. *IEEE instrumentation & measurement magazine*, 11(4):33, 2008.

[52] Oleg Grodzevich and Oleksandr Romanko. Normalization and other topics in multi-objective optimization. In *The FieldsMITACS Industrial Problems Workshop*, 2006.

[53] Jens Groot. State-of-health estimation of Li-ion batteries: Cycle life test methods. Master's thesis, Chalmers University of Technology, Göteborg, 2012.

[54] Bo Gu. Supervisory control strategy development for a hybrid electric vehicle. Master's thesis, The Ohio State University, 2006.

[55] Bo Gu and Giorgio Rizzoni. An adaptive algorithm for hybrid electric vehicle energy management based on driving pattern recognition. In *ASME 2006 International Mechanical Engineering Congress and Exposition*, pages 249–258. American Society of Mechanical Engineers, 2006.

[56] WB Gu and CY Wang. Thermal-electrochemical modeling of battery systems. *Journal of The Electrochemical Society*, 147(8):2910–2922, 2000.

[57] Lino Guzzella and Antonio Sciarretta. *Vehicle propulsion systems*, volume 1. Springer, 2007.

[58] Kelsey B Hatzell, Aabhas Sharma, and Hosam K Fathy. A survey of long-term health modeling, estimation, and control of lithium-ion batteries: Challenges and opportunities. In *2012 American Control Conference (ACC)*, pages 584–591. IEEE, 2012.

[59] Theo Hofman, Maarten Steinbuch, Roell Van Druten, and Alex Serrarens. Rule-based energy management strategies for hybrid vehicles. *International Journal of Electric and Hybrid Vehicles*, 1(1):71–94, 2007.

[60] Anderson Hoke, Alexander Brissette, Dragan Maksimović, Damian Kelly, Annabelle Pratt, and David Boundy. Maximizing lithium ion vehicle battery life through optimized partial charging. In *Innovative Smart Grid Technologies (ISGT), 2013 IEEE PES*, pages 1–5. IEEE, 2013.

[61] Anderson Hoke, Alexander Brissette, Dragan Maksimović, Annabelle Pratt, and Kandler Smith. Electric vehicle charge optimization including effects of lithium-ion battery degradation. In *2011 IEEE Vehicle Power and Propulsion Conference*, pages 1–8. IEEE, 2011.

[62] Xiaosong Hu, Shengbo Li, Huei Peng, and Fengchun Sun. Charging time and loss optimization for Linmc and Lifepo 4 batteries based on equivalent circuit models. *Journal of Power Sources*, 239:449–457, 2013.

[63] Jia-Wei Huang, Yi-Hua Liu, Shun-Chung Wang, and Zong-Zhen Yang. Fuzzy-control-based five-step Li-ion battery charger. In *2009 International Conference on Power Electronics and Drive Systems (PEDS)*, pages 1547–1551. IEEE, 2009.

[64] Nashat Jalil, Naim A Kheir, and Mutasim Salman. A rule-based energy management strategy for a series hybrid vehicle. In *Proc. of 1997 American Control Conference*, volume 1, pages 689–693. IEEE, 1997.

[65] Soon-il Jeon, Sung-tae Jo, Yeong-il Park, and Jang-moo Lee. Multi-mode driving control of a parallel hybrid electric vehicle using driving pattern recognition. *Journal of dynamic systems, measurement, and control*, 124(1):141–149, 2002.

[66] Valerie H Johnson, Keith B Wipke, and David J Rausen. Hev control strategy for real-time optimization of fuel economy and emissions. *SAE Transactions*, 109(3):1677–1690, 2000.

[67] Eckhard Karden, Serve Ploumen, Birger Fricke, Ted Miller, and Kent Snyder. Energy storage devices for future hybrid electric vehicles. *Journal of Power Sources*, 168(1):2–11, 2007.

[68] Saida Kermani, Sebastien Delprat, Thierry-Marie Guerra, Rochdi Trigui, and Bruno Jeanneret. Predictive energy management for hybrid vehicle. *Control Engineering Practice*, 20(4):408–420, 2012.

[69] John TBA Kessels, Michiel WT Koot, Paul PJ Van Den Bosch, and Daniel B Kok. Online energy management for hybrid electric vehicles. *IEEE Transactions on vehicular technology*, 57(6):3428–3440, 2008.

[70] Hamid Khayyam, Abbas Z Kouzani, and Eric J Hu. Reducing energy consumption of vehicle air conditioning system by an energy management system. In *Intelligent Vehicles Symposium, 2009 IEEE*, pages 752–757. IEEE, 2009.

[71] Min-Joong Kim and Huei Peng. Power management and design optimization of fuel cell/battery hybrid vehicles. *Journal of power sources*, 165(2):819–832, 2007.

[72] Namwook Kim, Suk Won Cha, and Huei Peng. Optimal equivalent fuel consumption for hybrid electric vehicles. *IEEE Transactions on Control Systems Technology*, 20(3):817–825, 2012.

[73] Namwook Kim, Sukwon Cha, and Huei Peng. Optimal control of hybrid electric vehicles based on pontryagin's minimum principle. *IEEE Trans. Control Syst. Technol.*, 19(5):1279–1287, 2011.

[74] Donald E Kirk. *Optimal control theory: an introduction*. Courier Dover Publications, 2012.

[75] Reinhardt Klein, Nalin A Chaturvedi, Jake Christensen, Jasim Ahmed, Rolf Findeisen, and Aleksandar Kojic. Optimal charging strategies in lithium-ion battery. In *Proceedings of the 2011 American Control Conference*, pages 382–387. IEEE, 2011.

[76] Maxim Koltypin, Doron Aurbach, Linda Nazar, and Brian Ellis. On the stability of lifepo4 olivine cathodes under various conditions (electrolyte solutions, temperatures). *Electrochemical and Solid-State Letters*, 10(2):A40–A44, 2007.

[77] Kerem Koprubasi. *Modeling and control of a hybrid-electric vehicle for drivability and fuel economy improvements*. PhD thesis, The Ohio State University, 2008.

[78] Yong-Duk Lee and Sung-Yeul Park. Rapid charging strategy in the constant voltage mode for a high power Li-ion battery. In *2013 IEEE Energy Conversion Congress and Exposition*, pages 4725–4731. IEEE, 2013.

[79] Jun Li, Edward Murphy, Jack Winnick, and Paul A Kohl. The effects of pulse charging on cycling characteristics of commercial lithium-ion batteries. *Journal of Power Sources*, 102(1):302–309, 2001.

[80] Chan-Chiao Lin, Zoran Filipi, Yongsheng Wang, Loucas Louca, Huei Peng, Dennis N Assanis, and Jeffrey Stein. Integrated, feed-forward hybrid electric vehicle simulation in Simulink and its use for power management studies. Technical report, SAE Technical Paper, 2001.

[81] Chan-Chiao Lin, Jun-Mo Kang, JW Grizzle, and Huei Peng. Energy management strategy for a parallel hybrid electric truck. In *American Control Conference, 2001. Proceedings of the 2001*, volume 4, pages 2878–2883. IEEE, 2001.

[82] Chan-Chiao Lin, Huei Peng, Jessy W Grizzle, and Jun-Mo Kang. Power management strategy for a parallel hybrid electric truck. *IEEE Transactions on Control Systems Technology*, 11(6):839–849, 2003.

[83] Chia-Hsiang Lin, Chun-Yu Hsieh, and Ke-Horng Chen. A Li-ion battery charger with smooth control circuit and built-in resistance compensator for achieving stable and fast charging. *IEEE Transactions on Circuits and Systems I: Regular Papers*, 57(2):506–517, 2010.

[84] Ping Liu, John Wang, Jocelyn Hicks-Garner, Elena Sherman, Souren Soukiazian, Mark Verbrugge, Harshad Tataria, James Musser, and Peter Finamore. Aging mechanisms of LiFePO4 batteries deduced by electrochemical and structural analyses. *Journal of the Electrochemical Society*, 157(4):A499–A507, 2010.

[85] Wei Liu. *Introduction to hybrid vehicle system modeling and control*. John Wiley & Sons, 2013.

[86] Yi-Hwa Liu, Jen-Hao Teng, and Yu-Chung Lin. Search for an optimal rapid charging pattern for lithium-ion batteries using ant colony system algorithm. *IEEE Transactions on Industrial Electronics*, 52(5):1328–1336, 2005.

[87] Yi-Feng Luo, Yi-Hwa Liu, and Shun-Chung Wang. Search for an optimal multistage charging pattern for lithium-ion batteries using the taguchi approach. In *TENCON 2009-2009 IEEE Region 10 Conference*, pages 1–5. IEEE, 2009.

[88] Vincenzo Marano, Simona Onori, Yann Guezennec, Giorgio Rizzoni, and Nullo Madella. Lithium-ion batteries life estimation for plug-in hybrid electric vehicles. In *Proc. 2009 IEEE Conf. Vehicle Power and Propulsion Conference.*, pages 536–543. IEEE, 2009.

[89] James Marcicki, Alex Bartlett, Marcello Canova, A Terrence Conlisk, Giorgio Rizzoni, Yann Guezennec, Xiao Guang Yang, and Ted Miller. Characterization of cycle-life aging in automotive lithium-ion pouch cells. *ECS Transactions*, 50(26):235–247, 2013.

[90] James Marcicki, Giorgio Rizzoni, AT Conlisk, and Marcello Canova. A reduced-order electrochemical model of lithium-ion cells for system identification of battery aging. In *Proc. of 2011 ASME Dynamic Systems and Control Conference and Bath/ASME Symposium on Fluid Power and Motion Control*, pages 709–716. American Society of Mechanical Engineers, 2011.

[91] James Marcicki, Fabio Todeschini, Simona Onori, and Marcello Canova. Nonlinear parameter estimation for capacity fade in lithium-ion cells based on a reduced-order electrochemical model. In *Proc. of 2012 American Control Conference*, pages 572–577. IEEE, 2012.

[92] R Timothy Marler and Jasbir S Arora. Survey of multi-objective optimization methods for engineering. *Structural and multidisciplinary optimization*, 26(6):369–395, 2004.

[93] Scott J Moura, Jeffrey L Stein, and Hosam K Fathy. Battery-health conscious power management for plug-in hybrid electric vehicles via stochastic control. In *Proc. 2010 ASME Conf. Dynamic Systems and Control Conference*, pages 615–624. American Society of Mechanical Engineers, 2010.

[94] Nikolce Murgovski. *Optimal powertrain dimensioning and potential assessment of hybrid electric vehicles*. Chalmers University of Technology, 2012.

[95] Nikolce Murgovski, Lars Johannesson, Jonas Sjöberg, and Bo Egardt. Component sizing of a plug-in hybrid electric powertrain via convex optimization. *Mechatronics*, 22(1):106–120, 2012.

[96] Cristian Musardo, Giorgio Rizzoni, Yann Guezennec, and Benedetto Staccia. A-ECMS: An adaptive algorithm for hybrid electric vehicle energy management. *European Journal of Control*, 11(4):509–524, 2005.

[97] Cristian Musardo, Benedetto Staccia, Shawn Midlam-Mohler, Yann Guezennec, and Giorgio Rizzoni. Supervisory control for NOx reduction of an HEV with a mixed-mode HCCI/CIDI engine. In *Proc. 2005 American Control Conference*, pages 3877–3881. IEEE, 2005.

[98] Jeremy Neubauer and Eric Wood. Thru-life impacts of driver aggression, climate, cabin thermal management, and battery thermal management on battery electric vehicle utility. *Journal of Power Sources*, 259:262–275, 2014.

[99] Gang Ning and Branko N Popov. Cycle life modeling of lithium-ion batteries. *Journal of The Electrochemical Society*, 151(10):A1584–A1591, 2004.

[100] Gang Ning, Ralph E White, and Branko N Popov. A generalized cycle life model of rechargeable Li-ion batteries. *Electrochimica acta*, 51(10):2012–2022, 2006.

[101] EHJA Nuijten, M Koot, JTBA Kessels, B de Jager, M Heemels, W Hendrix, and P van den Bosch. Advanced energy management strategies for vehicle power nets. In *Proc. EAEC 9th Int. Congress: European Automotive Industry Driving Global Changes*, 2003.

[102] Simona Onori, Lorenzo Serrao, and Giorgio Rizzoni. Adaptive equivalent consumption minimization strategy for hybrid electric vehicles. In *ASME 2010 Dynamic Systems and Control Conference*, pages 499–505. American Society of Mechanical Engineers, 2010.

[103] Simona Onori, Lorenzo Serrao, and Giorgio Rizzoni. *Hybrid electric vehicles: energy management strategies*. Springer, 2016.

[104] Simona Onori, Pierfrancesco Spagnol, Vincenzo Marano, Yann Guezennec, and Giorgio Rizzoni. A new life estimation method for lithium–ion batteries in plug–in hybrid electric vehicles applications. *International Journal of Power Electronics*, 4(3):302–319, 2012.

[105] Daniel F Opila, Xiaoyong Wang, Ryan McGee, R Brent Gillespie, Jeffrey A Cook, and Jessy W Grizzle. An energy management controller to optimally trade off fuel economy and drivability for hybrid vehicles. *IEEE Transactions on Control Systems Technology*, 20(6):1490–1505, 2012.

[106] SJ Pachernegg. A closer look at the willans-line. Technical report, SAE Technical Paper, 1969.

[107] Thomas Miro Padovani, Maxime Debert, Guillaume Colin, Yann Chamaillard, et al. Optimal energy management strategy including battery health through thermal management for hybrid vehicles. *Advances in Automotive Control*, 7(1):384–389, 2013.

[108] Gino Paganelli. *Conception et commande d'une chaîne de traction pour véhicule hybride parallèle thermique et électrique*. PhD thesis, 1999.

[109] Gino Paganelli, Sebastien Delprat, Thierry-Marie Guerra, Janette Rimaux, and Jean-Jacques Santin. Equivalent consumption minimization strategy for parallel hybrid powertrains. In *Proc. IEEE 2002 Vehicle Technol. Conf.*, volume 4, pages 2076–2081. IEEE, 2002.

[110] Gino Paganelli, Gabriele Ercole, Avra Brahma, Yann Guezennec, and Giorgio Rizzoni. A general formulation for the instantaneous control of the power split in charge-sustaining hybrid electric vehicles. In *Proceedings of 5th Intl Symposium on Advanced Vehicle Control, Ann Arbor, MI*, 2000.

[111] Gino Paganelli, Gabriele Ercole, Avra Brahma, Yann Guezennec, and Giorgio Rizzoni. General supervisory control policy for the energy optimization of charge-sustaining hybrid electric vehicles. *JSAE review*, 22(4):511–518, 2001.

[112] Rakesh M Patil, Jarod C Kelly, Zoran Filipi, and Hosam K Fathy. A framework for the integrated optimization of charging and power management in plug-in hybrid electric vehicles. *IEEE Transactions on Vehicular Technology*, 62(6):2402–2412, 2013.

[113] Laura V Pérez, Guillermo R Bossio, Diego Moitre, and Guillermo O García. Optimization of power management in an hybrid electric vehicle using dynamic programming. *Mathematics and Computers in Simulation*, 73(1):244–254, 2006.

[114] Scott B Peterson, Jay Apt, and JF Whitacre. Lithium-ion battery cell degradation resulting from realistic vehicle and vehicle-to-grid utilization. *Journal of Power Sources*, 195(8):2385–2392, 2010.

[115] Pierluigi Pisu, Kerem Koprubasi, and Giorgio Rizzoni. Energy management and drivability control problems for hybrid electric vehicles. In *Proceedings of the 44th IEEE Conference on Decision and Control*, pages 1824–1830. IEEE, 2005.

[116] Pierluigi Pisu and Giorgio Rizzoni. A supervisory control strategy for series hybrid electric vehicles with two energy storage systems. In *Proc. 2005 IEEE Conf. Vehicle Power Propulsion*. IEEE, 2005.

[117] Pierluigi Pisu and Giorgio Rizzoni. A comparative study of supervisory control strategies for hybrid electric vehicles. *IEEE Trans. Control Syst. Technol.*, 15(3):506–518, 2007.

[118] Lev Semenovich Pontryagin. *Mathematical theory of optimal processes*. CRC Press, 1987.

[119] Mitra Pourabdollah, Nikolce Murgovski, Anders Grauers, and Bo Egardt. Optimal sizing of a parallel phev powertrain. *IEEE Transactions on Vehicular Technology*, 62(6):2469–2480, 2013.

[120] Christopher D Rahn and Chao-Yang Wang. *Battery systems engineering*. John Wiley & Sons, 2013.

[121] P Ramadass, Bala Haran, Parthasarathy M Gomadam, Ralph White, and Branko N Popov. Development of first principles capacity fade model for Li-ion cells. *Journal of the Electrochemical Society*, 151(2):A196–A203, 2004.

[122] P Ramadass, Bala Haran, Ralph White, and Branko N Popov. Mathematical modeling of the capacity fade of Li-ion cells. *Journal of Power Sources*, 123(2):230–240, 2003.

[123] Giorgio Rizzoni, Lino Guzzella, and Bernd M Baumann. Unified modeling of hybrid electric vehicle drivetrains. *IEEE/ASME Trans. Mechatronics*, 4(3):246–257, 1999.

[124] İsmail Levent Sarioglu, Olaf P Klein, Hendrik Schroder, and Ferit Kucukay. Energy management for fuel-cell hybrid vehicles based on specific fuel consumption due to load shifting. *IEEE Transactions on Intelligent Transportation Systems*, 13(4):1772–1781, 2012.

[125] Antonio Sciarretta, Michael Back, and Lino Guzzella. Optimal control of parallel hybrid electric vehicles. *IEEE Trans. Control Syst. Technol.*, 12(3):352–363, 2004.

[126] Antonio Sciarretta and Lino Guzzella. Control of hybrid electric vehicles. *IEEE Trans. Control Syst. Technol.*, 27(2):60–70, 2007.

[127] Antonio Sciarretta, Lino Guzzella, and Michael Back. A real-time optimal control strategy for parallel hybrid vehicles with on-board estimation of the control parameters. In *Proceedings of 2004 IFAC symposium on advances in automotive control*, pages 502–507, 2004.

[128] J Scordia, M Desbois-Renaudin, R Trigui, B Jeanneret, F Badin, and C Plasse. Global optimisation of energy management laws in hybrid vehicles using dynamic programming. *International Journal of Vehicle Design*, 39(4):349–367, 2005.

[129] Lorenzo Serrao. *A comparative analysis of energy management strategy for hybrid electric vehicles*. PhD thesis, The Ohio State University, 2009.

[130] Lorenzo Serrao, Simona Onori, and Giorgio Rizzoni. Ecms as a realization of Pontryagin's minimum principle for HEV control. In *Proc. of 2009 American Control Conference*, pages 3964–3969, 2009.

[131] Lorenzo Serrao, Simona Onori, and Giorgio Rizzoni. A comparative analysis of energy management strategies for hybrid electric vehicles. *Journal of Dynamic Systems, Measurement, and Control*, 133(3):031012, 2011.

[132] Lorenzo Serrao, Simona Onori, Giorgio Rizzoni, and Yann Guezennec. Model based strategy for estimation of the residual life of automotive batteries. In *Proc. of the Seventh IFAC Symposium on Fault Detection, Supervision and Safety of Technical Processes (SAFEPROCESS 09)*, pages 923–928, 2009.

[133] Lorenzo Serrao, Simona Onori, Antonio Sciarretta, Yann Guezennec, and Giorgio Rizzoni. Optimal energy management of hybrid electric vehicles including battery aging. In *Proc. American Control Conference (ACC)*, pages 2125–2130. IEEE, 2011.

[134] Lorenzo Serrao and Giorgio Rizzoni. Optimal control of power split for a hybrid electric refuse vehicle. In *Proc. of the 2008 American Control Conference*, pages 4498–4503, 2008.

[135] Weixiang Shen, Thanh Tu Vo, and Ajay Kapoor. Charging algorithms of lithium-ion batteries: an overview. In *Industrial Electronics and Applications (ICIEA), 2012 7th IEEE Conference on*, pages 1567–1572. IEEE, 2012.

[136] Godfrey Sikha, Branko N Popov, and Ralph E White. Effect of porosity on the capacity fade of a lithium-ion battery theory. *Journal of The Electrochemical Society*, 151(7):A1104–A1114, 2004.

[137] Pierfrancesco Spagnol, Simona Onori, Nullo Madella, Yann Guezennec, and John Neal. Aging and characterization of Li-ion batteries in a HEV application for lifetime estimation. In *Proc. of IFAC Symposium Advances in Automotive Control*, 2010.

[138] Stephanie Stockar, Vincenzo Marano, Marcello Canova, Giorgio Rizzoni, and Lino Guzzella. Energy-optimal control of plug-in hybrid electric vehicles for real-world driving cycles. *IEEE Trans. Vehi. Technol.*, 60(7):2949–2962, 2011.

[139] Kathryn Striebel, Joongpyo Shim, Azucena Sierra, Hui Yang, Xiangyun Song, Robert Kostecki, and Kathryn McCarthy. The development of low cost LiFePO 4-based high power lithium-ion batteries. *Journal of Power Sources*, 146(1):33–38, 2005.

[140] Olle Sundstrom and Lino Guzzella. A generic dynamic programming matlab function. In *2009 IEEE Control Applications,(CCA) & Intelligent Control,(ISIC)*, pages 1625–1630. IEEE, 2009.

[141] S Suri G., Onori. A control-oriented Li-ion battery aging model for hybrid electric vehicle optimization. *Energy*, 96:644–653, 2015.

[142] L Tang, G Rizzoni, and A Cordoba-Arenas. Battery life extending charging strategy for plug-in hybrid electric vehicles and battery electric vehicles. *IFAC-PapersOnLine*, 49(11):70–76, 2016.

[143] Li Tang and Giorgio Rizzoni. Energy management strategy including battery life optimization for a hev with a cvt. In *Transportation Electrification Asia-Pacific (ITEC Asia-Pacific), 2016 IEEE Conference and Expo*, pages 549–554. IEEE, 2016.

[144] Li Tang, Giorgio Rizzoni, and Simona Onori. Energy management strategy for hevs including battery life optimization. *Transportation Electrification, IEEE Transactions on*, 1(3):211–222, 2015.

[145] J Vetter, P Novak, MR Wagner, C Veit, K-C Möller, JO Besenhard, M Winter, M Wohlfahrt-Mehrens, C Vogler, and A Hammouche. Ageing mechanisms in lithium-ion batteries. *Journal of Power Sources*, 147(1):269–281, 2005.

[146] Emmanuel Vinot and Rochdi Trigui. Optimal energy management of hevs with hybrid storage system. *Energy Conversion and Management*, 76:437–452, 2013.

[147] John Wang, Ping Liu, Jocelyn Hicks-Garner, Elena Sherman, Souren Soukiazian, Mark Verbrugge, Harshad Tataria, James Musser, and Peter Finamore. Cycle-life model for graphite-LiFePO4 cells. *Journal of Power Sources*, 196(8):3942–3948, 2011.

[148] M Stanley Whittingham. History, evolution, and future status of energy storage. *Proceedings of the IEEE*, 100(Special Centennial Issue):1518–1534, 2012.

[149] Lianghong Wu, Yaonan Wang, Xiaofang Yuan, and Zhenlong Chen. Multiobjective optimization of hev fuel economy and emissions using the self-adaptive differential evolution algorithm. *IEEE Transactions on vehicular technology*, 60(6):2458–2470, 2011.

[150] Toshihiro Yoshida, Michio Takahashi, Satoshi Morikawa, Chikashi Ihara, Hiroyuki Katsukawa, Tomoyuki Shiratsuchi, and Jun-ichi Yamaki. Degradation mechanism and life prediction of lithium-ion batteries. *Journal of The Electrochemical Society*, 153(3):A576–A582, 2006.

[151] Zou Yuan, Liu Teng, Sun Fengchun, and Huei Peng. Comparative study of dynamic programming and pontryagins minimum principle on energy management for a parallel hybrid electric vehicle. *Energies*, 6(4):2305–2318, 2013.

[152] Xi Zhang and Chris Mi. *Vehicle power management: modeling, control and optimization*. Springer Science & Business Media, 2011.